DEVELOPMENT OF A NEW INFRARED SPECTROSCOPIC METHOD BASED ON MULTIVARIATE CALIBRATION FOR THE DETERMINATION OF ALUMINUM AND MAGNESIUM OXIDE THICKNESS ON ALUMINUM FOIL AND SHEETS SURFACES

A Thesis Submitted to
the Graduate School of Engineering and Sciences of
İzmir Institute of Technology
in Partial Fulfillment of the Requirements for the Degree of

MASTER OF SCIENCE

in Chemistry

by
Ayten Ekin MEŞE

July 2016
İZMİR

We approve the thesis of **Ayten Ekin MEŞE**

Examining Committee Members:

Prof. Dr. Durmuş ÖZDEMİR
Department of Chemistry, İzmir Institute of Technology

Doç. Dr. Hasan ERTAŞ
Department of Chemistry, Ege University

Prof. Dr. Figen TOKATLI
Department of Food Engineering, İzmir Institute of Technology

28 July 2016

Prof. Dr. Durmuş ÖZDEMİR
Supervisor, Department of Chemistry,
İzmir Institute of Technology

Prof. Dr. Ahmet Emin EROĞLU
Head of the Department of Chemistry

Prof. Dr. Bilge KARAÇALI
Dean of the Graduate School of
Engineering and Sciences

ACKNOWLEDGEMENTS

There are a number of people without whom it would not have been possible to complete this master thesis and to whom I am grateful.

To my supervisor, Prof. Dr. Durmuş ÖZDEMİR, for his full support, expert guidance, understanding and encouragement over the last year and a half. His in-depth knowledge and patience made it possible to complete this thesis and I cannot image this study could not be finished without his endless help. I am extremely grateful being part of a work team of his research group.

Besides my advisor, I would like to thank to rest of my thesis committee: Prof. Dr. Figen TOKATLI and Assoc. Prof. Dr. Hasan ERTAŞ

To members of Chemometrics Research Group, Başak BAŞAR and Gün Deniz AKKOÇ, for their help, great patience and motivation at all times. They are always with me when I feel desperate and they are always there for me when I need them.

To ASSAN Aluminum, for their technical support and providing Grazing Angle ATR for this research. Also, to ASSAN Aluminum Research and Development Laboratory Unit Manager Özlem İNANÇ UÇAR and ASSAN Aluminum Technology Director Dr. Murat DÜNDAR for performing annealing processes of the aluminum samples, their kindness and helps at any subject of interest.

To Prof. Dr. Şefik SÜZER and his research group for providing XPS reference measurements which are the vital part of this study.

Finally, my sincere thanks to my parents, Dilek and Metin MEŞE, my brother, Mehmet Batuhan MEŞE and my friends Ece Aybala DEMİR and İpek HARMANLI for supporting me spiritually throughout my entire study and encouraged my activities.

ABSTRACT

DEVELOPMENT OF A NEW INFRARED SPECTROSCOPIC METHOD BASED ON MULTIVARIATE CALIBRATION FOR THE DETERMINATION OF ALUMINUM AND MAGNESIUM OXIDE THICKNESS ON ALUMINUM FOIL AND SHEETS SURFACES

Surface oxidation is a general problem for certain industrial applications such as coating and painting of the finished rolled products. A detailed understanding for the oxide growth mechanism as well as the development of a simple analytical method to measure this oxide thickness is very important in aluminum rolling industry and this study aims to develop a spectroscopic method to determine the oxide thicknesses on the surface of the aluminum by using multivariate calibration and infrared spectroscopy.

Two main series of different aluminum alloys (3005 and 3003BZ) were selected in this study to develop a proposed methodology which is based on the combination of Fourier Transform Infrared Spectroscopy (FTIR) with Grazing Angle ATR accessory and chemometrics multivariate calibration techniques. In order to obtain oxide thickness values, X-ray Photoelectron Spectroscopy (XPS) was used and aluminum oxide (Al_2O_3) and magnesium oxide (MgO) thicknesses determinations were carried out by two different multivariate calibration models which are Genetic Inverse Least Squares (GILS) and Genetic Partial Least Squares (GPLS).

These models were able to predict Al_2O_3 and MgO thicknesses using FTIR that is faster, easier and cheaper to operate as well as from XPS. The correlation coefficients of XPS reference oxide thickness values versus FTIR-GATR based GILS and GPLS predicted values were better than 0.919 in range of 0 to 25 nanometers for Al_2O_3 and 0 to 35 nm for MgO. These results suggest that grazing angle FTIR-ATR spectroscopy may offer a simple and nondestructive alternative for quick determination of oxide layer thickness.

ÖZET

ALÜMİNYUM LEVHA VE FOLYOLARIN YÜZEYLERİNDE OLUŞAN ALÜMİNYUM VE MAGNEZYUM OKSİT KALINLIKLARININ BELİRLENMESİ İÇİN ÇOK DEĞİŞKENLİ KALİBRASYONA DAYALI YENİ BİR KIZILÖTESİ SPEKTROSKOPİK METOT GELİŞTİRİLMESİ

Alüminyum alaşımları doğal bir oksit tabakasını yüzeyinde barındırır. Ancak kimi yüksek sıcaklık ısıl işlemleri veya tavlama işlemleri sonrasında da atmosferik oksijen ve/veya nemi yardımıyla malzeme yüzeyinde daha düzensiz kristalografik yapılarda oksit tabakası meydana gelir. Bir alüminyum alaşımının yüzeyinde oluşan nanometre mertebesindeki oksit kalınlığının ölçümü için uygulanabilecek yöntemler, uzun numune hazırlama işlemleri ve X-ışınları fotoelektron spektroskopisi (XPS) gibi gelişmiş fakat pahalı ve zaman alıcı teknikler gerektirmektedir. Bu çalışmada, kızılötesi ve çok değişkenli kalibrasyon metotları kullanılarak alüminyum üzerindeki Al_2O_3 ve MgO kalınlıklarının ölçülebilmesi amaçlanmıştır.

Bu çalışma kapsamında iki farklı alüminyum levha (3005 ve 3003BZ) örneği seçilmiş olup, Grazing Angle ATR aksesuarlı Fourier dönüşümlü kızılötesi spekstroskopisi ile ölçümleri alınmıştır. Dört farklı süre ve beş farklı tavlama sıcaklığı kullanılarak hazırlanan levha ve folyoların spektrumları alındıktan sonra, referans Al_2O_3 ve MgO kalınlıkları XPS ile ölçülmüştür. Elde edilen verilere kemometrik çok değişkenli kalibrasyon yaklaşımı uygulanmış ve modelleme çalışmalarında Genetik En Küçük Ters Kareler (GILS) ve Genetik Kısmi En Küçük Kareler (GPLS) metotları kullanılmıştır.

Elde edilen modelleme sonuçları, hem Al_2O_3 hem de MgO kalınlığının belirlenmesinde başarıya ulaşılmış olup, XPS metodundan daha hızlı, basit ve kısa zamanda ölçüm yapma olasılığı sağlamıştır. GILS ve GPLS metotları ile elde edilen modellerin korelasyon katsayılarına bakıldığında, 0-25 nm arasında değişen Al_2O_3 kalınlığı ve 0-35 nm arasında değişen MgO kalınlıklarında, her iki model için de 0.919'den daha iyi modeller elde edilmiştir. Çalışma sonucunda FTIR-GATR spektroskopisinin oksit kalınlığını belirlemede hızlı ve tahribatsız ölçümler yapabildiği sonucuna ulaşılmıştır.

TABLE OF CONTENTS

LIST OF FIGURES

Figure **Page**

LIST OF TABLES

Table **Page**

CHAPTER 1

INTRODUCTION

Aluminum represents the second largest metal market in the world. It is used in wide range of industrial equipment as well as household items. The reason why aluminum is a preferred material in a great number of applications is that it has low density, high specific strength, high energy absorption characteristics, corrosion resistance in aggressive environments and attractive appearance.

Aluminum alloys contain a natural oxide layer. It is generally covered with a very thin (a few nanometers) natural oxide layer which protects it against further corrosive attack. However, that natural oxide layer is effected when aluminum alloys are exposed to annealing process during manufacturing. Also, the thickness of oxide layer can be increased consciously by some chemical or electrochemical reactions which is called "anodizing". Yet, in this study conducted with ASSAN Aluminum, anodizing process didn't apply to aluminum samples. Three production steps which are casting, production and annealing processes are applied to aluminum foils and sheets. There are two main objectives of annealing process, one of them is to give a shape and the other one is to get rid of the surface contamination. Although annealing operations are crucial for aluminum alloys, when the rolled aluminum sheets and foils are put on the thawing ovens, the oxide layer on the surface tend to grove depending on the thawing temperature, time and atmosphere due to the air exposure.(Snijders, Jeurgens, and Sloof 2002). These sheets and foils may contain not only $Al_2(OH)_3$, but also $Al(OH)_3$, (MgO) or spinels (Al-Mg-O) depending on the alloy composition. On sectoral basis, aluminum sheet and foil products that are included in this study are divided into two groups as shown in Figure 1.1.

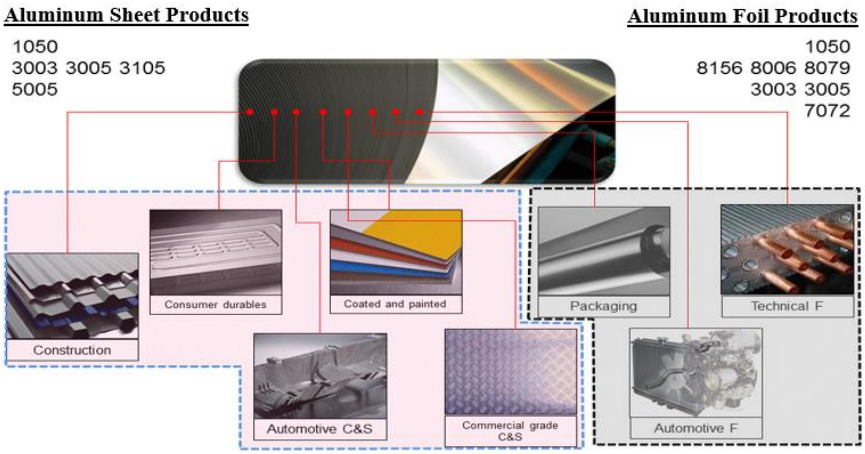

Figure 1.1. Various aluminum sheet and foil alloys that are used in this study.

Because outermost surface of aluminum has a significant importance in adhesion characteristics, the thickness of oxide layers on the end of the production lines is vital. In addition to that, to control the measurement of oxide thickness generated at any stage of production route and in the end-product is crucial for proper design of production process and achieving the desired surface properties in use. This study refers to two main groups of aluminum foils and sheets, which differs by their usage in industry.

The first of these main groups is the application of "Brazed Finstock". This application includes aluminum alloy foils (thickness ranging from 40 to 350 micrometers) which are used in automotive industry as heat exchangers, radiators and condensers. These mentioned aluminum foils are combined with a part of heat exchangers. This method is called "Brazing" and is carried out at high temperatures to reach the fusing point of the metal and to make a connection between fin and tube. Oxide thickness significantly influences the wetting characteristics on the aluminum surface and impair the mechanical bonding and heat transfer in heat exchanger systems (Figure 1.2)

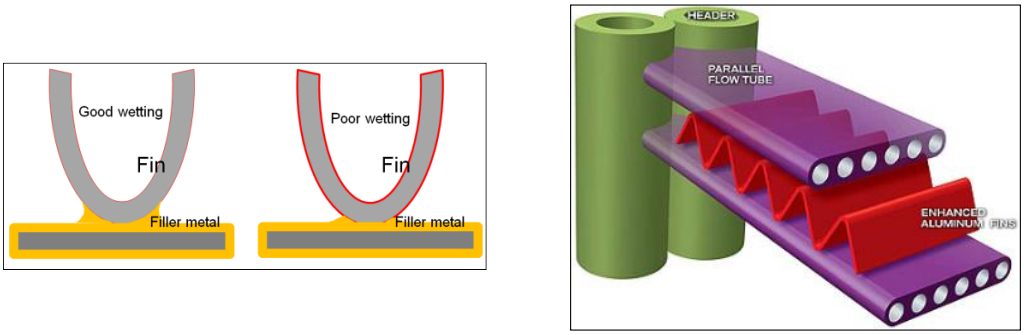

Figure 1.2. Schematic representation of oxide problems in heat exchanger systems.

The second of these main groups is the application of storage boxes. Because the thickness of oxide layer can change the surface tension of aluminum foils, presence of oxides (Al_2O_3, MgO) at the foil surface deteriorate the frictional conditions between the metal die-foil interface and results in failure during forming. Oxide layer which is formed during annealing process can be seen on the surface aluminum foil as a lighter color. However, it is impossible to notice when the thickness of the oxide layer is less but still effects the coating process.

The thickness of end-product is vital, especially for brazing method, and usually it should be lower than 50 Å. However, to determine accurate measurement of 50 Å or lower thickness of oxide layer, more specific techniques are needed. Although sophisticated techniques like X-ray Photoelectron Spectroscopy (XPS) (Jeurgens, Vinodh, and Mittemeijer 2006a) and Transmission Electron Microscopy (TEM) are suggested in academic area for the determination of oxide thickness, these methods take extended period of time. When the limited time of a defined product development process for a several products and several different process, it is unlikely to achieve determination of oxide layer in that limited time.

1.1. Structure and Scope of the Thesis

The first chapter of this thesis study describes the importance of aluminum in industry, problems due to oxide layer formation, the purpose of this research and a brief overview of literature review. The objective of this study is to develop a new infrared spectroscopic method based on multivariate calibration for the determination of aluminum and magnesium oxide thickness (in nanometer scales) on aluminum foil and sheets surfaces. In addition to that, it is also aimed to be able to model oxide formation on the surface of aluminum sheets and foils in the process of annealing. At the end, with the successful models the best annealing programs could be set for the desired aluminum products which have the lowest oxide thicknesses.

1.2. Literature Review

The number of studies for monitoring and detection of the thickness of the oxides formed on the aluminum sheet and foil product as an industrial measured are very few. In the most of the studies, samples were prepared in the laboratory conditions and there are no studies include samples of aluminum sheets or foils directly taken from the production process industrially. In a study by Franchy (2000), the growth of oxide, nitride and thin crystalline films of oxynitride were scanned on the surface of metals and metal alloys. This study particularly focused on the mechanism of the formation of oxide films on aluminum and aluminum alloy surfaces.

The most common method used for the determination of oxide layer on metal is X-ray Photoelectron Spectroscopy. King and Swartz (1987) used variable angle XPS technique to measure thickness of oxide layer (in angstrom) formed on the aluminum metal and this study was published for use in advanced undergraduate laboratory experiment in chemistry education course in 1987. They proposed variable angle XPS technique can be successfully applied on very thin oxide layers. Another study performed with XPS technique was carried out by Jeurgens et al. (1999). The thickness of the aluminum oxide layer by using XPS technique and the time-dependent change of the composition of the oxidation time were examined. The oxide-film thickness was derived from the primary zero-loss intensities of only the metallic and oxidic Al 2 p main peaks, utilising the known value of the intrinsic bulk plasmon excitation probability for the Al 2 p core-level photoelectron emission process. Snijders, Jeurgens, and Sloof (2002) investigated structure of thin-aluminum oxide films (<10 nm) from valence band spectra measured using XPS. Bare aluminum substrates, Al (4 3 1), was exposed to oxygen by changing time at different temperatures and thin aluminum-oxide films were produced and valence band (VB) spectra of oxide films were determined. At the end of the study, they suggest that surface of bare aluminum substrate is changing as a function of time, temperature and oxide film thickness. In different study for determination of aluminum-oxide layer was performed by Van Den Brand et al. (2004). A set of five different aluminum oxide layers which were made by oxidizing aluminum in a vacuum with an alkaline and acidic pretreatment and in boiling water, were investigated by using XPS. Determination was made by constrained curve-fitting of the O 1s peak and hydroxyl fractions of the aluminum oxide layers ranges change between 0.0 and 0.5. Study shows

that, angle resolved measurements could deduce the most of the oxides which are more enriched in hydroxyl groups against the surface region. Another study to determine the microstructure of very thin oxide film, Jeurgens, Vinodh, and Mittemeijer (2006b) tried to perform structural characterization of thin oxide layer using XPS method.

Prescott and Graham (1992) have studied about the formation of protective alpha-aluminum oxide (α-Al_2O_3) scales on alloys at high-temperature. To determine the oxidation of aluminum, Transmission Electron Microscopy (TEM) and Electron Diffraction were used. They suggested that there are some of major issues concerning the development of alpha-aluminum oxide scales, which are interaction between transport processes, the effect of grow stress, reaction kinetics and microstructures. Also, they mentioned alumina-forming systems are dependent on alloy compositions or experimental conditions. In another study, Dunlop and Benmalek (1997) investigated the role of characterization of surface in aluminum industry. It was recommended that especially XPS, Auger Electron Microscopy (AES), Secondary Ion Mass Spectroscopy (SIMS) and Electron Microscopy (TEM and SEM) techniques were widely used for the characterization of oxides. In another article written by Heilmann et al. (1999) is about determination of the pore size and vertical structure of nanoporous aluminum oxide membranes. They used Focused Ion Beam technology (FIB) and High Resolution Scanning Electron Microscopy (SEM) for observation of pore geometry of nanoporous aluminum oxide membrane and FIB technology also used for preparation of depth profile. Based on information about pore geometry, it is suggested that pore size distribution and inner surface the deposition of nanosized materials can be performed much more effectively.

In further study performed by French, Müllejans, and Jones (1998), Vacuum UV and Electron Energy Loss Spectroscopy (EELS) techniques has been studied to determine the optical properties of aluminum oxide. They emphasized that optical properties can be significantly changed by especially part the preparation, mode of data collection and data analysis. Another study about determination of aluminum oxide film thickness, composition and structure is performed by Le Pévédic, Schmaus, and Cohen (2008). They obtained a well-ordered ultrathin alumina film on the top of Ni(1 1 1) and the formation of this film was determined using Rutherford Backscattering Spectrometry (RBS) under channeling conditions, Nuclear Reaction Analysis (NRA), Auger Electron Spectroscopy (AES) and Low Energy Electron Diffraction (LEED). It was concluded that regardless of the thickness, the structure of oxide layers have a similar compositions.

Another study include the thickness of anodized aluminum-magnesium oxide was studied by Habib (2010). The annealing effect for thickness of aluminum-magnesium oxides and their electrochemical behavior were examined by the electrochemical impedance spectroscopy. Garabagiu and Mihailescu (2011) tried to determine the thickness of anodic aluminum oxide films and investigate their optical properties. They determined dissolution rate of the anodic aluminum oxide barrier by several successive partial removal of barrier layer of thin film. They used a new, simple electrochemical setup and the transmission spectrum of alumina for determination and they observed that thinning the alumina membrane causes some changes in the optical transmission spectrum and that changes provide information on the dissolution rate of alumina barrier layer. In another article about aluminum thin film thickness measurement is written from Movla and Babazadeh (2014).They using low energy electron beam for estimating the Al thin film thickness measurement. Simulation results show that maximum transmitted electrons versus Al layer thickness has a parabolic relation and by using the obtained equation, it is possible to estimate unknown thickness of the thin film Al layer.

In addition to those techniques, there are few studies in literature using infrared spectroscopy for characterization of aluminum oxide and film thickness measurement. In one of these studies, FTIR reflectance spectroscopy techniques were used for determining the composition of oxide film on the metal surface Lefez et al. (2007). In this article, it was emphasized that using a combination of FTIR spectroscopy and microscopy provides a major advantage compared to other methods for monitoring the surface of aluminum oxide without decomposition. Raacke, Giza, and Grundmeier (2005) also studied with FTIR reflectance spectroscopy technique for analyzing the composition of plasma-treated metal surface.

CHAPTER 2

INSTRUMENTATION

2.1. X-Ray Photoelectron Spectroscopy (XPS)

For quantitative analysis of surface composition and depth, X-ray photoelectron spectroscopy (XPS) is a popular technique despite of high cost of the device, expensive maintenance and time consuming procedure. XPS is, however, very sensitive and capable of distinguishing different chemical compositions of the surface while it is also possible to involve sputtering of the surface so that the composition of inner layers along with the depth can be determined. This technique is also applicable to almost all elements. Figure 2.1 shows the schematic diagram of XPS working principle.

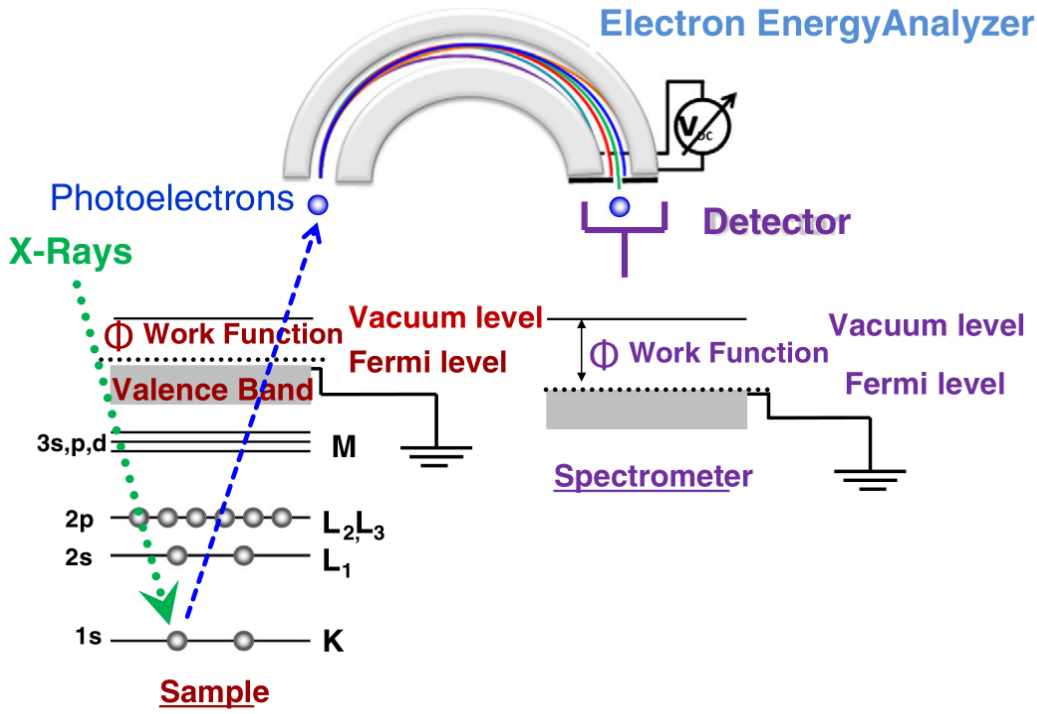

Figure 2.1. Schematic diagram of the XPS technique.
(Source: Sezen and Suzer, 2013).

The underlying principles of XPS begin with the Einstein's famous Nobel winning discovery photoelectric effect given in the equation 2.1.

$$BE = h\nu - KE \tag{2.1}$$

XPS exploits the power of the X-ray photons to eject the core electrons of an atom from the inner shell. The knowledge of the incident light's energy (hν) and the kinetic energy (KE) of the electron measured by the detector allows the calculation of binding energy (BE) of the specific electron using the formula given above. This binding energy is specific to the orbital of each element and peaks can be identified using a reference table. The determination of the chemical properties of an element is provided by the fact that the binding energy varies with these properties such as oxidation state, mostly because of the changes in Coulomb interactions and shielding effects as shown in Figure 2.2.

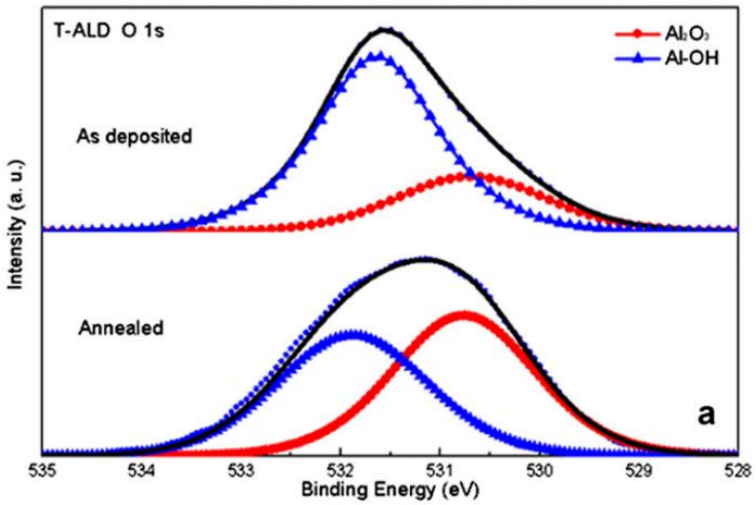

Figure 2.2. O_{1s} XPS spectra of Al_2O_3 films. The solid black lines represent the fitted curves.
(Source: Xiang et al., 2015)

Due to the quantized energy loss of ejected electrons passing through the layers, the XPS can only provide reliable results up to 10nm of depth in single "run" which usually takes roughly 15 minutes. The sputtering with a charged noble gas such as Ar^+, on the other hand, removes the surface layer by layer and reveals information of the inner surface. The ion beam is usually not focused on a single point but rather on a surface that is larger than the diameter of the beam to avoid crater formation which decreases the

depth resolution. During the etching process, some of the ions may stay embedded to the surface while the ions may induce a reaction between the impurities in air such as water, oxygen and the surface hence the quality of the vacuum increases the resolution. It is also possible to derive a formulation for determining etching rate from the number of atoms removed and the thickness of certain number of atoms in the specific area.

$$\text{Rate of removal of surface atoms} = (YI)/e \tag{2.2}$$

where Y is the sputtering yield, I is the ion beam current (amp), charge of the ions (coulomb)

$$\text{Number of atoms in the area of interest} = A\,(d.N/w)^{2/3} \tag{2.3}$$

$$\text{Layer thickness} = A\,(w/d.N)^{1/3} \tag{2.4}$$

where A is the area (cm^2), d is density, N is Avogadro's constant and w is the atomic weight. This formula assumes the atoms are in a cubic array. Combining them simplifies to:

$$\text{Etching rate} = IYw/(AedN) \tag{2.5}$$

The ejected electrons are separated by their kinetic energy and then detected. The number of electrons detected with a corresponding binding energy in a certain amount of time accounts for the peak heights and is expected to be linearly correlated with species to be analyzed quantitatively.

2.2. Fourier Transform Infrared (FTIR) Spectroscopy

Infrared spectroscopy was first mentioned by Sir William Herschel in 1800. It deals with the infrared region of the electromagnetic spectrum (wavelength from 700 nm to 1 mm) and it is based on the vibrations of the atoms of a molecule of interest. Infrared spectrum is generally subdivided into three regions which are near-IR, mid-IR and far-IR (Holler, Skoog, and Crouch 2007) as shown in Table 2.1. IR spectrum represents either

the infrared radiation which is absorbed or transmitted by the sample. Because each different material is a unique combination of atoms, it is impossible for two compounds produce the exact same infrared spectrum. That's why infrared spectrometry provides a positive identification which is called qualitative analysis.

Table 2.1. IR Spectral Regions.

Region	**Wavelengths, μm**	**Wavenumbers, cm^{-1}**
Near	0.78 to 2.5	12800 to 4000
Middle	2.5 to 50	4000 to 200
Far	50 to 1000	200 to 10
Most used	2.5 to 15	4000 to 670

In early 1980s, instrumentation of IR spectrometry was based on grating monochromators or prisms which are called dispersive type instrumentation. With the invention of interferometers by Albert Abraham Michelson, Fourier Transform Infrared (FT-IR) spectrometry was developed in order to overcome the limitations generated by dispersive instruments. General FT-IR diagram is shown in Figure 2.3.

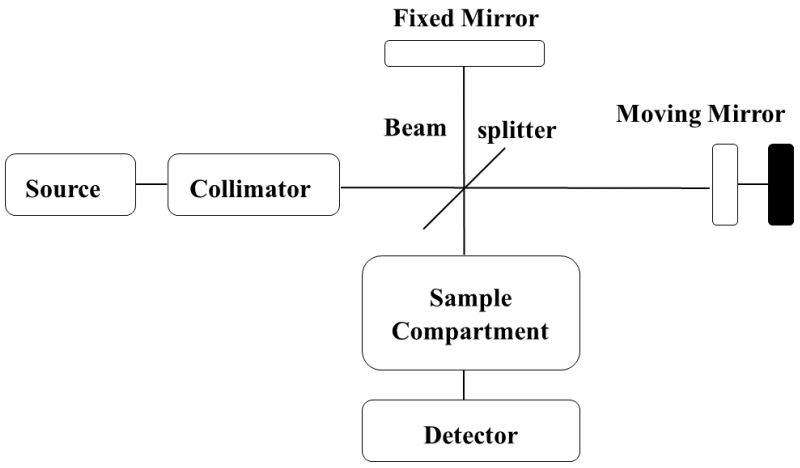

Figure 2.3. A general Fourier Transform Infrared (FT-IR) spectrometer block diagram.

Fourier transform type infrared spectrometers caused dramatically change for mid-IR instrumentation and as a result mid-infrared (MIR) is the most used region for quantitative and qualitative analyses. An infrared spectrum which is collected from mid-IR region has two main regions which include functional groups region (3600-1200 cm^{-1}) and the fingerprint region (1200-600 cm^{-1}). FT-IR spectra provide identification of unknown material, determination of quality or consistency of sample and also determination of amount of components in a mixture. The main reasons of using FT-IR spectroscopy over other techniques can be listed as:

- It is a non-destructive technique
- It has a good precision
- It doesn't need external calibration
- It has high speed of collecting data
- It has lower S/N ratio
- It is mechanically simple technique

2.3. Grazing Angle Attenuated Total Reflection (GATR)

The main difference between reflection and transmission FT-IR techniques is the challenging sample preparation of transmission FT-IR even though transmission FT-IR techniques are convenient for solids, liquids and gases. Reflection FT-IR techniques, however, require minimal sample preparation and can be used to analysis of not only solids and liquids, but also gels or coatings (Holler, Skoog, and Crouch 2007).

Classical FT-IR techniques such as transmission or ATR techniques generally measuring coatings or samples on samples where the thickness of sample is three times more (Kempfert et al.). Yet, grazing angle reflection-absorption techniques have been used to measure very thin films of material on reflective surfaces. The main advantage grazing angle reflection-absorption techniques over other reflection-absorption techniques is the incidence and reflectance of the infrared beam where classical techniques involve an angle about 10-30 degrees and grazing angle procedure uses an incidence and reflectance angle of about 75-85 degree. Therefore, the infrared beam passes through a much longer path through the sample than with small angles and creates a stronger spectrum (Mirabella 1998). In theory, reflection-absorption spectrum is collected in most efficient way using higher angle of incidence which can be achieved

when the parallel light comes with angle to the surface gives evaluable absorption. A schematic representation of beam path of grazing angle specular reflectance that is used for this study is shown in Figure 2.4.

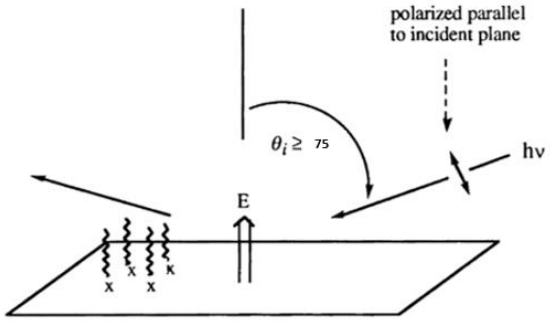

Figure 2.4. A schematic representation of the GATR-FTIR experiments (modificated version) (Source: Ulman, 2013)

The working principle of grazing angle specular reflectance shown in Figure 2.4. Samples are simply placed face down over the top and spectrum obtained from aluminum film is collected. Spectra collected from the surface of the aluminum samples are enhanced by using P-polarized light, with the electric field vector upright to the sample surface. Other features of 80Spec grazing angle used in this study is that it has dual polarizer mounts for incoming and outgoing beam and it has baseline mount design for stable operation and collection of high spectra. Also, it fits to all FTIR spectrometers.

In a study about applying grazing angle attenuated total reflectance Fourier transform infrared spectroscopy (GATR-FTIR) to demonstrate doping haftnia with Dy or Sc, Hardy et al. (2009) mentioned that GATR-FTIR provides a highly sensitive, cheap and quick characterization of metal oxide layer which is ultrathin and have different compositions. In this study, the potential of GATR-FTIR was demonstrated for characterization of high-*k*.

In another study which is about determining the biocompatibility of materials, quartz crystal microbalance (QCM) and GATR-FTIR spectroscopy were applied for data analysis to discuss protein adhesion. Thanks to GATR-FTIR spectroscopy they observed that there were conformational changes of adsorbed proteins depending on incubation time. The researchers demonstrated that conformation and binding rates of bound proteins

through protein surface were influenced by simple tailor-made mono-chemical surfaces positively (Roach, Farrar, and Perry 2005).

In a study, ATR, GATR and transmission mode FTIR spectroscopy were used to consider the orientation of peptide nanotubes in a suitable liquid environment of organized phospholipid multibilayers. Structural characteristic of the related peptide nanotubes were found out in liquid environment with ATR-IR firstly. After that GATR-FTIR and transmission mode FTIR spectroscopy were used to support its results. Additionally, membrane spanning orientation and transport competent of peptide nanotubes were supported in this study (Kim, Hartgerink, and Ghadiri 1998).

Primera-Pedrozo et al. (2009) were investigated construction a methodology by using Reflection Absorption Infrared Spectroscopy (RAIRS) in conjunction with Fiber Coupled Grazing Angle Probe for detection and quantitative determination of explosive residues (TNT, DNT, HMX, PETN, and Tetryl etc.) on metallic surfaces. Partial least square (PLS) method was used for analyzing the data quantitatively. In order to compare linear multivariate analysis peak areas were also used in this study. Additionally the target treat chemicals were determined according to the fingerprint region of the spectrum for each compound and their detection limits were calculated.

CHAPTER 3

CALIBRATION METHODS

Calibration is the mathematical method of finding the relation between two set of variables one being the output from an instrument(x) and the other one being properties of the sample(c). This relation, then, can be used to predict the properties of the sample from the device output. For instance, quantitative analysis with NIR spectroscopy can be established by using solutions with different concentrations and with their NIR spectrums to find the coefficients that can be used to calculate the concentrations of the new (unknown) solutions from their spectrums.

When the properties of a sample are expected to be linearly correlated to the instrumental response(s), linear calibration methods can be used. These calibration methods can be divided into two main groups:

- Univariate Calibration
- Multivariate Calibration

Univariate calibration aims to obtain a model for a single property of the sample using a single variable such as the wavelength with highest absorbance from a full spectrum whereas with multivariate calibration multiple responses from a single or multiple detectors are used to model the multiple properties of a sample.

The abbreviations used to define matrix sizes are given below:
n: Number of experiments
p: Number of variables
m: Number of compounds

3.1. Univariate Calibration

3.1.1. Classical Univariate Calibration

The most common and simple calibration method is classical univariate calibration and is very similar to the Beer-Lambert Law:

$$x = \mathrm{C}.\mathrm{S} \tag{3.1}$$

In this equation, x is the absorbance at single wavelength and C is the concentration matrix, while S is the regression coefficient. Classical univariate calibration assumes that the instrumental output is a function of sample's property and it aims to fit a line to the data that minimizes the errors perpendicular to independent variable such as concentrations as shown in Figure 3.1.

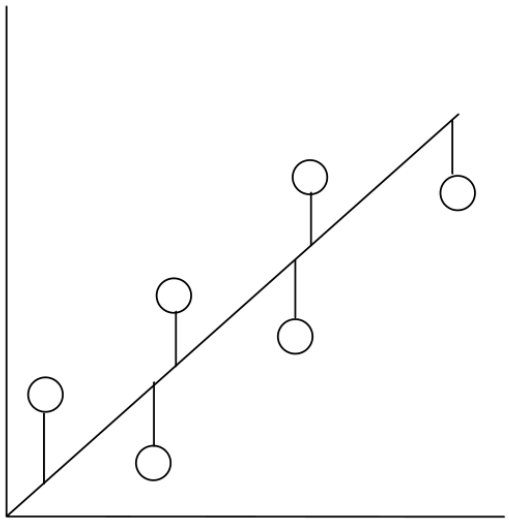

Figure 3.1. Classical Univariate Calibration Line
(Source: Brereton, 2003) .

In order to solve the regression problem and to find s, pseudo-inverse can be used:

$$x = \mathrm{C}.\mathrm{S} \tag{3.2}$$

$$\mathrm{c}'.\mathrm{x} = \mathrm{c}'.\mathrm{c}.\mathrm{s} \tag{3.3}$$

$$(\mathrm{c}'.\mathrm{c})^{-1}.\mathrm{c}'.\mathrm{x} = \mathrm{s} \tag{3.4}$$

The purpose of multiplication of both side with c^t is making the concentration vector a square matrix so that taking inverse becomes possible. This solution can also be expressed in terms of summation:

$$s \approx (c'.c)^{-1}.c'.x = \frac{\sum_{i=1}^{l} x_i c_i}{\sum_{i=1}^{l} c_i^2} \tag{3.5}$$

Since the usage of software became a more popular and common way of solving these kind of problems, expressing the solution in terms of matrices is more convenient even though both equations are equivalent.

To predict the modelled property, the formula below can be used:

$$c = \frac{x}{s} \tag{3.6}$$

3.1.2. Inverse Univariate Calibration

Unlike the classical univariate calibration, inverse univariate calibration assumes that a property of the sample is a function of a response. This often makes the usage of inverse calibration more appropriate:

- While the classical univariate calibration assumes all the errors are in the responses obtained from device, inverse calibration assumes the source of errors lies in concentrations. The preparation of samples with specific concentrations involves usage of containers such as graduated cylinder, volumetric flask as well as dilution. The accuracy of these tools haven't increased much relative to the improvements in devices and the procedure of sample preparation often includes human errors.
- Generally, the main purpose of calibration is to predict properties from the responses rather than vice-versa.

The general form of inverse calibration is given below:

$$c = x.s \tag{3.7}$$

The solution of this equation to find s is very similar to the previous solution:

$$c = x.s \tag{3.8}$$

$$x'.c = x'.x.s \tag{3.9}$$

$$(x'.x)^{-1}.x'.c = s \tag{3.10}$$

Inverse univariate calibration tries to minimize the errors perpendicular to the responses as shown in Figure 3.2.

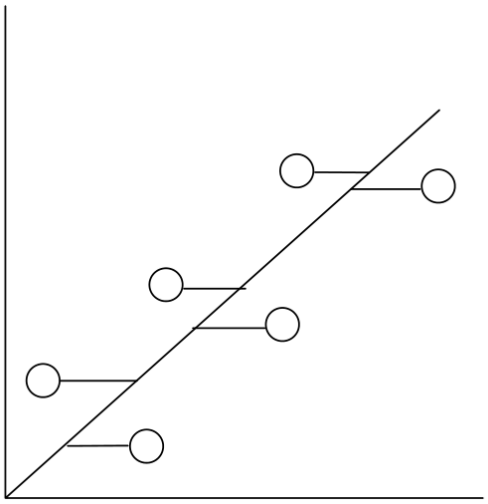

Figure 3.2. Inverse Univariate Calibration Line.
(Source: Brereton, 2003).

3.2. Intercept Term

So far no regression parameter to reflect the baseline of the responses was given yet the addition of this parameter may increase the predictive power of calibration model dramatically when a constant response is observed even in the case of absence of related property. One way of adding this parameter is given in equation 3.11.

$$c = b_0 + b_1.x \tag{3.11}$$

In order to find b_0 which is the intercept term and b_1 which is the slope term, it is more convenient to write this equation in vector or matrix form given in the equation 3.12.

$$c = x.b \tag{3.12}$$

In this case the c is the concentrations, X is a matrix with two columns the first column consists of ones, the second column is responses, and b is a single row two column vector that consists of b0 and b1 respectively. The solution then becomes:

$$(X'.X)^{-1}.X'.c = b \tag{3.13}$$

The other way of adding intercept is mean centering the data. In this procedure, the mean of properties is subtracted from each property and the mean of responses are also subtracted from each response. This provides an equivalent approach to the previous way while this method provides a simpler calculation. In order to predict the properties, however, one should mean center the responses and add the previous mean of the properties to the predicted values.

3.3. Multivariate Calibration

In some cases, a single variable may not be enough to describe the sample's parameter of interest. This may happen, for example, when the compound of interest consists of several species each having a different wavelength of maximum absorbance. The other concern is random interferences and noises. Using multiple wavelengths yields better results most of the time due to the averaging of useful information in absorbance as well as noises. Also, in order to determine multiple components at once, multivariate calibration can be used.

There are, however, some limitations of these calibration methods. To obtain a reliable model, the number of variables should be equal to at least the number of compounds. The number of observations should also exceed the number of variables.

3.3.1. Classical Least Squares (CLS)

Classical least squares calibration is the multivariate form of classical univariate calibration and is very suitable when a complete spectrum is to be modelled as given in the equation 3.14.

$$X = \mathrm{C}.\mathrm{S} \tag{3.14}$$

In this equation, X is n x p matrix of n experiments and p variables, C is a n x m matrix of n experiments and m components and S is a m x p matrix that contains regression coefficients. The solution to find S involves pseudo-inverse equation 3.15 is used.

$$(\mathrm{C}'.\mathrm{C})^{-1}.\mathrm{C}'.\mathrm{X} = \mathrm{S} \tag{3.15}$$

In order to obtain a reasonable model, all properties of the sample such as concentration of each species should be used when modelling.

3.3.2. Inverse Least Squares (ILS)

Inverse least squares, as in inverse univariate calibration, defines the properties of a sample as a function of the response:

$$\mathrm{C} = \mathrm{X}.\mathrm{S} \tag{3.16}$$

In this equation, X is n x p matrix, C is a n x m matrix, and S is a m x p matrix. To obtain S following formula is used:

$$(\mathrm{X}'.\mathrm{X})^{-1}.\mathrm{X}'.\mathrm{C} = \mathrm{S} \tag{3.17}$$

Even though ILS can be used to model a single component in a sample without the knowledge of the others, the calculation of pseudo-inverse is computationally expensive and prone to multicollinearity issues which lead to overfitting. To overcome this issue, feature selection methods such as genetic algorithm can be employed.

3.3.3. Partial Least Squares (PLS)

Partial least squares method combines the advantages of ILS and CLS while avoiding their cons. Unlike CLS, in order to apply PLS there is no need for the knowledge of all interfering species and PLS doesn't require variable exclusion since it projects the combination of responses and dependent variables to a new smaller dimensional space. In a noise free case, the whole data can be explained in only a few latent variables. In addition to these, while other calibration methods assume the errors are either in responses or properties of samples, PLS accounts for both cases (Geladi and Kowalski 1986) .

While there are two versions of PLS which are PLS1 and PLS2, in this study PLS1 was used since it provides better predictive power. The PLS1 decomposes the data so that:

$$X = T.P + E \tag{3.18}$$

$$c = T.q + f \tag{3.19}$$

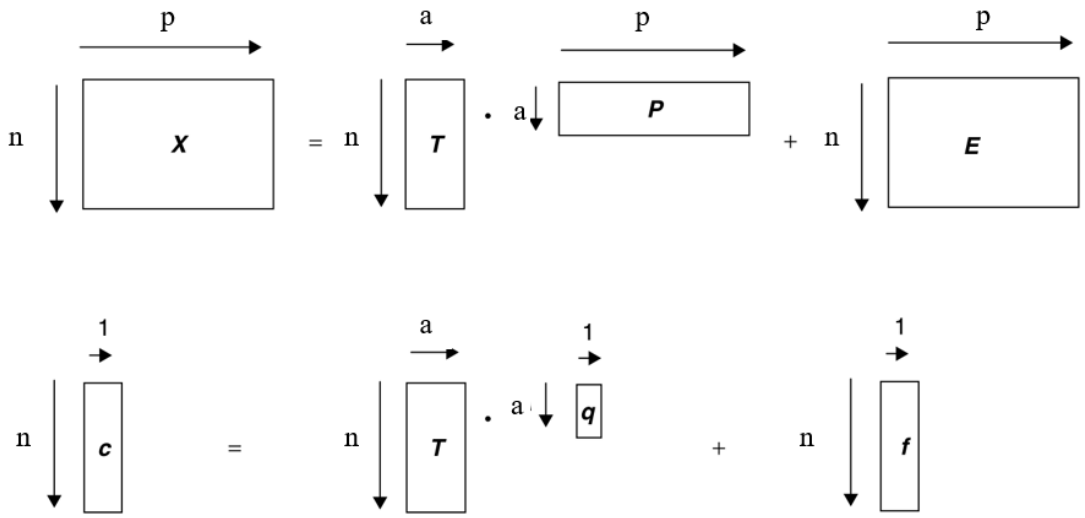

Figure 3.3. The size of matrices used in PLS.

X is the matrix of responses, P is the loadings of responses, E is the residuals of responses while c is the property of interest, q is the loadings of property and f is the residuals. The number of latent variables are indicated with a. Finally T is the scores matrix and is used to model the data with an ILS model. The new samples can then be predicted by projecting the new data and using that ILS model.

One of the most important aspects of PLS is the selection of number of latent variables (similar to PCA models). One method of optimizing this number is using the PRESS values.

$$PRESS = \sum_{i=1}^{m} (\hat{c} - c_i)^2 \tag{3.20}$$

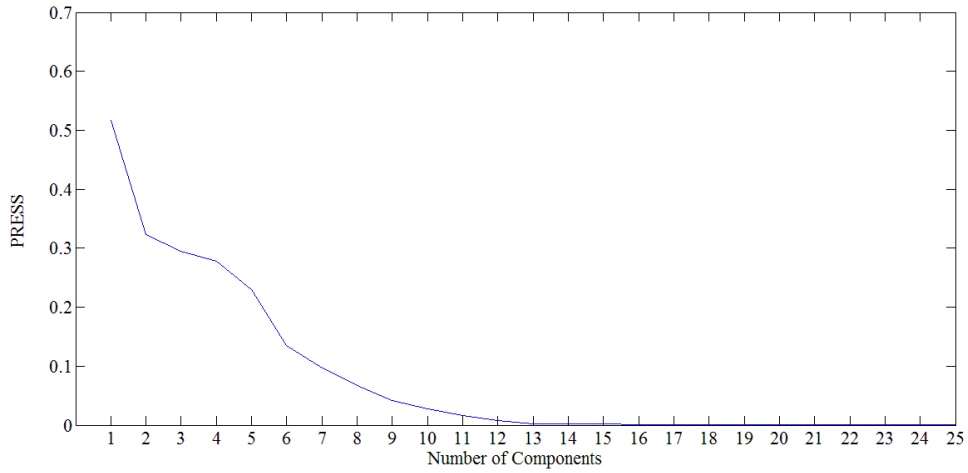

Figure 3.4. An example of a number of components vs. PRESS plot that is obtained from PLS modelling of Al_2O_3.

As a general rule of thumb, the number of components are chosen before the increment in PRESS is observed or when the PRESS stops decreasing. The addition of extra latent variables may cause modelling of interferences.

3.3.4. Genetic Inverse Least Squares (GILS)

GILS is an iterative feature selection algorithm that combines genetic algorithm and ILS. Despite the popularity of ILS alone, the multicollinearity problem forces the usage of many wavelengths which may cause overfitting of the model. It is also not

always possible to know which response from the device carries the information that is related to the sample's property of interest, especially in complicated spectrums. Since trying each and every N combination of variables, that is more than 3000 in a NIR spectra for instance, is not feasible, developers of genetic algorithm are focused on creating a new method which is inspired and based from Darwin's evolution theory (ÖZDEMİR and Öztürk 2004).

The genetic algorithm involves 5 steps which are initialization of gene population, fitness assignment of the population, selection of genes to be breed, cross-over and handling of mutations, and replacement of the new genes with the old ones.

The terminology used in genetic algorithm originates from biology. A gene is a set of variables and in this study variables are absorbances at certain wavelengths. Cross-over refers to exchange of variables between selected gene pairs. A mutation is considered to be a harmful one and refers to the excess number of variables in a gene so that it may cause possibly overfitting. The fitness of a gene is presentation of a gene's success that is calculated by the means of cross-validation.

3.3.4.1. User Defined Options

The problem of finding the best combination of variables is very similar to the search of global minima. In this manner, there are many options to adjust the parameters of genetic algorithm to achieve a desired computational time and the expected quality of the model. The first options provide the user to adjust number of genes in the population. Since the process of cross-over happens pair-wise this number must be an even integer and is proportional to the computational cost.

Another option is the coefficient of determination threshold for the initialization of the new genes and is useful for eliminating possible highly uncorrelated genes. This value must be between 0 and 1. Choosing a low value hastens the initialization step while increases the risk of constructing a bad series of genes which may ultimately cause a bad modelling.

The number of iterations is used to decide how many times the genes will be subjected to breeding and replaced with the old genes. During the iterations, the number of variables in a gene may increase or decrease too much to be carried on to the next

iteration and this number is also optional and can be any integer. Since the GILS ultimately averages fittest genes, the number of runs must be chosen to a point where a good tradeoff between computational cost and success of the final model.

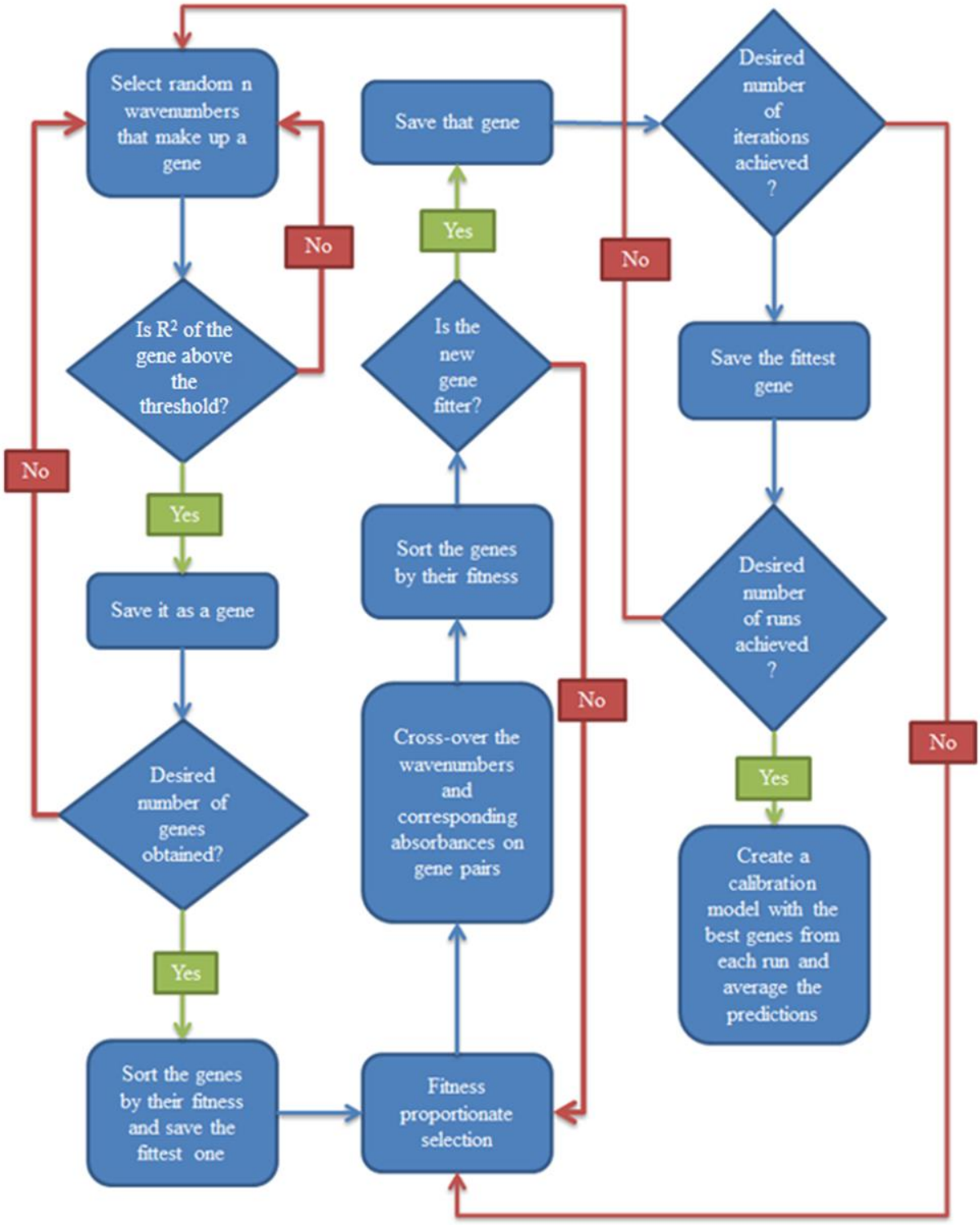

Figure 3.5. Flowchart of genetic algorithm.

3.3.4.2. Initialization of Gene Population

Firstly, a certain number of variables are selected to construct a gene. The number of variables is random yet should not exceed the number of experiments due to the nature of ILS. That gene is then subjected to the cross-validation for the determination of its fitness and coefficient of determination. A gene in this study can be defined as a set of absorbances at specific wavenumbers:

$G = [A_{489}\ A_{2618}\ A_{2003}\ A_{769}\ A_{1459}]$

The coefficient of determination is calculated using the formula given in the equation 3.21.

$$r = \frac{n\ \sum xy - (\sum x)(\sum y)}{\sqrt{n(\sum x^2) - (\sum x)^2}\ \sqrt{n(\sum y^2) - (\sum y)^2}} \tag{3.21}$$

The predicted values to be used in the calculation of R^2 are obtained by leave one out cross validation. This procedure removes a single sample from the whole data along with its response, then the rest of the data, using only the variables indicated by the gene, is used to create an ILS model. The prediction of a single sample is then takes place by this model and the deleted sample is put back. This procedure is repeated until all the property of samples are predicted.

If a gene is above the R^2 threshold, it is preserved and otherwise disposed. Populating the gene pool continues until the given number of genes which can meet the R^2 criteria are obtained. These genes are also the first parent genes.

3.3.4.3. Evaluation of the Population

As in all kind of genetic algorithms, there must be a fitness definition of genes. The fitness, in this case, is established to be inversely proportional to the standard error of cross-validation (SECV) that is calculated by comparing the real values and the values obtained from ILS models during the cross-validation where the selected variables are contained in the gene as shown in the equation 3.22.

$$\text{Fitness} = \frac{1}{\text{SECV}} \tag{3.22}$$

And SECV is defined as:

$$SECV = \sqrt{\frac{\sum_{i=1}^{m}(c_i - \hat{c}_i)^2}{m-2}} \tag{3.23}$$

Where m is the number of samples, c_i is the property of the sample while $\hat{c}$ is the prediction. The fitness of each gene is saved and the genes are sorted in ascending order by their finesses.

3.3.4.4. Selection of the Parent Genes for Breeding and Mating

While there exist many methods for selection of the genes to breed such as top-down and tournament selection, roulette wheel method was used in this study. This method assigns each gene an area proportional to their fitness in a roulette wheel. The wheel is then spun number of genes times. The genes that are selected by this random spinning are then paired top-down so that the first selected gene is matched with the second, third gene is paired with the forth gene and so on.

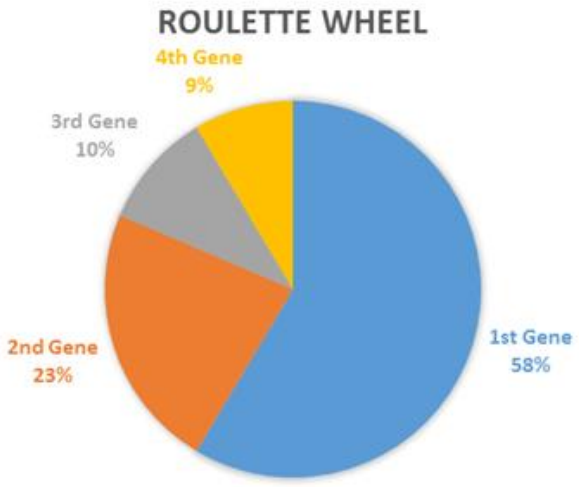

Figure 3.6. Example of Roulette Wheel selection method.

3.3.4.5. Cross-Over and Mutations

In this step, the selected parent gene pairs are cut from the middle to exchange variables to form a new pair of offspring:

Parent Gene Pair:
G1 = [A_{598}, A_{3457} # A_{2706}, A_{2451}]
G2 = [A_{918}, A_{544}, A_{857} # A_{1442}, A_{1961}, A_{3752}]
Offspring:
NEWG1 = [A_{598}, A_{3457}, A_{1442}, A_{1961}, A_{3752}]
NEWG2 = [A_{2706}, A_{2451}, A_{918}, A_{544}, A_{857}]

The # symbol indicates the position where the genes are broken. After each pair of parent genes are subjected to cross-over, the fitness of each gene is determined as explained in evaluation part. During the cross-over, there is a slight chance of a gene to exceed the given number of variable threshold or to become too small to model the data. In this case, this gene is replaced with a new one with the process explained in initialization of gene population part.

3.3.4.6. Replacing Parents with Their Offspring

The fitness of the best offspring is compared the older fittest gene and if the offspring is fitter, this gene replaces the fittest gene to be stored along with its fitness while all the parent genes are replaced with the offspring regardless of their fitness. The whole procedure is repeated until the defined number of iterations are reached.

As a result of the whole procedure starting from initialization and ending with the last iteration is called a run. Each run yields to its fittest gene and the final model obtained from GILS is defined to be all of these best genes. The prediction of the unknowns is carried out by prediction with the fittest genes using ILS followed by averaging of the results.

3.3.5. Genetic Partial Least Squares (GPLS)

GPLS algorithm uses partial least squares unlike the GILS method which employs ILS for fitness determination and predictions. The main differences are listed below:

- PLS requires the number of principle components to be optimized. The optimum number of components is determined using cross-validation with increasing number of components. The first point before the fitness decrement observed is assigned to be the best number of components and saved with the gene.
- The absence of multicollinearity due to the nature of PLS allows single point cross-overs to be from random places rather than only from the middle of the genes. This allows better shuffling of variables among genes.

CHAPTER 4

EXPERIMENTATION

4.1. Initial Studies

This thesis study is a part of joint project between ASSAN Aluminum San. Tic. A.Ş. and Prof. Dr. Durmuş ÖZDEMİR. ASSAN Aluminum produces a number of different alloyed aluminum sheets and foils for various industrial applications from automotive to packing. Each of these alloys may have externally added metals such as magnesium and zinc depending on the type of application for finished products. The sheets and foils are produced by a rolling process which is followed by annealing in order to give desired strength and mechanical properties. In addition to this, annealing is also used to remove rolling oil residuals on the surface of rolled sheets and foils. A natural oxide layer is formed right after rolling process and this oxide layer may to an undesired magnitude depending on the annealing time and temperature. If oxide thickness on the surface of rolled products exceeds to a certain level (10-15 nm) serious problems occurs in some industrial applications such as 'Brazed Finstock' at which the presence of oxide layer impair mechanical bonding and food packing applications where storage boxes are broken during the press. Therefore, there is a need for analytical method to determine the oxide layer formation mechanism as a result of annealing time and temperature. This study is focused on first evaluate the contribution of time and temperature on the oxide layer growth during annealing and develop a statistical model to predict the magnitude of oxide thickness depending on these factors. Second aim of this thesis is to develop an infrared spectroscopic method coupled with multivariate calibration for the quantitative determination of oxide thickness (Al_2O_3 and MgO).

For this purpose, four different aluminum alloys namely 3005, 3105, 5005 and 5754 were selected. These alloys are used in certain applications and have different compositions and due to the commercial reasons detailed formulations of these alloys are not given here. From four different aluminum alloys, 5754 series of aluminum alloys were selected due to having high tendency to form oxides on the surface for initial studies. In order to evaluate the effect of time and temperature during annealing, this alloys were exposed to four different annealing times (1 hour, 3 hours, 8 hours and 12 hours) and five

different annealing temperatures (300 ^{o}C, 350 ^{o}C, 380 ^{o}C, 450 ^{o}C and 500 ^{o}C). A total of 20 samples were obtained from the combination of four annealing times and five annealing temperatures. At the initial stage of the project the grazing angle ATR accessory was not available neither in ASSAN Aluminum nor in any other place in Turkey. As a results, these 20 samples were sent to Innoval Technologies which is formerly an independent aluminum industry consulting company based in England and now is a part of Danieli Group. FTIR spectra of these samples were recorded in triplicate by using 80 degree fixed angle Grazing Angle ATR accessory in the wavenumber range from 5000 cm^{-1} to 600 cm^{-1}. Although the FTIR spectra of these samples were recorded at the time, the consulting company did not provide any reference oxide measurement on the same samples. Therefore, the only available information was these spectra and annealing conditions. The details of this initial study are given in results in discussion section.

4.2. Experimental Studies

While a large number of aluminum alloys were selected, chemometric multivariate calibration modelling studies were carried out in two subtitle. First sub-heading includes 3005 series of aluminum alloy which has a magnesium content (added during casting) and second sub-heading includes 3003BZ series of aluminum alloy which has no added magnesium content (except any impurities in unrolled aluminum). In this regard, a number of 21 samples were prepared for each series of aluminum alloys mentioned above (3005 and 3003BZ). One of these samples (not exposed to any annealing process) had been accepted as natural oxide formed sample and remain 20 samples were subjected to five different annealing temperature (300, 350, 400, 450 and 500 ^{o}C) and four different annealing time (1, 3, 5 and 8 hours). Then, Grazing Angle Attenuated Total Reflectance (GATR)-FTIR spectra of 21 samples were recorded by using Perkin Elmer Frontier FTIR Spectrometer coupled with GATR accessory in the wavenumber range of 4000-600 cm^{-1}. Samples were placed on the top of Grazing Angle ATR accessory in two different configurations which were perpendicular to the rolling direction and parallel to the rolling direction. GATR-FTIR spectra of two series alloys were obtained in both directions. Immediately after, samples were drifted apart with air and sent to Prof. Dr. Şefik SÜZER's laboratory (Bilkent University, Department of Chemistry) to determine reference oxide thickness values which are carried out by X-Ray Photoelectron

Spectroscopy (XPS). The fact that, XPS measurements are quite time consuming and expensive, only those mentioned 40 samples (20 from 3005 series and 20 from 3003BZ series) were analyzed by XPS. On the other hand, a number of aluminum alloys that are somewhat similar to 3005 series alloy were also studied at different annealing time and temperature. These alloys were 3105, 5005, 5052 and 5754 series alloys and they were also annealed at the temperatures and times given above. Similarly, 1050, 3003, 8006 and 8156 series alloys which are similar in composition to 3003BZ were also studied. The GATR-FTIR spectra of these samples were also collected but no XPS measurements has been performed on these additional alloys. Therefore, these samples were only used to test the performance of the multivariate calibration models developed based on 3005 and 3003BZ series aluminum alloys. For each series alloys (3005 and 3003BZ) two different calibration modelling studies were performed with the GATR-FTIR data which are collected perpendicular to the rolling direction and parallel to the rolling direction.

4.3. Data Processing

Two-way analysis of variance (ANOVA) was performed by using Microsoft Excel (MS Office 2010, Microsoft Corporation) to determine the effect of annealing temperature and annealing time on the growth of oxide layer thicknesses (Al_2O_3 and MgO). Also, multiple regression analysis was applied to the same data after normalizing the factor levels by using Minitab 16 Statistical Software (State College, PA: Minitab, Inc.). In addition to these, Microsoft Excel was also used to generate univariate calibration models. Genetic Inverse Least Squares (GILS) and Genetic Partial Least Squares (GPLS) multivariate calibration methods were coded in Matlab programming language (Matlab R2016a - MathWorks Inc., Natick, MA). Both method were performed with the option of ‘’Leave-One-Out Cross Validation’’ mode.

CHAPTER 5

RESULTS AND DISCUSSION

5.1. Initial Study Results

Details of experimental procedures about the initial studies has been given in the above section. Over there, it was mentioned that there were a total of 20 synthetically annealed 5754 alloy at four different time and five different temperature. GATR-FTIR spectra of these samples are given in Figure 5.1. Each sample has been scanned three times on different locations of the surface and the figure illustrates the total 60 spectra.

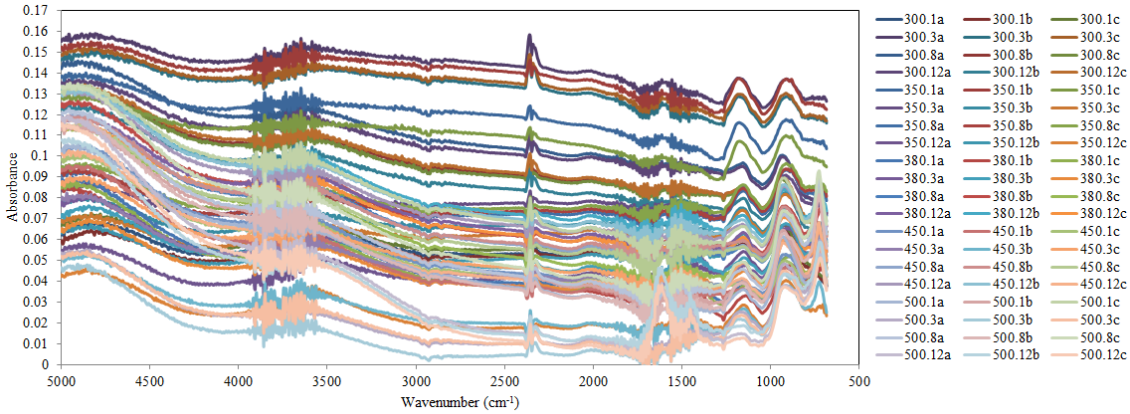

Figure 5.1. FTIR raw spectra of 20 samples (triplicate measurement) of 5754 series of aluminum alloy using Grazing Angle ATR.

As can be seen in Figure 5.1, there is a significant baseline shift not only between spectra of different samples but also even between triplicate measurements of the same samples. In addition, the spectral range between 1600-1200 cm^{-1} and 4000-3500 cm^{-1} show significant spectral noise. Therefore, the spectra needed a noise removal and baseline correction process for any further analysis. In Figure 5.2, the wavenumber range of spectra was narrowed down to 1080-680 cm^{-1} interval in order to observe aluminum oxide and magnesium oxide peaks existing in the approximate range of 930 cm^{-1} and 730 cm^{-1}, respectively.

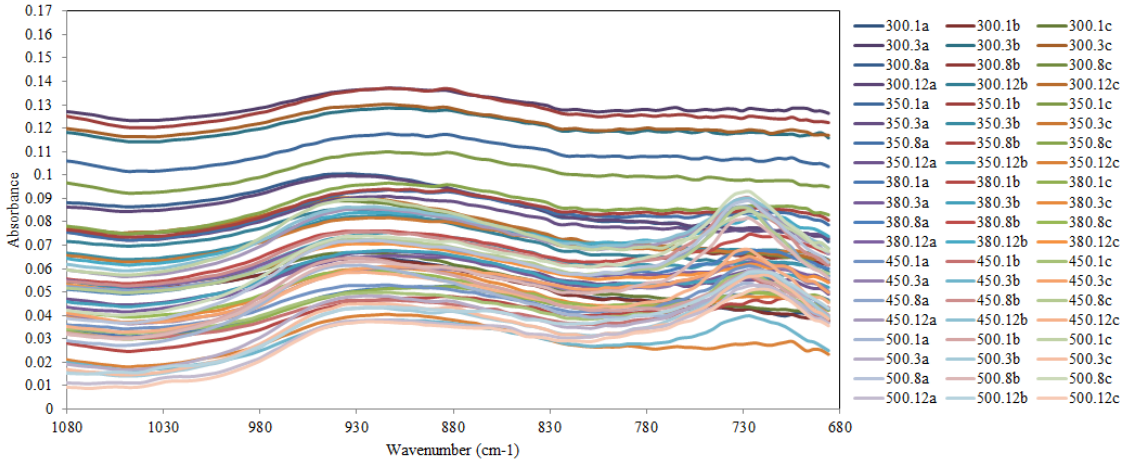

Figure 5.2. FTIR raw spectra of 20 samples of 5754 series of aluminum alloy using Grazing Angle ATR (narrowed range of wavenumber).

Even though the baseline shift on the spectra makes it difficult to compare spectra, it is still possible to observe the increase MgO peak at around 733 cm^{-1} as a results of increasing annealing temperature. By using the raw spectra given in Figure 5.1, simple least squares method was applied to be able to determine possible correlation between the magnitude of Al_2O_3 peak at around 933 cm^{-1} and MgO peak at around 733 cm^{-1} and annealing time and temperature. Figure 5.3 shows applied annealing time and temperature vs absorbance values of Al_2O_3 peak at 933 cm^{-1}. The correlation plots between absorbance values of MgO peak at 733 cm^{-1} vs annealing time and temperature were illustrated in Figure 5.4.

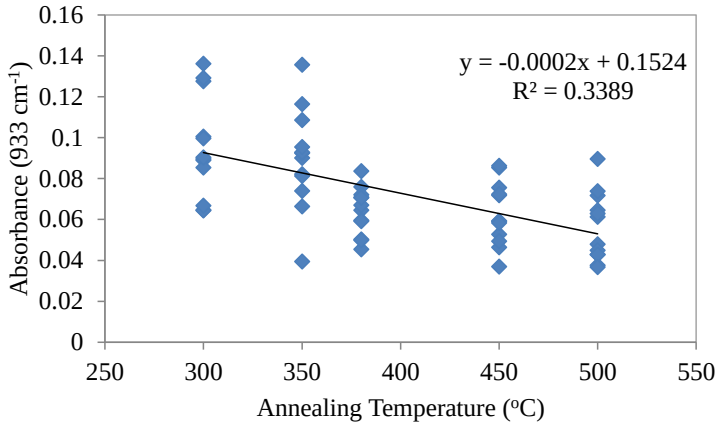

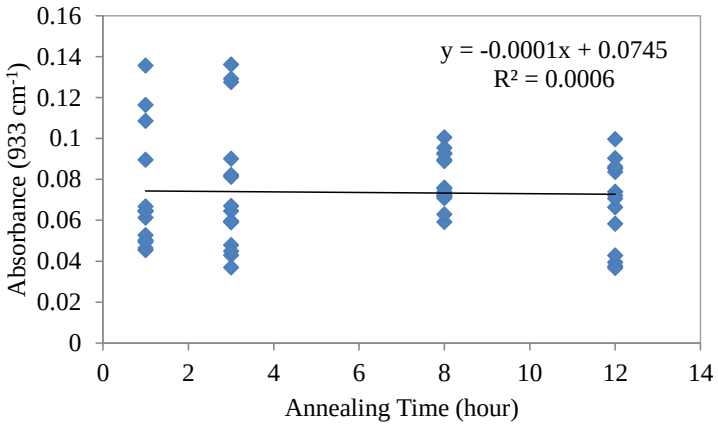

Figure 5.3. Plots of annealing temperature and time vs absorbance values at 933 cm^{-1}.

As shown in Figure 5.3, scatter plots between maximum absorbance at 933 cm^{-1} and two parameters (annealing time and temperature) do not indicate any meaningful correlation among two annealing parameters.

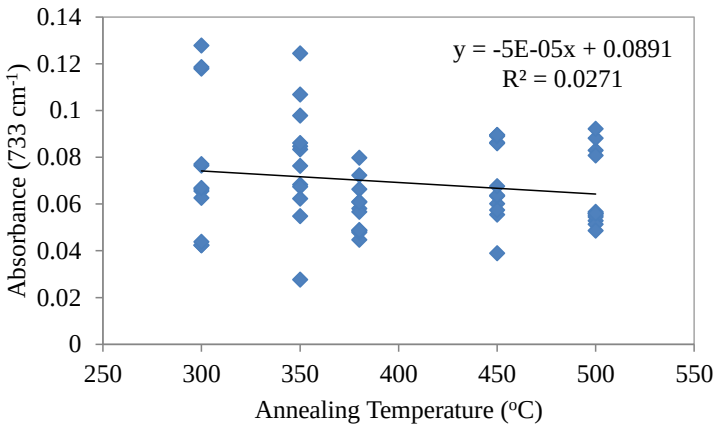

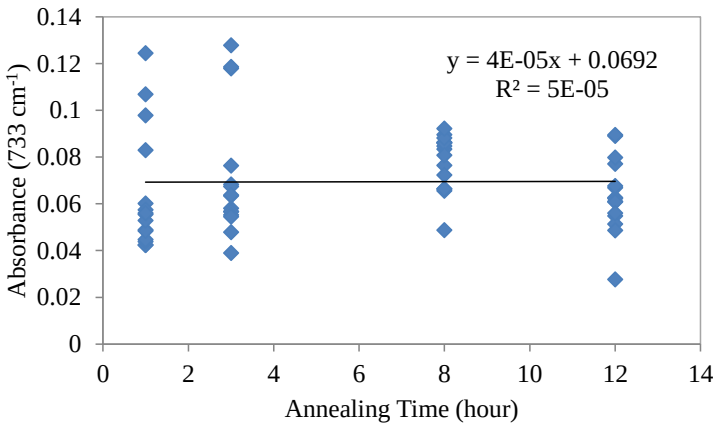

Figure 5.4. Plots of annealing temperature and time vs absorbance values at 733 cm^{-1}.

As in Figure 5.4, it is also clear that there is no significant correlation between the absorbance values at 733 cm^{-1} vs annealing temperature and time by using simple least square method. However, one can see that there is a clear change on the absorbance patterns of the spectra for the samples that are annealed at different time and temperatures. The problem is that, the spectra have a significant baseline variations and noisy. It becomes impossible to establish any calibration line based on these raw data. For this reason, raw spectral data has been subjected to noise removal and baseline correction process with a baseline correction algorithm developed in our laboratory. The details of the baseline correction algorithm are given in section 5.4. Resulting baseline line corrected and noise removed spectra are given in the Figure 5.5.

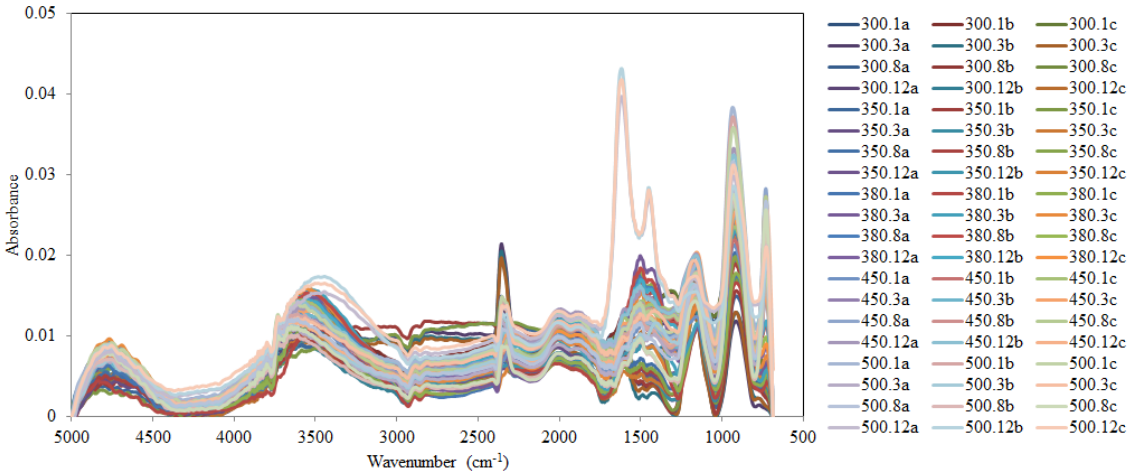

Figure 5.5. Baseline corrected and noise removed FTIR spectra of 20 samples of 5754 series of aluminum alloy (in triplicate) using Grazing Angle ATR.

As seen in the Figure 5.5 given above, after noise removal and baseline correction process, changes in absorbance patterns of the spectra has become clearer. In Figure 5.6, the same corrected spectra are given in narrow wavenumber range in order to interpret changes in aluminum oxide and magnesium oxide peaks at around 933 cm^{-1} and 733 cm^{-1}, respectively.

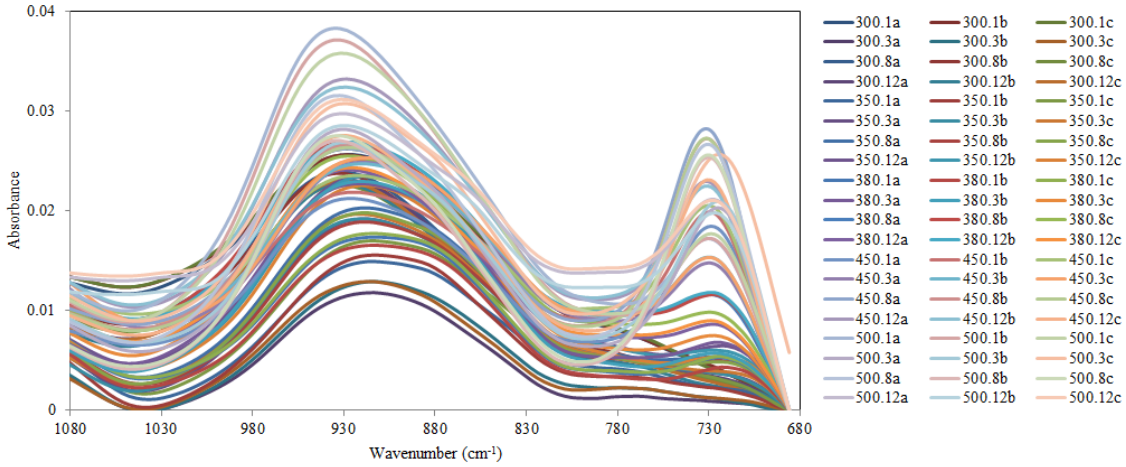

Figure 5.6. Narrowed range of wavenumbers from 1080 to 680 cm^{-1} for the baseline corrected and noise removed FTIR spectra of 20 samples of 5754 series of aluminum alloy (in triplicate) using Grazing Angle ATR.

When the absorbance peaks of Al_2O_3 and MgO given in Figure 5.6 were examined, it is clear that as the annealing temperature increases, there is a clear increase in the absorbance peaks at around 933 cm^{-1} and 733 cm^{-1}. In addition, there is also a slight shift on the wavenumber scale to the higher wavenumbers as the annealing time and temperature increases.

Using noise removed and baseline corrected FTIR spectra of 20 samples, the same simple least square method were applied to determine possible correlation between annealing temperature and time vs absorbance values at 933 cm^{-1} and 733 cm^{-1}, respectively. Figure 5.7 shows correlation plots for the absorbance peaks at 933 cm^{-1} and Figure 5.8 shows correlation plots for the absorbance peaks at 733 cm^{-1} for both annealing temperature and time.

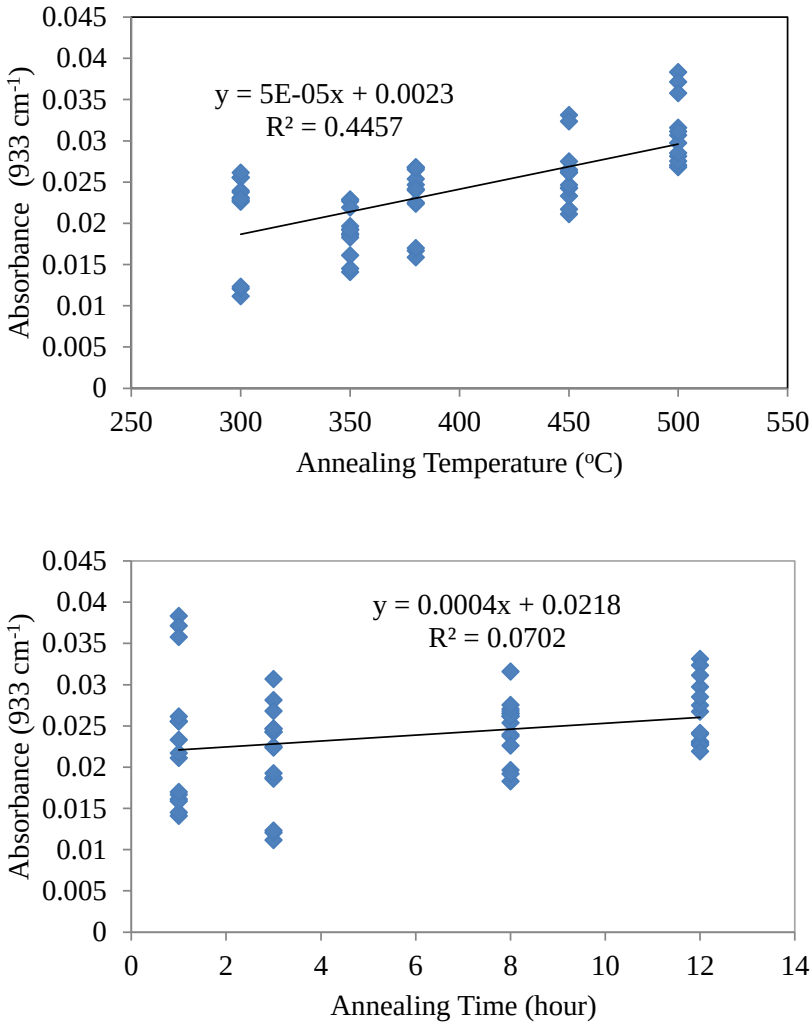

Figure 5.7. Correlation plots corresponding to maximum absorbance at 933 cm^{-1} from noise removed and baseline corrected spectra versus annealing temperature and time.

Although the plots which are given in Figure 5.7 shows better correlations compare to Figure 5.3 where the raw spectra was used, it is seen that there is a still significant variations for the same annealing temperature but different annealing times as it is expected. This is also true for the reverse case where annealing time is constant and annealing temperature is varied. On the other hand, there is a much more improvement on the regression coefficient between absorbance values at 933 cm^{-1} and especially annealing temperature.

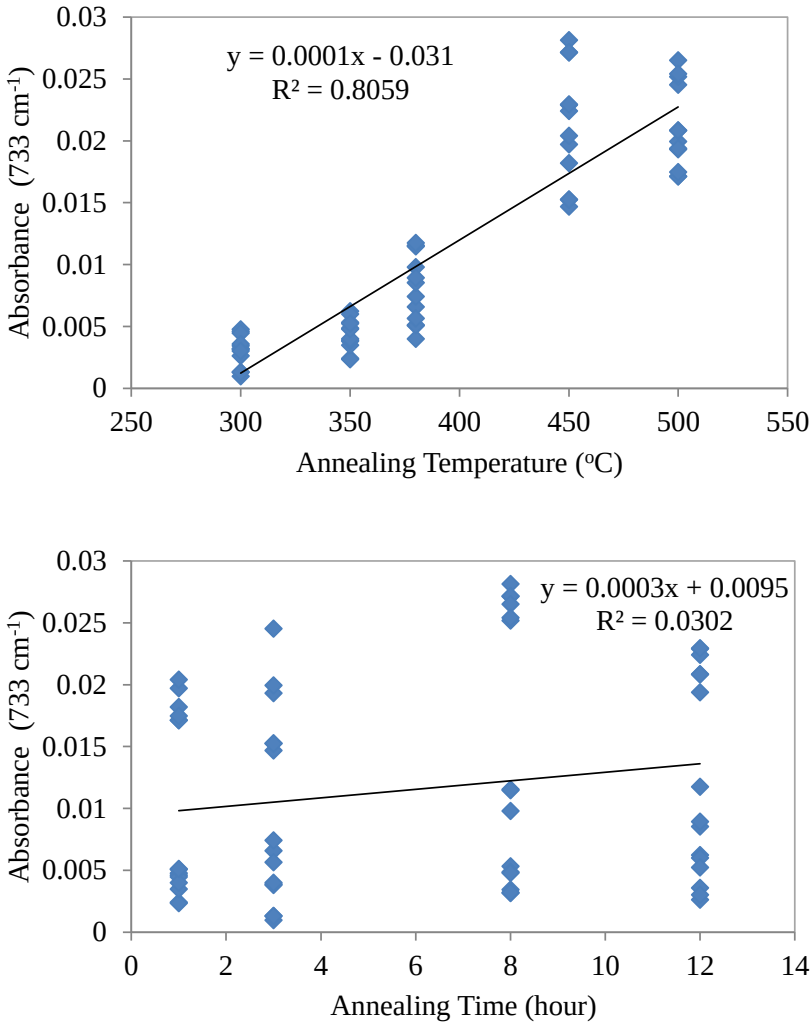

Figure 5.8. Correlation plots corresponding to maximum absorbance at 733 cm^{-1} from noise removed and baseline corrected spectra versus annealing temperature and time.

As shown in Figure 5.8, correlation coefficient between absorbance value at 733 cm^{-1} and annealing temperature was observed to be higher than the correlation plots given in Figure 5.7. Also, correlation between absorbance values at 733 cm^{-1} and annealing time was much lower compared to the annealing temperature. The fact that both annealing time and annealing temperature are changed simultaneously for these 20 samples, it would be more appropriate to demonstrate the change in absorbance value at both Al_2O_3 and MgO peaks vs time and temperature in a three dimensional surface plot. Figure 5.9 and 5.10 show these three dimensional surface plots of annealing time and temperature vs absorbance at 933 cm^{-1} and 733 cm^{-1}, respectively.

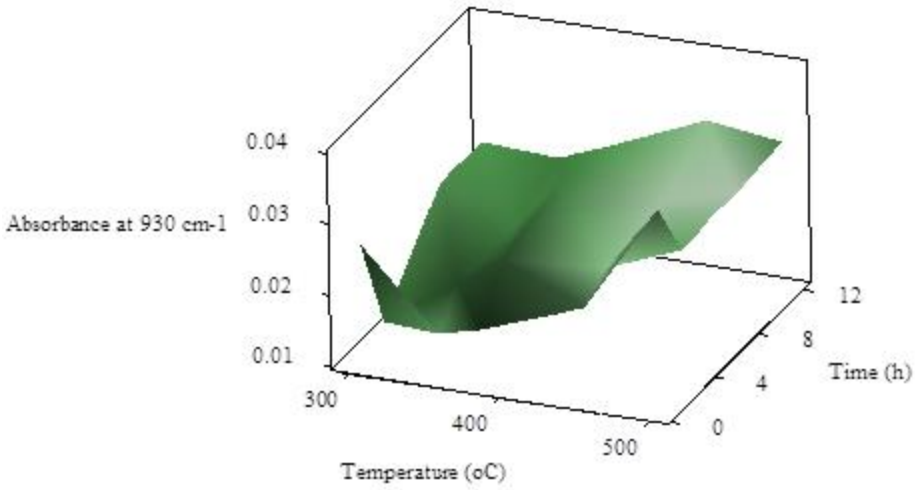

Figure 5.9. Three dimensional surface plot of absorbance at 933 cm^{-1} vs annealing temperature and time.

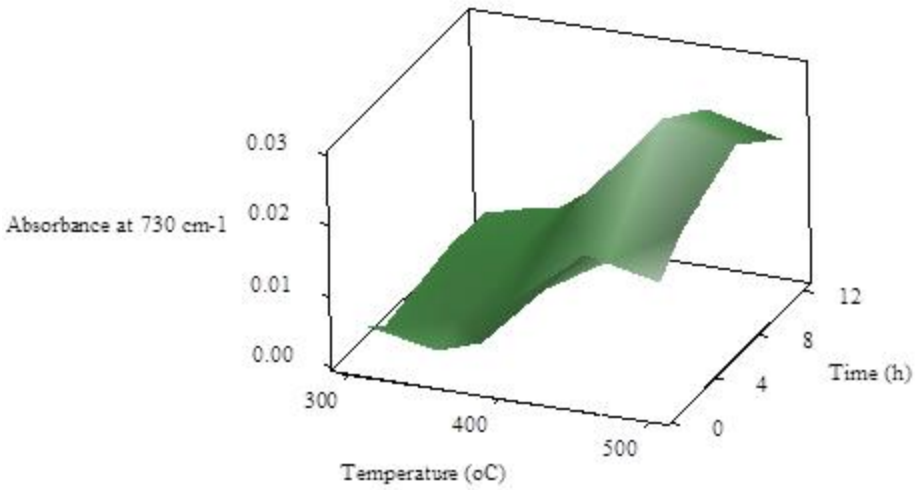

Figure 5.10. Three dimensional surface plot of absorbance at 733 cm^{-1} vs annealing temperature and time.

As can be seen from Figure 5.9 and 5.10, three dimensional surface plots of absorbance values (at 933 cm^{-1} and 733 cm^{-1}) vs annealing temperature and time, show clear view of increase in absorbance values as a function of annealing temperature and time. However, the main contribution to the increase of absorbance values is due to the change in temperature rather than time.

Because simple univariate calibration is unable to perform successful calibration models, it was decided to use a multivariate calibration approach in order to obtain better correlation coefficients. In this regard, it was decided to perform calibration graphs of the annealing temperature and annealing time using a genetic algorithm based inverse least squares (GILS) method. These modelling studies were initially carried out using raw spectral data of 20 samples of 5754 series aluminum alloy in triplicate (totally 60 sample). From these spectra, a total of 45 samples were chosen randomly as a calibration set and the remaining 15 samples were chosen as independent validation set for the model. Figure 5.11 shows actual vs predicted values of annealing temperature and annealing time obtained from multivariate calibration models.

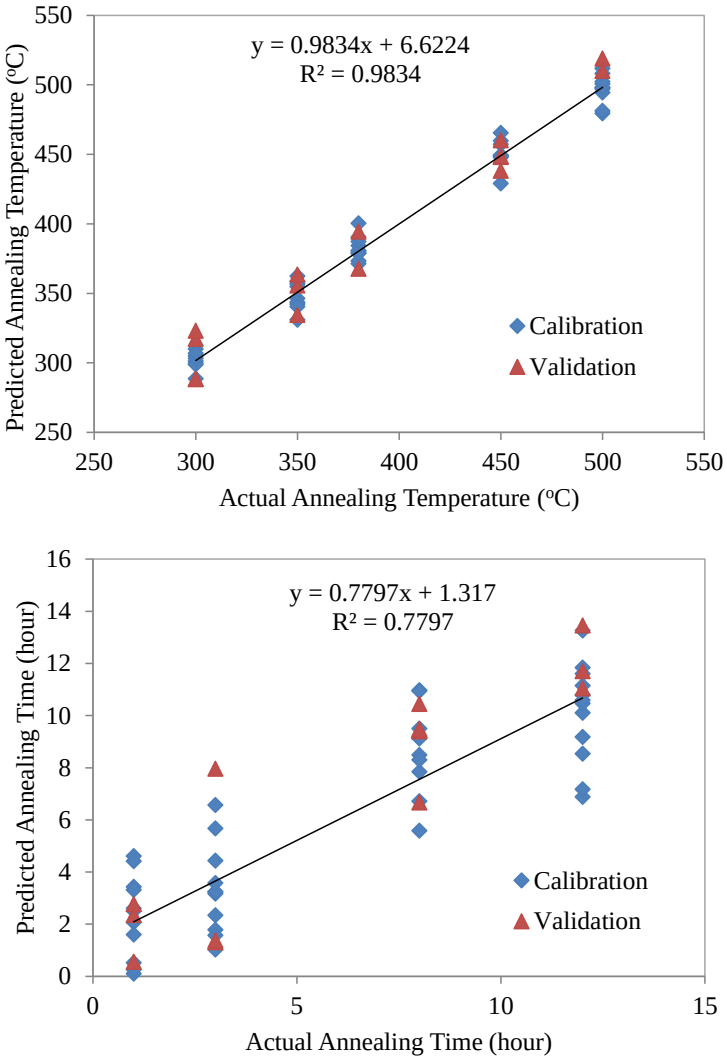

Figure 5.11. Actual vs predicted plots of annealing temperature and annealing time obtained from raw FTIR spectra using GILS method.

When actual vs predicted plots of annealing temperature and time were examined, it is seen that the correlation coefficient were significantly increase not only for temperature but also time. Likewise, when compared with the results of simple univariate calibration approach, results of both models for annealing time and temperature appears to be much better for both calibration and validation samples. From this point, the same multivariate calibration models were generated with noise removed and baseline corrected FTIR spectra and the actual vs predicted plots of temperature and time are given in Figure 5.12.

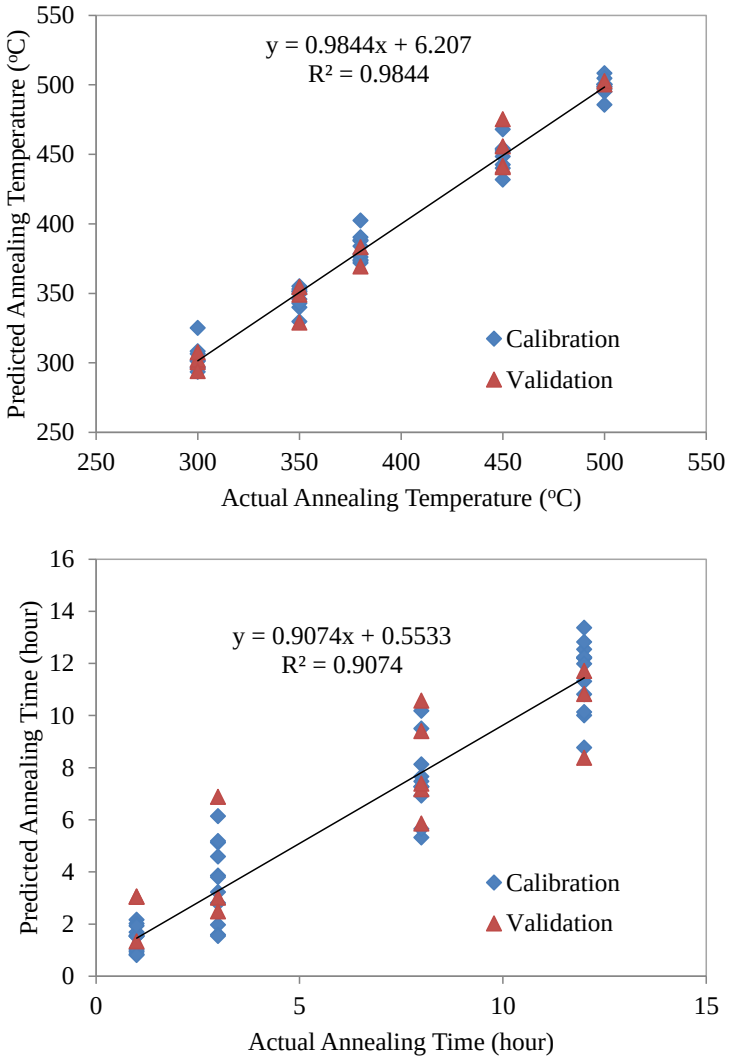

Figure 5.12. Actual vs predicted plots of annealing temperature and annealing time obtained from noise removed and baseline corrected FTIR spectra using GILS method.

As can be seen from Figure 5.12, multivariate calibration models generated with noise removed and baseline corrected spectra produced more successful results compared to modelling carried out with raw spectra.

At this point, the main issue needed to be emphasized is the purpose of this study to be able to develop a multivariate calibration model to determine the thickness of oxide layers based on FTIR spectroscopy. However, at the initial stage of the study, there were no reference oxide thickness information but it was still sufficient to motivate this thesis study. Therefore, it was decided to analyzed synthetically annealed aluminum samples with XPS and generate multivariate calibration models with the FTIR spectra and reference XPS results. The following section describes the oxide thickness studies which

were outline in the experimental section with two different aluminum alloy namely 3005 which has added magnesium and 3003BZ alloy which contains no externally added magnesium.

5.2. XPS Results

Figure 5.13 shows raw binding energy spectrum of one of the 3005 series of aluminum alloy sample obtained from XPS analysis after exposed to 1 hour duration of annealing time at 500 ^{o}C. Three dimensional Al 2p and Mg 2p XPS spectrum of the same sample given in Figure 5.13 were shown on Figure 5.14 as a function of raw counts vs binding energy and a number of iteration.

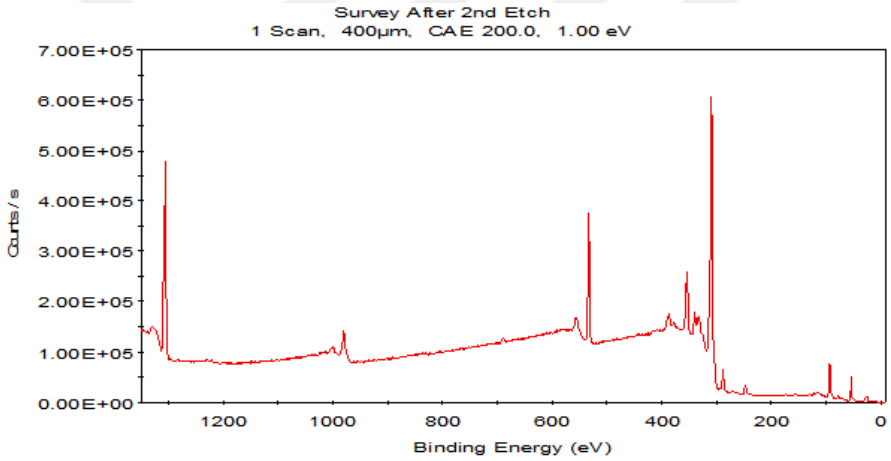

Figure 5.13. Raw XPS binding energy spectrum of one of the 3005 series of alloy sample exposed to 1 hour of annealing process at 500 ^{o}C.

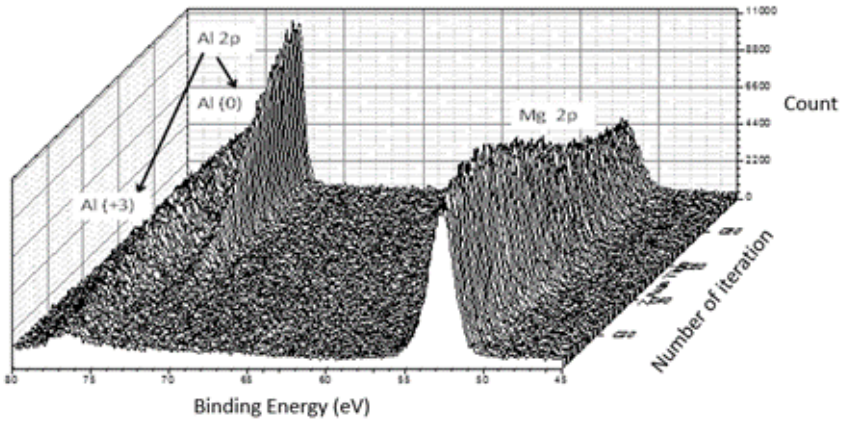

Figure 5.14. Changes of Al 2p and Mg 2p peaks as a result of iterative surface etching in a narrow energy band for the sample that was annealed for 1 hour at 500 ^{o}C from 3005 series alloy.

As seen in Figure 5.14, the binding energy of Al^{3+} corresponds to 75 eV where the binding energy of elemental Al corresponds to 70 eV. It is evident that the binding energy peak corresponding to elemental aluminum around 70 eV is starting to rise up after 60th iteration and rapidly grows up. On the other hand, with the increasing number of etching on the surface, the intensity of electrons having binding energy corresponding to Al_2O_3 starts to decrease. By using the point where elemental Al peak becomes visible, the thickness of Al_2O_3 on the surface can be calculated with the equations 2.1 - 2.5 given in Chapter 2. Two dimensional colored image of the XPS spectra given in Figure 5.14 were illustrated in Figure 5.15 for Al 2p scans and in Figure 5.16 for Mg 2p scans.

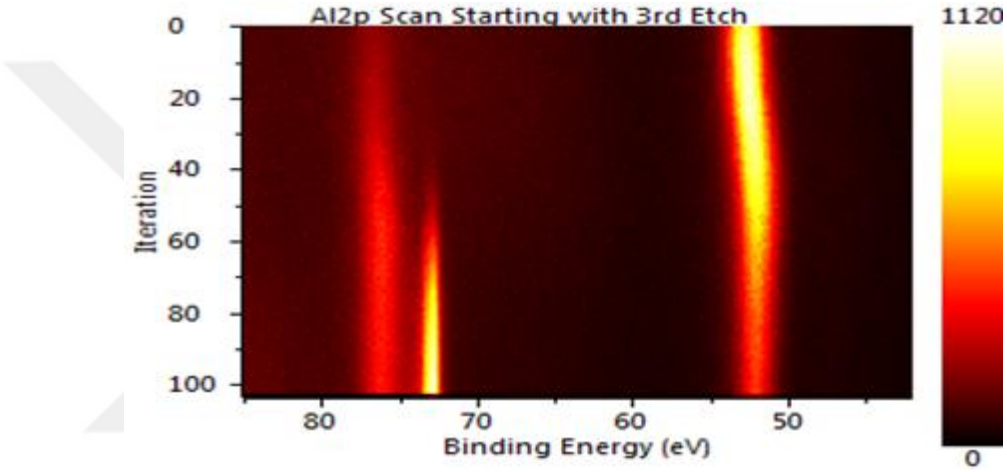

Figure 5.15. Two dimensional color representation aluminum 2p peaks as a result of iterative surface etching in a narrow energy band for the 3005 series sample that was annealed for 1 hour at 500 ^oC.

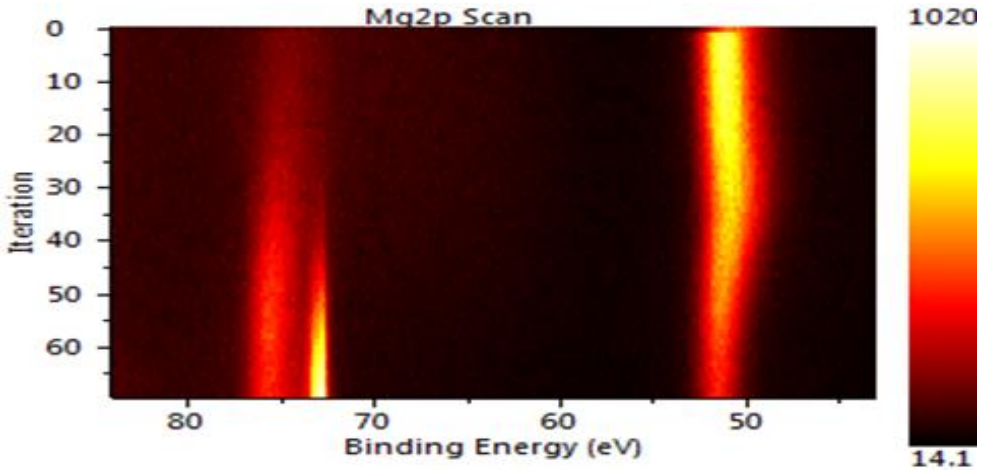

Figure 5.16. Two dimensional color representation magnesium 2p peaks as a result of iterative surface etching in a narrow energy band for the sample that was annealed for 1 hour at 500 ^oC from 3005 series alloy.

The two dimensional color images of Al 2p and Mg 2p scans show that as the iteration number increases the intensity of oxide peaks decrease while the intensity of natural elemental form of aluminum peak starts to rise up. Figure 5.17 illustrates the change of oxide thickness (in nm) as a function of iteration in the XPS analysis of the sample which was annealed one hour at 500 ^{o}C from 3005 alloy.

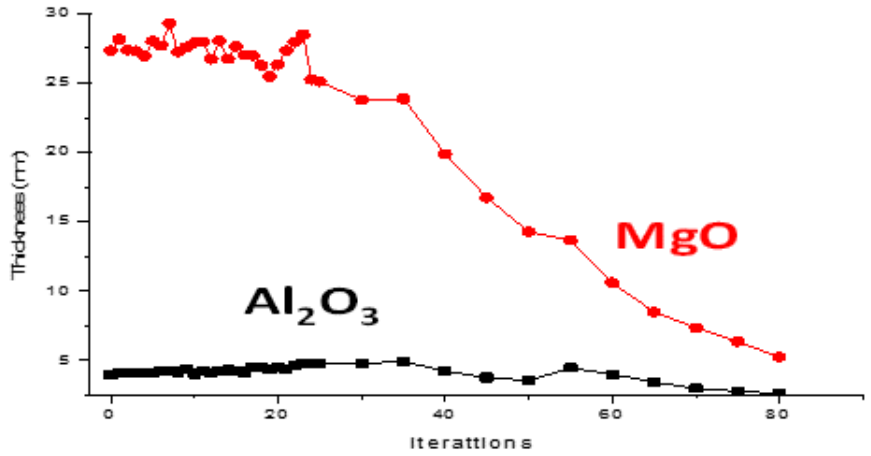

Figure 5.17. The plot of Al_2O_3 and MgO thicknesses vs the number of iterations for the sample which was annealed one hour at 500 ^{o}C from 3005 alloy.

Figure 5.17 shows that both MgO and Al_2O_3 thicknesses decrease as the etching takes place over and over after several iteration period. It is also evident that the MgO thickness is greater than the Al_2O_3 thickness on the very outer surface for this particular annealing temperature (500^{o}C).

Another aluminum alloy series namely 3003BZ were also studied with 21 sample of which 20 of them were synthetically annealed whereas one of them were kept as unannealed raw sample with the natural oxide layer on it. As in the case of 3005 series alloy, all of these samples were also analyzed with XPS for the reference oxide measurements. Among these samples, the one that was annealed at 500 ^{o}C for 1 hour was used for the demonstration of the XPS results in the following section. Figure 5.18 shows three dimensional Al 2p XPS spectrum of this series as a function of raw counts vs binding energy and a number of iteration.

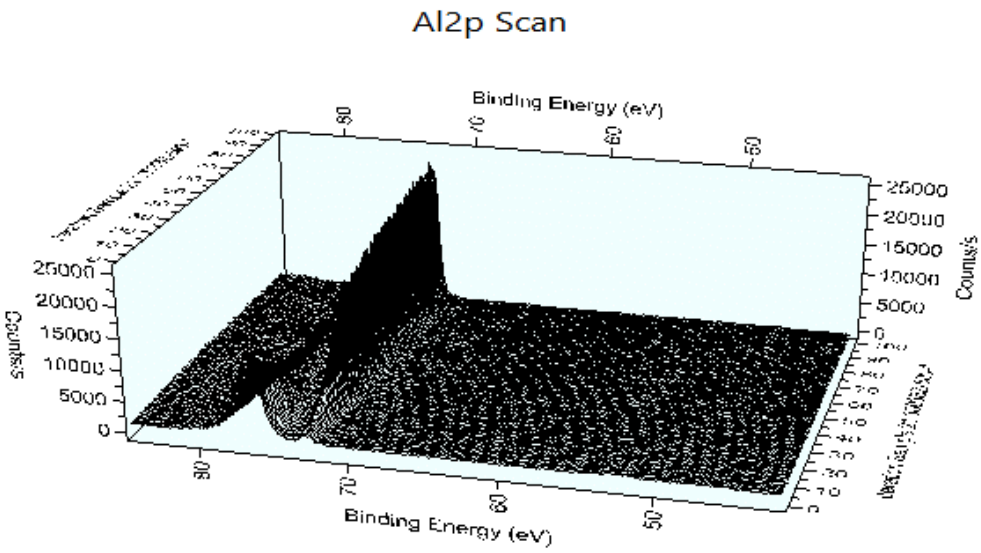

Figure 5.18. Changes of Al 2p peak as a result of iterative surface etching in a narrow energy band for the 3003BZ series sample that was annealed for 1 hour at 500 ^{o}C.

As shown in Figure 5.18, with the increase in the number of iterations on the surface, the intensity of elemental aluminum peak increases while the intensity of Al^{3+} decreases, as expected. On other hand, the absence of magnesium peak is a clear evidence since the sample contains no externally added magnesium for this alloy. In addition to three dimensional binding energy XPS spectra, which is given in Figure 5.18, the colored images of the same spectra were illustrated in Figure 5.19 for Al 2p. Also, the plot of Al_2O_3 and MgO thicknesses vs the number of iterations is given in Figure 5.20.

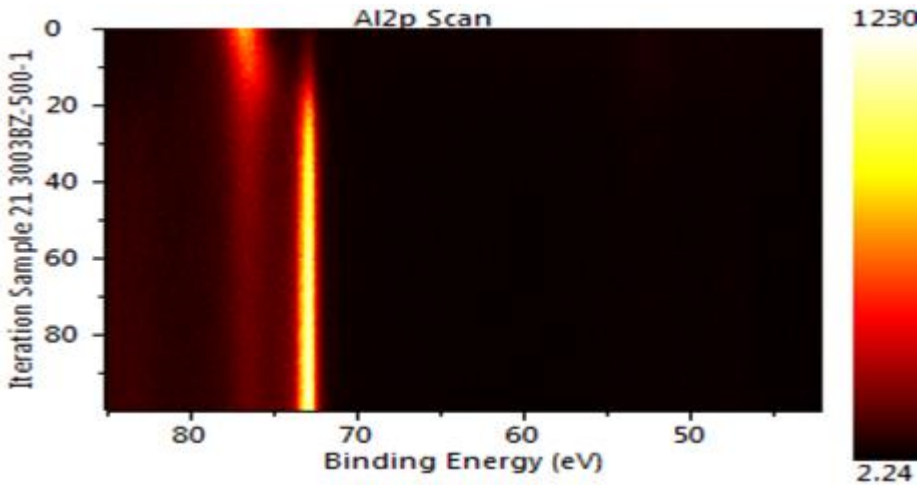

Figure 5.19. Two dimensional color representation of changes of Al 2p peak as a result of iterative surface etching in a narrow energy band for 3003BZ series alloy.

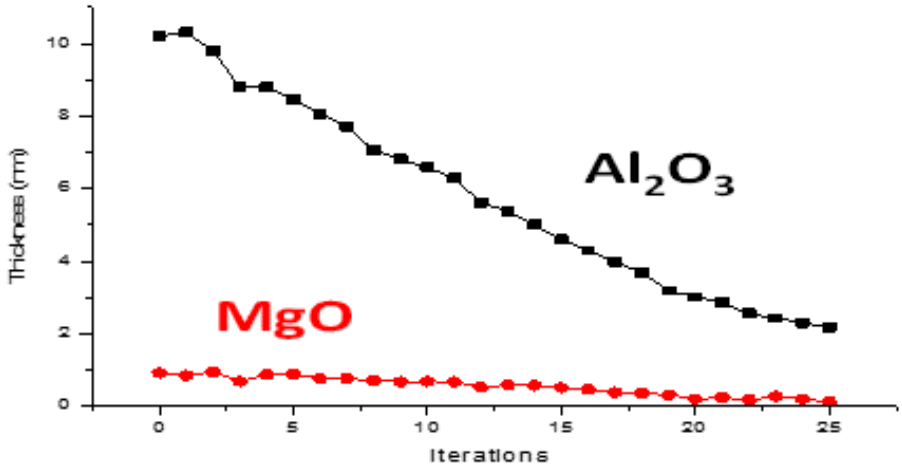

Figure 5.20. The plot of Al_2O_3 and MgO thicknesses vs the number of iterations for the sample which was annealed one hour at 500 ^oC from 3003BZ alloy.

As in case of 3005 series, Figure 5.20 also demonstrates that both Al_2O_3 and MgO thicknesses decrease as the etching procedure. It is also seen that, unlike 3005 series alloys, Al_2O_3 thickness is now much greater than MgO thickness for 3003BZ series of aluminum alloys since there is no added magnesium in this alloy.

As shown XPS spectral data of one of the 3005 alloy sample and one of the 3003BZ alloy sample as an example above, Al_2O_3 and MgO thicknesses of a total of 40 annealed samples (20 samples for each series) were calculated. In Table 5.1, the thickness of Al_2O_3 (in nanometer) formed as a result of annealing operation at four different time periods and five different temperature on 3005 series of aluminum surface are given. The thickness of MgO of the same samples are given in Table 5.2.

Table 5.1. Al_2O_3 thickness of 20 samples (in nanometer) belongs to 3005 series of aluminum alloys determined by XPS method after exposed to different annealing temperature and time.

Thickness of Al_2O_3 (nm)	Annealing Time, h			
Annealing Temperature, ^oC	1 hour	3 hours	5 hours	8 hours
300	4.4	4.8	5.1	5.4
350	4.8	5.1	5.3	5.6
400	8.0	12.0	16.0	18.0
450	14.0	17.0	20.0	22.0
500	15.0	>15	>15	>15

Table 5.2. MgO thickness of 20 samples (in nanometer) belongs to 3005 series of aluminum alloys determined by XPS method after exposed to different annealing temperature and time.

Thickness of MgO (nm)	Annealing Time, h			
Annealing Temperature, ^{o}C	1 hour	3 hours	5 hours	8 hours
300	1.4	2.4	2.7	3.0
350	2.0	5.0	7.0	10.0
400	16.0	20.0	25.0	30.0
450	20.0	24.0	28.0	36.0
500	25	>15	>15	>15

As seen in Table 5.1 and Table 5.2, Al_2O_3 oxide thickness of three 3005 series of aluminum alloys, shown as ">15 nm", could not be determined because of extremely long analysis time. Yet, another notable result in Table 5.1 and 5.2 is that, up to 350 ^{o}C annealing temperature, the thickness of Al_2O_3 formed on the surface is more than the thickness of the MgO. However, for the samples exposed to annealing procedure at 400 and 450 ^{o}C, rapid increase in the amount of MgO thickness is observed. This results support the proposed formation of MgO and Al_2MgO_4 spinels which were mentioned in the Chapter 1. However, for the completeness and understanding of the spinel formation mechanism, the process is also briefly explained here. Figure 5.21 represents the MgO and Al_2MgO_4 spinel formation mechanism due to temperature increase in the annealing process.

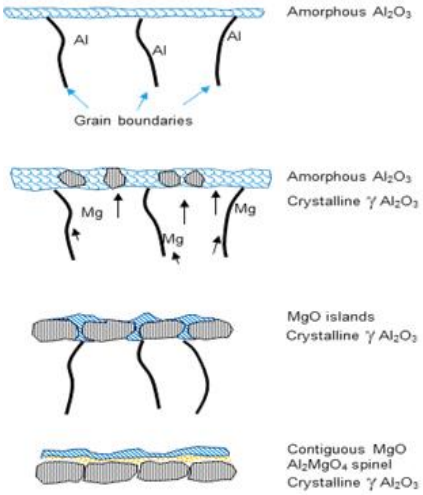

Figure 5.21. Schematic representations of MgO and Al_2MgO_4 spinels formation which depends on the increasing annealing temperature.

The evidence of spinels formation as a result of temperature dependent oxidation on the surfaces was also observed in the FTIR study which will be given in the next section in detail. As explained early on, XPS reference analysis for 3003BZ series of alloys were also performed and Al_2O_3 and MgO thicknesses were calculated. Table 5.3 shows Al_2O_3 thicknesses while Table 5.4 shows MgO thicknesses of 20 annealed samples.

Table 5.3. Al_2O_3 thicknesses of 20 samples belong to 3003BZ series of aluminum alloys determined by XPS method after exposed to different annealing temperatures and times.

Thickness of Al_2O_3 (nm)	Annealing Time, h			
Annealing Temperature, ^oC	1 hour	3 hours	5 hours	8 hours
300	4.9	5.1	5.3	5.5
350	5.5	5.8	6.2	6.6
400	6.6	7.1	7.4	8.0
450	8.0	9.0	10.0	11.0
500	11.0	12.0	13.0	14.0

Table 5.4. MgO thicknesses of 20 samples belong to 3003BZ series of aluminum alloys determined by XPS method after exposed to digfferent annealing temperatures and times.

Thickness of MgO (nm)	Annealing Time, h			
Annealing Temperature, ^oC	1 hour	3 hours	5 hours	8 hours
300	0.1	0.2	0.3	0.4
350	0.1	0.1	0.2	0.2
400	0.4	0.3	0.4	0.5
450	0.4	0.5	0.4	0.4
500	0.8	0.8	0.8	0.8

When the thicknesses of Al_2O_3 and MgO on the surface of 3003BZ series alloy samples shown in Table 5.3 and Table 5.4 were compared to oxide thicknesses of 3005 series alloys, the amount of oxides present on the surface of 3003BZ series alloys are observed to be much lower, especially for the MgO.

In order to give a statistical meaning to the oxide thickness measurements at different annealing temperatures and times, it was decided to apply two-way analysis of variance (ANOVA) at 95% confidence level ($\alpha = 0.05$). Two-way ANOVA results of 3005 series alloys for Al_2O_3 and MgO are given in Table 5.5 and Table 5.6, respectively. Similarly, ANOVA results of 3003BZ series alloys for Al_2O_3 and MgO are given in Table 5.7 and Table 5.8, respectively.

Table 5.5. Two-factor (annealing temperature and annealing time) analysis of variance (ANOVA) results for Al_2O_3 of 3005 series alloys.

ANOVA						
Source of Variation	*SS*	*df*	*MS*	*F*	*P-value*	*F crit*
Annealing Temperature	512.917	3	170.972	38.4682	1.8E-05	3.86255
Annealing Time	56.6369	3	18.879	4.2477	0.03969	3.86255
Error	40.0006	9	4.44451			
Total	609.554	15				

Table 5.6. Two-factor (annealing temperature and annealing time) analysis of variance (ANOVA) results for MgO of 3005 series alloys.

ANOVA						
Source of Variation	*SS*	*df*	*MS*	*F*	*P-value*	*F crit*
Annealing Temperature	1774.3	3	591.432	72.8558	1.2E-06	3.86255
Annealing Time	213.137	3	71.0456	8.75178	0.00494	3.86255
Error	73.0606	9	8.11785			
Total	2060.494	15				

Table 5.7. Two-factor (annealing temperature and time) analysis of variance (ANOVA) results for Al_2O_3 of 3003BZ series alloys.

ANOVA						
Source of Variation	*SS*	*df*	*MS*	*F*	*P-value*	*F crit*
Annealing Temperature	138.865	4	34.7163	149.264	4.02578E-10	3.25917
Annealing Time	9.124	3	3.04133	13.0763	0.000433026	3.49029
Error	2.791	12	0.23258			
Total	150.78	19				

Table 5.8. Two-factor (annealing temperature and annealing time) analysis of variance (ANOVA) results for MgO of 3003BZ series.

ANOVA						
Source of Variation	*SS*	*df*	*MS*	*F*	*P-value*	*F crit*
Annealing Temperature	0.982	4	0.2455	50.7931	2E-07	3.25917
Annealing Time	0.0295	3	0.00983	2.03448	0.16279	3.49029
Error	0.058	12	0.00483			
Total	1.0695	19				

As it can be seen from the ANOVA tables above, at 95% confidence level, while all of the p-values are below the limit value ($\alpha = 0.05$), only the p-value of MgO for annealing time in Table 5.8 was found to be greater than 0.05 (α=0.05). This means that only for the analysis performed with MgO for 3003BZ series of aluminum, annealing time does not make a significant contribution. This is a reasonable outcome since 3003BZ alloy do not contain added magnesium. However, in all other cases, both annealing temperature and annealing time contribute significantly to the oxide thickness on the surface. The other important thing is that, as it is understood from the degrees of freedom, two-way ANOVA for 3005 series alloys were performed with 16 samples while two-way ANOVA for 3003BZ series alloys were performed with 20 samples. As it was mentioned in Table 5.1 and Table 5.2, the oxide thicknesses of three aluminum samples could not be determined by XPS because of extremely long analysis time. That is why, while performing two-way ANOVA studies, samples belongs to 500 ^{o}C annealing temperature did not used. However, because the oxide thicknesses of all of the samples belongs to 3003BZ series were known, 20 samples were used to perform two-way ANOVA analysis.

In addition to two-way ANOVA results shown in the Table 5.5-5.8 above, regression analysis was performed with a full quadratic model including linear and non-linear effects of both factors (annealing temperature and annealing time), non-linear terms (squared temperature and time) and their interaction along with intercept term (equation 5.1).

$$y = b_0 + b_1 x_1 + b_2 x_2 + b_{11} x_1^2 + b_{22} x_2^2 + b_{12} x_1 x_2 \quad (5.1)$$

where b_0 represents intercept term, b_1 and b_2 indicate linear contributions, b_{11} and b_{22} stand for quadratic effects and b_{12} expresses the interaction of both factors.

For 3005 series alloys, the detailed ANOVA results of regression analysis are shown in Table 5.9 and Table 5.10 for Al_2O_3 and MgO, respectively. Similarly, detailed ANOVA results of regression analysis results for 3003BZ series alloys are shown in Table 5.11 and 5.12 for Al_2O_3 and MgO, respectively.

Table 5.9. Analysis of variance (ANOVA) results for Al_2O_3 of 3005 series.

ANOVA for Aluminum Oxide						
Source	**DF**	**Seq SS**	**Adj SS**	**Adj MS**	**F**	**P**
Regression	5	567.901	567.901	113.58	27.27	0
Linear	2	520.112	538.05	269.025	64.59	0
Temperature	1	466.095	482.83	482.83	115.92	0
Time	1	54.017	55.22	55.22	13.26	0.005
Square	2	22.453	22.453	11.227	2.7	0.116
Temperature*Temperature	1	20.026	20.026	20.026	4.81	0.053
Time*Time	1	2.428	2.428	2.428	0.58	0.463
Interaction	1	25.336	25.336	25.336	6.08	0.033
Temperature*Time	1	25.336	25.336	25.336	6.08	0.033
Residual Error	10	41.653	41.653	4.165		
Total	15	609.554				

Table 5.10. Analysis of variance (ANOVA) results for MgO of 3005 series.

ANOVA for Magnesium Oxide						
Source	**DF**	**Seq SS**	**Adj SS**	**Adj MS**	**F**	**P**
Regression	5	1923.63	1923.63	384.73	28.11	0
Linear	2	1855.6	1904.62	952.31	69.58	0
Temperature	1	1642.58	1691.79	1691.79	123.61	0
Time	1	213.02	212.82	212.82	15.55	0.003
Square	2	0.5	0.5	0.25	0.02	0.982
Temperature*Temperature	1	0.39	0.39	0.39	0.03	0.869
Time*Time	1	0.11	0.11	0.11	0.01	0.93
Interaction	1	67.53	67.53	67.53	4.93	0.051
Temperature*Time	1	67.53	67.53	67.53	4.93	0.051
Residual Error	10	136.86	136.86	13.69		
Total	15	2060.49				

Table 5.11. Analysis of variance (ANOVA) results for Al_2O_3 of 3003BZ series.

ANOVA for Aluminum Oxide						
Source	**DF**	**Seq SS**	**Adj SS**	**Adj MS**	**F**	**P**
Regression	5	150.359	150.359	30.072	999.94	0
Linear	2	139.737	142.041	71.02	2361.56	0
Temperature	1	130.682	132.926	132.926	4420.03	0
Time	1	9.055	9.115	9.115	303.09	0
Square	2	8.167	8.167	4.084	135.79	0
Temperature*Temperature	1	8.102	8.102	8.102	269.39	0
Time*Time	1	0.066	0.066	0.066	2.19	0.161
Interaction	1	2.455	2.455	2.455	81.62	0
Temperature*Time	1	2.455	2.455	2.455	81.62	0
Residual Error	14	0.421	0.421	0.03		
Total	19	150.78				

Table 5.12. Analysis of variance (ANOVA) results for MgO of 3003BZ series.

ANOVA for Magnesium Oxide						
Source	**DF**	**Seq SS**	**Adj SS**	**Adj MS**	**F**	**P**
Regression	5	0.96651	0.96651	0.1933	26.28	0
Linear	2	0.78541	0.74923	0.37462	50.92	0
Temperature	1	0.75625	0.72025	0.72025	97.9	0
Time	1	0.02916	0.02898	0.02898	3.94	0.067
Square	2	0.15019	0.15019	0.0751	10.21	0.002
Temperature*Temperature	1	0.15018	0.15018	0.15018	20.41	0
Time*Time	1	0.00001	1.4E-05	1.4E-05	0	0.966
Interaction	1	0.0309	0.0309	0.0309	4.2	0.06
Temperature*Time	1	0.0309	0.0309	0.0309	4.2	0.06
Residual Error	14	0.10299	0.103	0.00736		
Total	19	1.0695				

As can be seen from ANOVA Table 5.9 and 5.10 above, when *p*-values of annealing temperature compared to *p*-values of annealing time, while annealing temperature and time and their interaction have significant contributions to oxide thicknesses ($p<0.05$), square interactions especially the time have no significant importance. Similarly for 3003BZ series alloys, as shown in Table 5.11 and 5.12, annealing temperature has much more significant effect than annealing time. It can be concluded that the thickness of oxide formation on the surface is much more affected by exposure to higher annealing temperature than annealing time.

5.3. FTIR Results

After completing XPS reference analysis studies, multivariate modelling studies were conducted to determine the thickness of Al_2O_3 and MgO based on FTIR spectroscopy. Grazing Angle ATR-FTIR spectra of all the samples which are given in Table 5.1 and 5.2 for 3005 alloy and in Table 5.3 and 5.4 for 3003BZ alloy were collected by using a bench top FTIR spectrometer (Perkin Elmer Frontier) equipped with a Grazing Angle ATR (Pike Tech) accessory. In addition to the FTIR spectra of 20 samples mentioned above from each series, FTIR spectra of an additional un-annealed alloy sample from each series (3005 and 3003BZ) were also taken as a starting point. Grazing Angle ATR-FTIR spectra of both 3005 and 3003BZ alloys were collected in two different orientation. First, aluminum samples were placed perpendicular to the rolling direction over the top of the accessory. After perpendicular measurements were taken, samples were placed parallel to the rolling direction and Grazing Angle ATR-FTIR spectra were collected. Figure 5.22 shows the picture of perpendicular and parallel direction measurements.

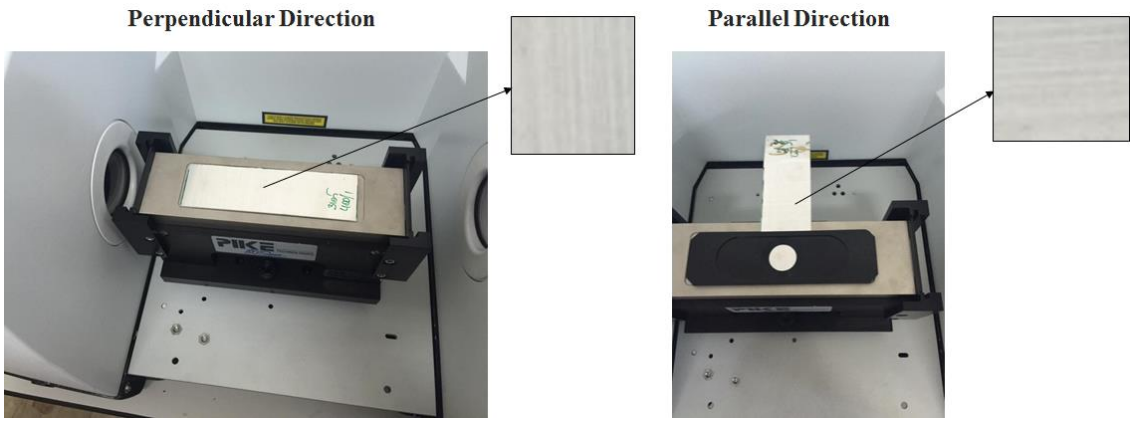

Figure 5.22. Perpendicular and parallel direction of Grazing Angle ATR-FTIR measurements.

5.3.1. Grazing Angle ATR-FTIR Results of Perpendicular Direction

As shown in Figure 5.22, samples were placed face down on the top of the grazing angle accessory in perpendicular direction and FTIR spectra of aluminum alloys were obtained. Figure 5.23 shows the raw GATR-FTIR spectra of 3005 series of 21 samples obtained in perpendicular direction whereas GATR-FTIR spectra of 3003BZ series of 21 samples are shown in Figure 5.24.

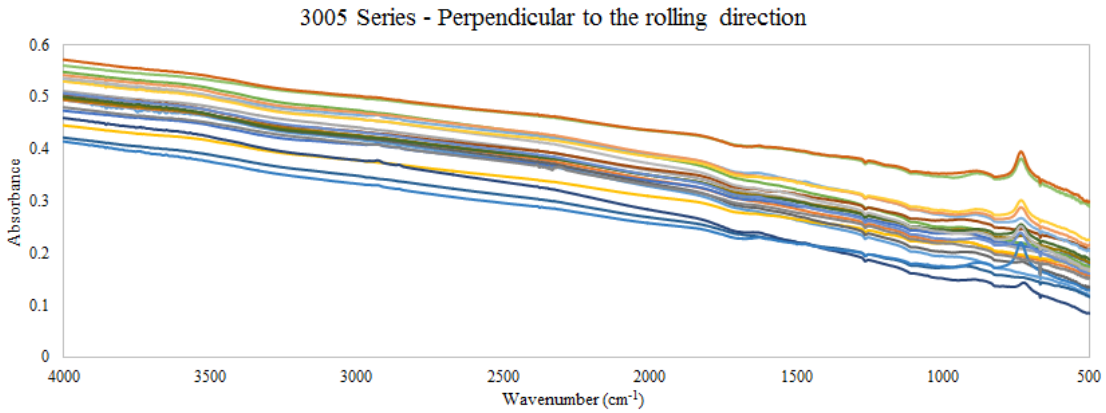

Figure 5.23. Raw FTIR spectra from Perkin Elmer FTIR Spectrometer coupled with Grazing Angle ATR of 21 samples of 3005 series alloys obtained in perpendicular to the rolling direction.

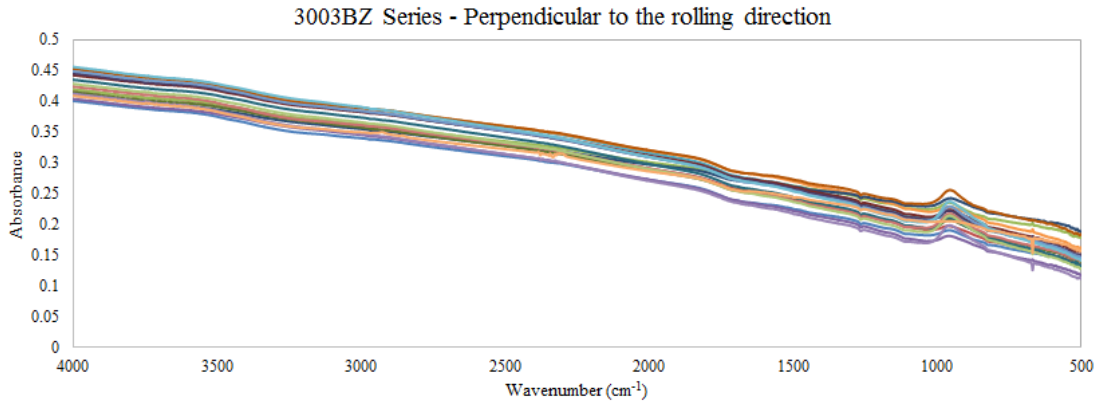

Figure 5.24. Raw FTIR spectra from Perkin Elmer FTIR Spectrometer coupled with Grazing Angle ATR of 21 samples of 3003BZ series alloys.

When the raw FTIR spectra of 3005 and 3003BZ series of aluminum given in Figure 5.23 and Figure 5.24 were examined closely, it is clear that a significant baseline shift was observed depending on the surface brightness and roughness. Therefore, for analysis and modelling with classical univariate (simple least square method) or chemometrics multivariate calibration methods, first thing to be done was to eliminate these baseline shifts. In today's technology, modern FTIR spectrometers are manufactured with various baseline correction software for this purpose and provide elimination of baseline shifts according to intensity and shape. However, these standard tools cannot always provide sufficient baseline correction for such a high fluctuations illustrated in Figures 5.23 and 5.24. In this context, it was necessary to develop specific baseline correction algorithms for such an unusual FTIR spectra. In this study, conventional baseline correction toolbox which is included in FTIR spectrometer software was used initially. However, the results of standard baseline correction methods did not provide sufficient correction. As a result, a new baseline correction algorithm has been developed which is explained in the following section.

5.3.2. Baseline Correction

The baseline shifts shown on the Figures 5.23 and 5.24 are partially linear in certain parts of the spectra and partially non-linear especially in lower wavenumber ranges. As a result, a second order quadratic baseline correction algorithm was developed. This method fits a quadratic function using the four consecutive wavenumbers chosen from the full spectral range shown as an example in Figure 5.25 for given points and this function is then used for constructing a baseline to be subtracted from the absorbances at each wavenumber for each experiment. A standard form of a quadratic function is given in the equation 5.2.

$$y = b_0 + b_1.x + b_2.x^2 \tag{5.2}$$

where x is the absorbance at a wavenumber, b_0, b_1 and b_2 are the coefficients and y is the corresponding value on the fitted line.

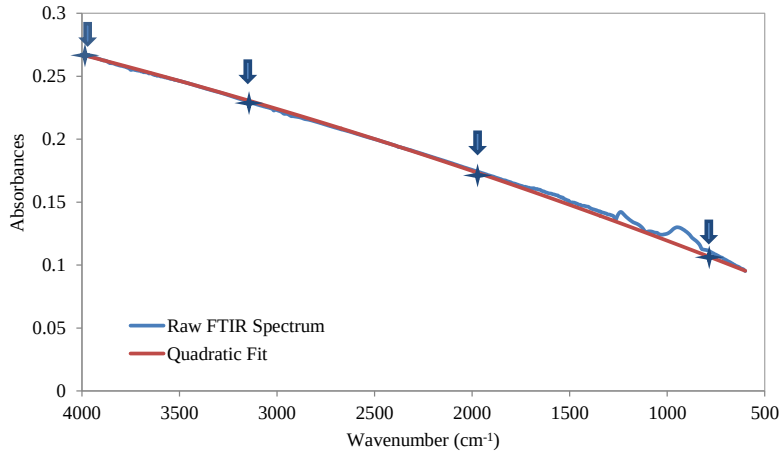

Figure 5.25. The plot of raw FTIR spectrum, the selected wavenumbers for the second order quadratic baseline equation and corresponding baseline spectra generated with a quadratic equation.

Using the least squares approach, the coefficients of the quadratic equation given above were determined based on the four selected wavenumber which are 4000, 3000, 2000 and 600 cm^{-1}. By using this fitted equation, a synthetic baseline was generated for each spectrum and then subtracted the corresponding raw spectrum of the particular sample. Figure 5.26 illustrates baseline corrected FTIR spectrum given in Figure 5.25 above.

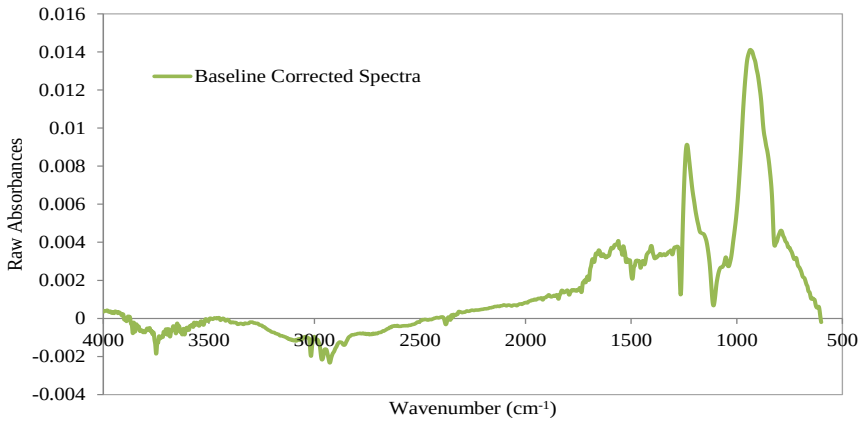

Figure 5.26. Baseline corrected form of the FTIR spectrum.

As seen in Figure 5.26, the peaks for aluminum oxide and magnesium oxide below the 1000 cm^{-1} wavenumber are now visible even though the overall absorbance scales are narrower when compared to the raw spectra. In addition, the spectral features above

2500 cm^{-1} go to negative absorbance value but this do not disturb multivariate calibration as there are no meaningful spectral features on this part of the spectral data.

Figure 5.27 shows baseline corrected FTIR spectra of 3005 series of aluminum measured in perpendicular direction using baseline correction method mentioned above. While Figure 5.27 includes whole range, Figure 5.28 shows narrowed wavenumber range to focus oxide peaks.

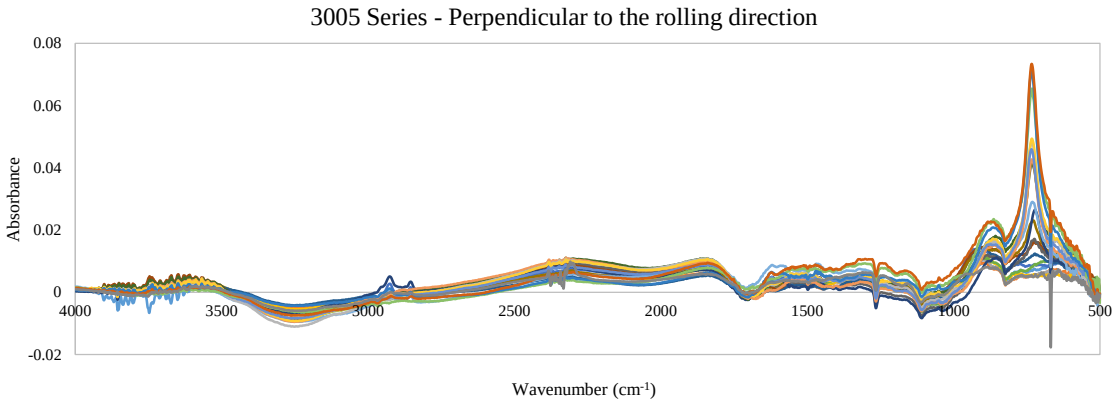

Figure 5.27. Baseline corrected FTIR spectra of 21 samples of 3005 series of aluminum in perpendicular direction using Perkin Elmer FTIR Spectrometer coupled with Grazing Angle ATR.

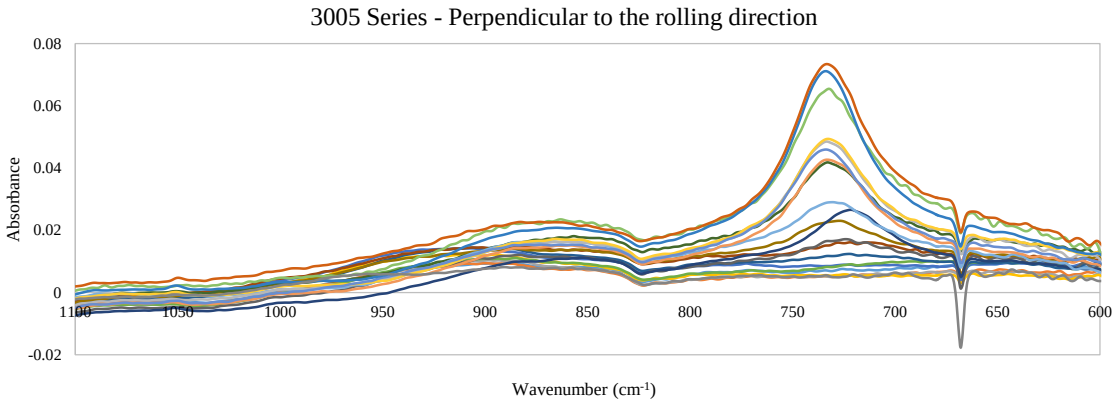

Figure 5.28. Narrowed range of wavenumbers from 1100 to 600 cm^{-1} for the baseline corrected FTIR spectra of 21 samples of 3005 series of aluminum alloy using Perkin Elmer FTIR Spectrometer coupled with Grazing Angle ATR.

As can be seen from FTIR spectra given in Figure 5.28, the peaks around 930 cm^{-1} and 730 cm^{-1} which correspond to Al_2O_3 and MgO, respectively were clearly observed after baseline correction. The figure demonstrates that the absorbance peak of

Al_2O_3 shifts to higher wavenumber as the annealing temperature and time increases. This shift of the wavenumber and the decrease in the height of absorbance peak of Al_2O_3 may be explained by the mechanism of MgO and Al_2MgO_4 spinel formation shown in the Figure 5.21. In addition to this, while the intensity of Al_2O_3 absorbance lowers down, the intensity of MgO absorbance significantly increases. Since the univariate calibration models use the absorbance at a single wavenumber, the shift of the characteristic peak makes the modelling unreliable.

When FTIR spectra of 3003BZ alloys are examined, it is evident that the same baseline shift problem exists as shown in Figure 5.24. Thus, the same baseline correction algorithm was applied to 3003BZ series of aluminum alloy samples and the resulting baseline corrected spectra are shown in Figure 5.29. In order to focus aluminum oxide peak, a narrowed wavenumber (1500-600 cm^{-1}) range of spectra is shown in Figure 5.30. Here the significant difference is the absence of MgO peak, which was dominating 3005 series aluminum alloy in Figure 5.30 since this alloy do not contain externally added magnesium in it.

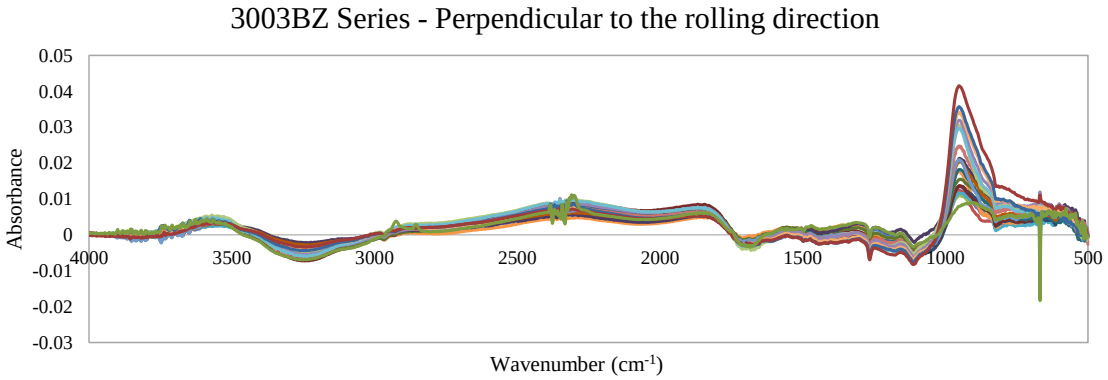

Figure 5.29. Baseline corrected FTIR spectra of 21 samples of 3003BZ series of aluminum alloy in perpendicular direction using Perkin Elmer FTIR Spectrometer coupled with Grazing Angle ATR.

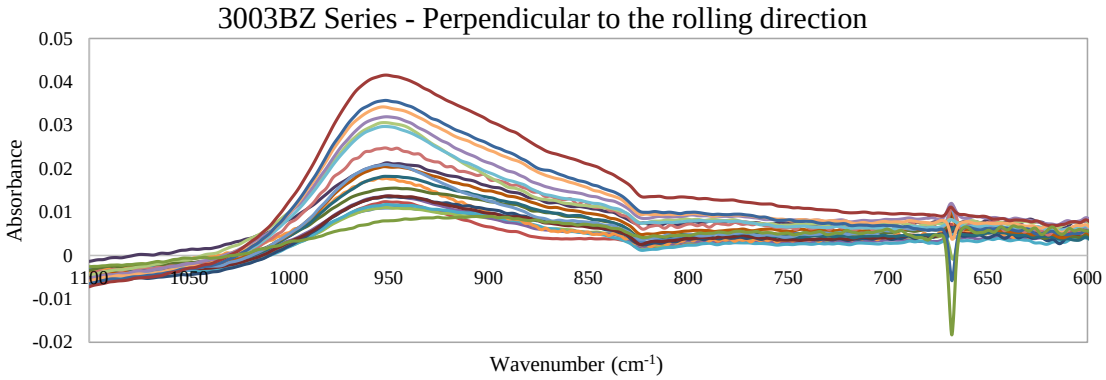

Figure 5.30. Narrowed range of wavenumbers from 1100 to 600 cm^{-1} for the baseline corrected FTIR spectra of 21 samples of 3003BZ series of aluminum alloy using Perkin Elmer FTIR Spectrometer coupled with Grazing Angle ATR.

The wavenumber shift in Figure 5.30 was not observed as significant as in 3005 series due to the absence of externally added magnesium which accounts for the wavenumber shift. In addition to 3005 and 3003BZ series alloys which has XPS reference values, GATR-FTIR spectra of two set of aluminum alloys namely 3105, 5005, 5052, 5754 series and 1050, 3003, 8006, 8156 series were taken. Figure 5.31, 5.32, 5.33 and 5.34 show the raw and baseline corrected spectra of 3105, 5005, 5052 and 5754 series alloys in perpendicular direction, respectively. The figure legends shown on the right side of each plot indicate the alloy series name, annealing temperature and annealing time with spaces between each term (e.g. '3105'-'200 ºC'- '1h' corresponds to the samples which is from 3105 series of aluminum alloy annealed at 200 ºC for 1 hour).

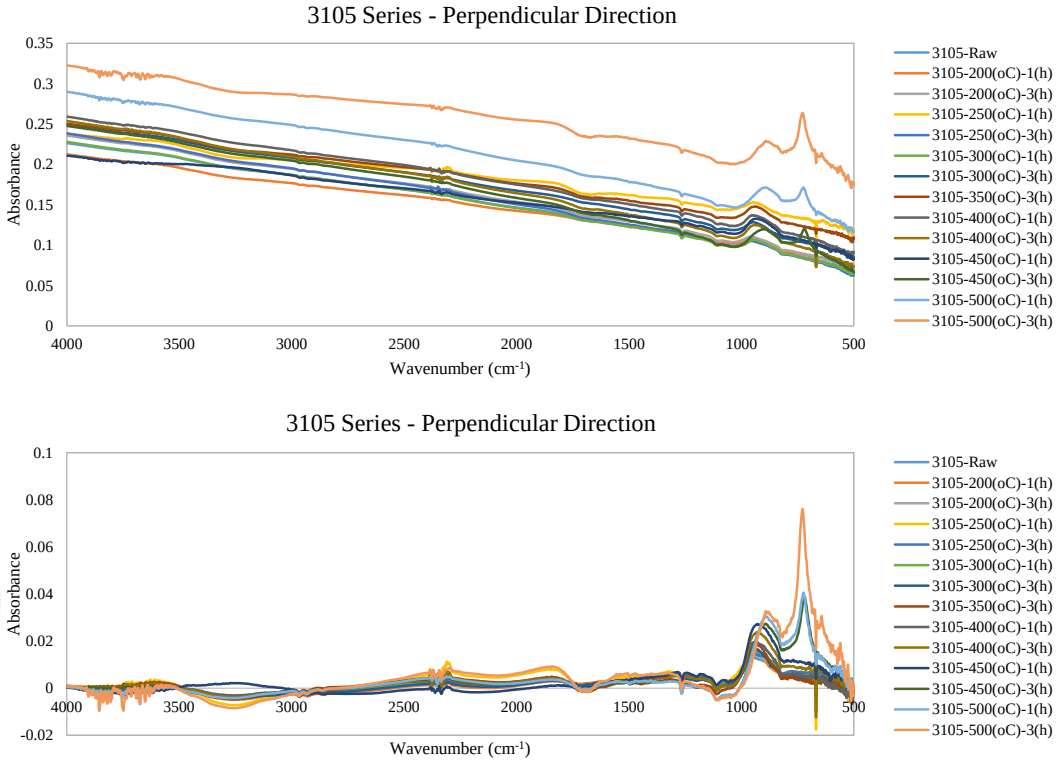

Figure 5.31. Raw and baseline corrected GATR-FTIR spectra of 3105 series alloys in perpendicular direction, respectively.

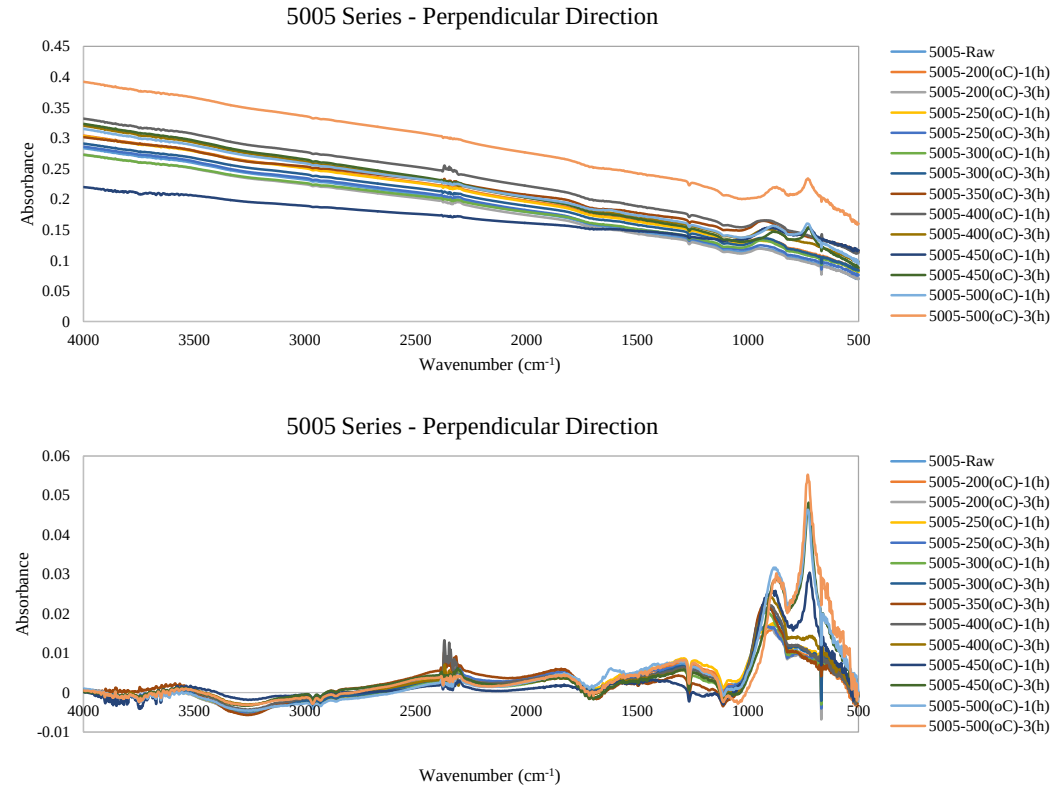

Figure 5.32. Raw and baseline corrected GATR-FTIR spectra of 5005 series alloys in perpendicular direction, respectively.

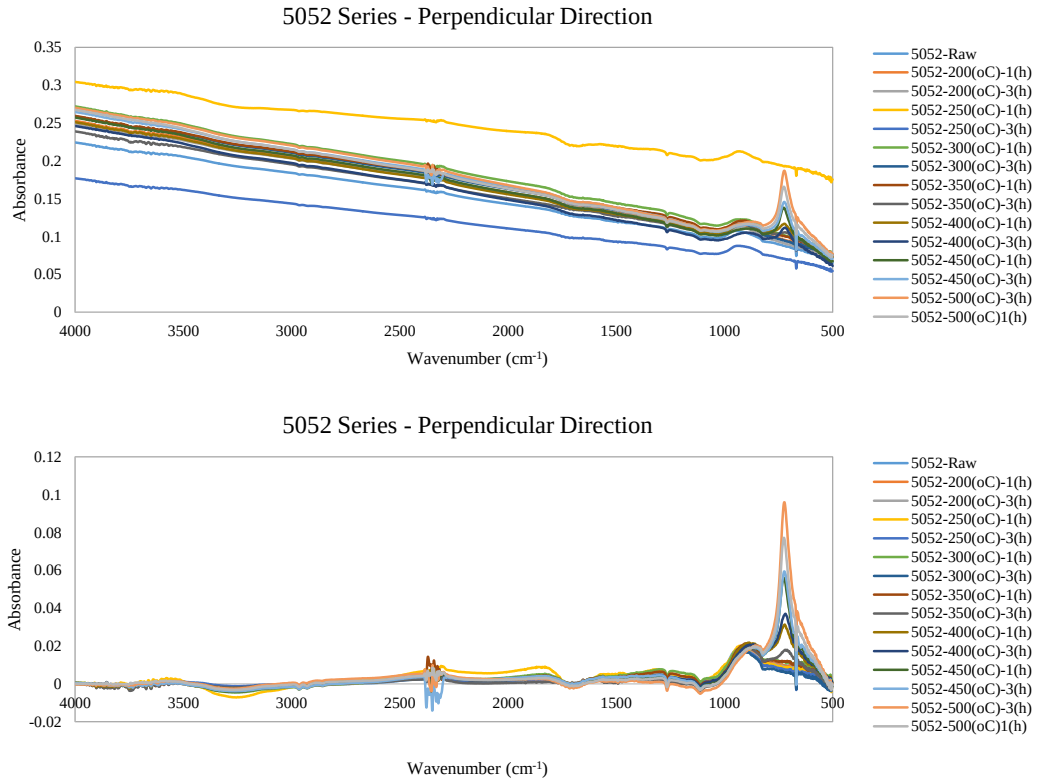

Figure 5.33. Raw and baseline corrected GATR-FTIR spectra of 5052 series alloys in perpendicular direction, respectively.

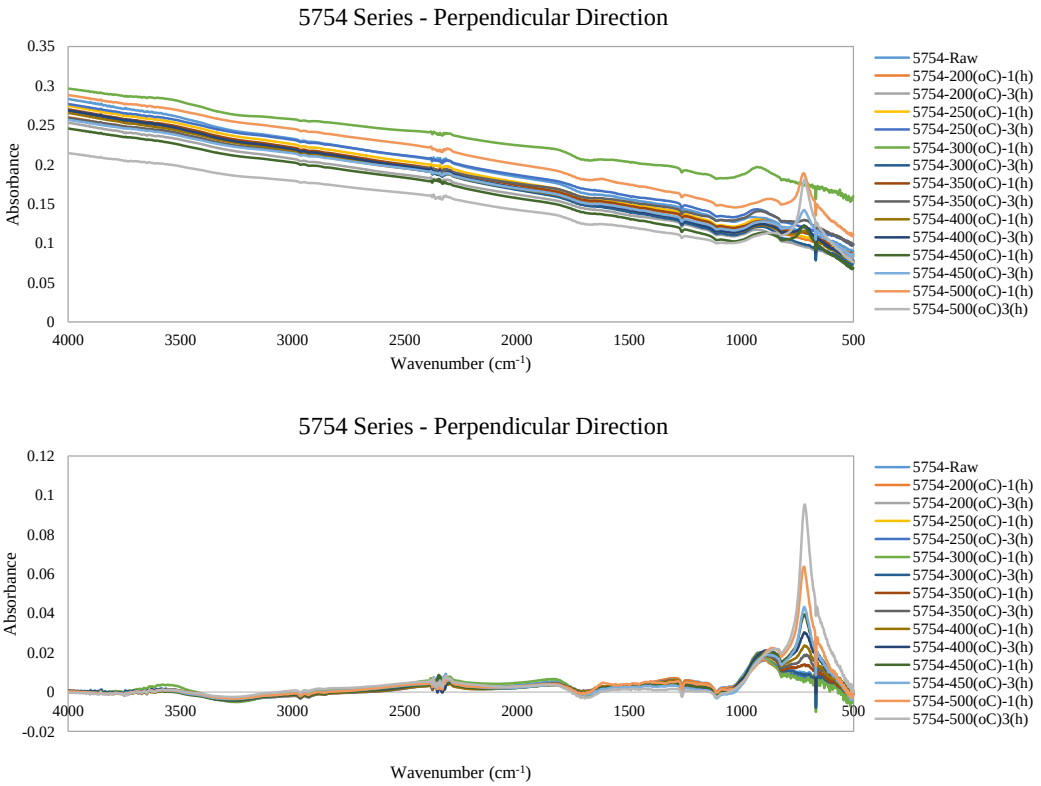

Figure 5.34. Raw and baseline corrected GATR-FTIR spectra of 5754 series alloys in perpendicular direction, respectively.

As shown in the figures above, raw and baseline corrected spectra of 3105, 5005, 5052 and 5754 series alloys have spectral similarity patterns to the 3005 series alloys having reference thickness measurements. Thus, the oxide thicknesses of these series alloys were predicted by the models generated with perpendicular measurements of 3005 series alloys. Similarly, Figure 5.35, 5.36, 5.37, 5.38 and 5.39 show the raw and baseline corrected spectra of 8006-1st trial, 8006-2nd trial, 1050, 3003 and 8156 series alloys in perpendicular direction, respectively.

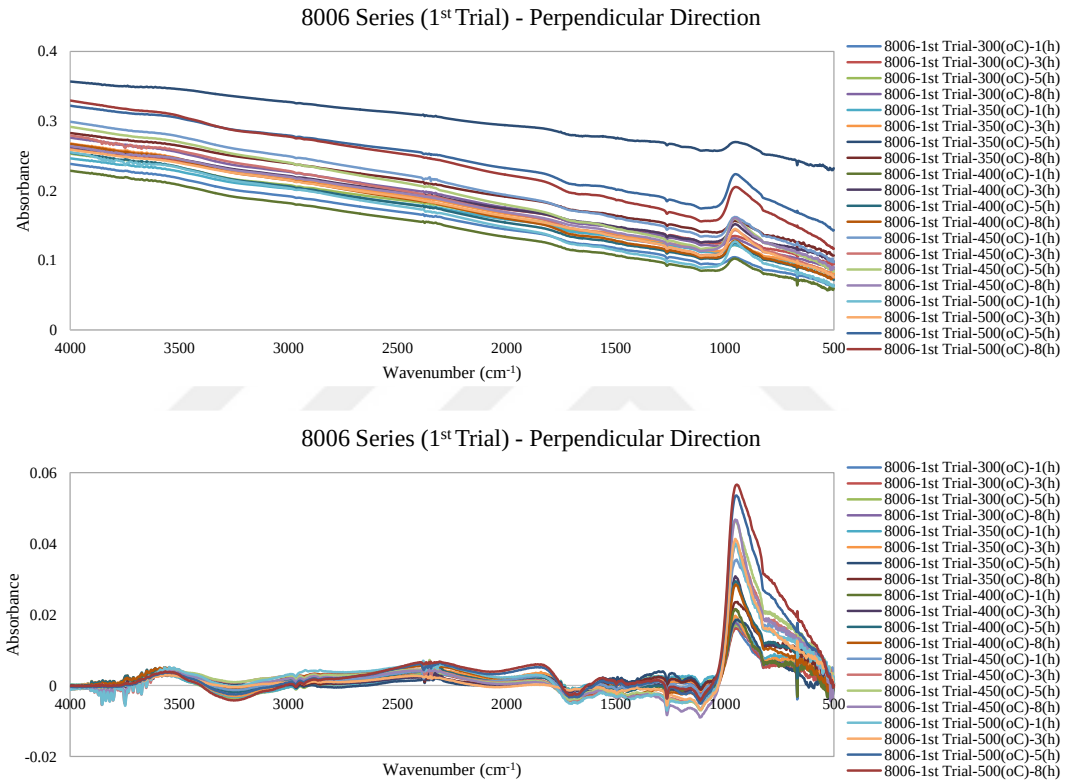

Figure 5.35. Raw and baseline corrected GATR-FTIR spectra of first trial of 8006 series alloys in perpendicular direction, respectively.

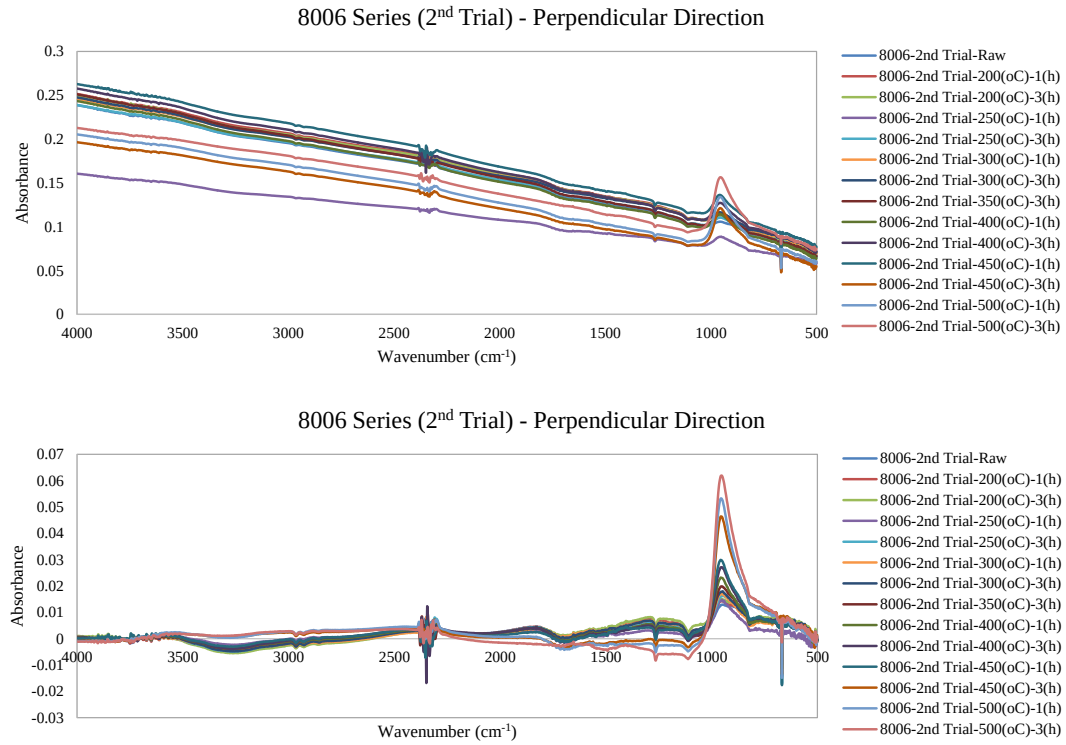

Figure 5.36. Raw and baseline corrected GATR-FTIR spectra of second trial of 8006 series alloys in perpendicular direction, respectively.

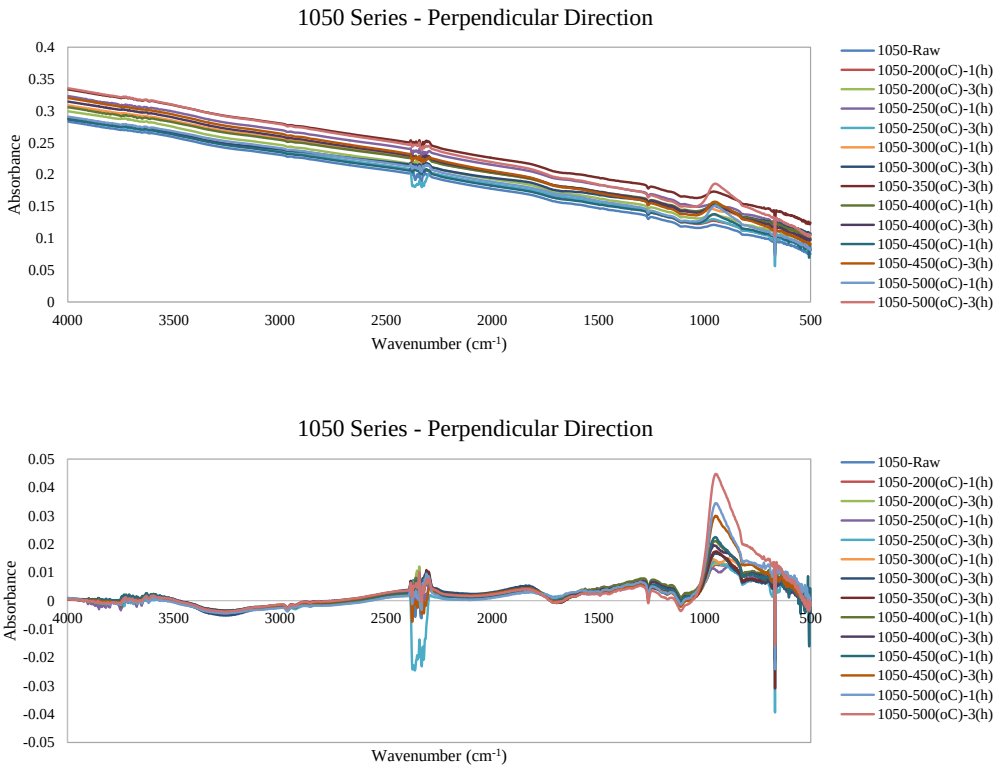

Figure 5.37. Raw and baseline corrected GATR-FTIR spectra of 1050 series alloys in perpendicular direction, respectively.

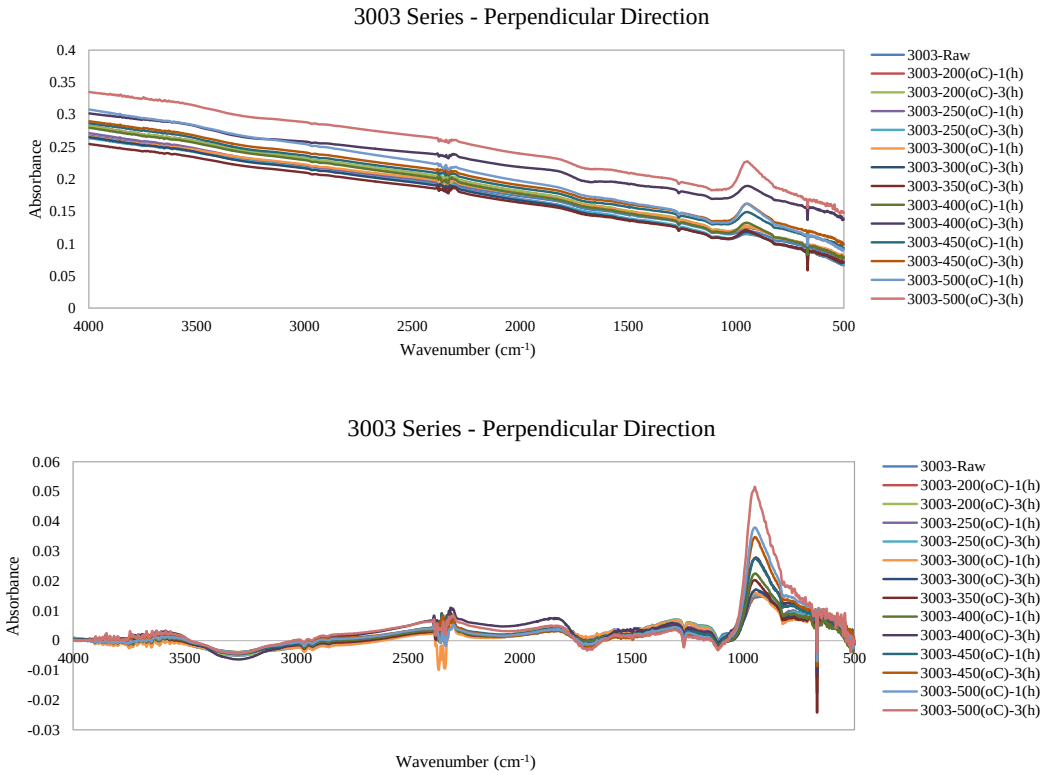

Figure 5.38. Raw and baseline corrected GATR-FTIR spectra of 3003 series alloys in perpendicular direction, respectively.

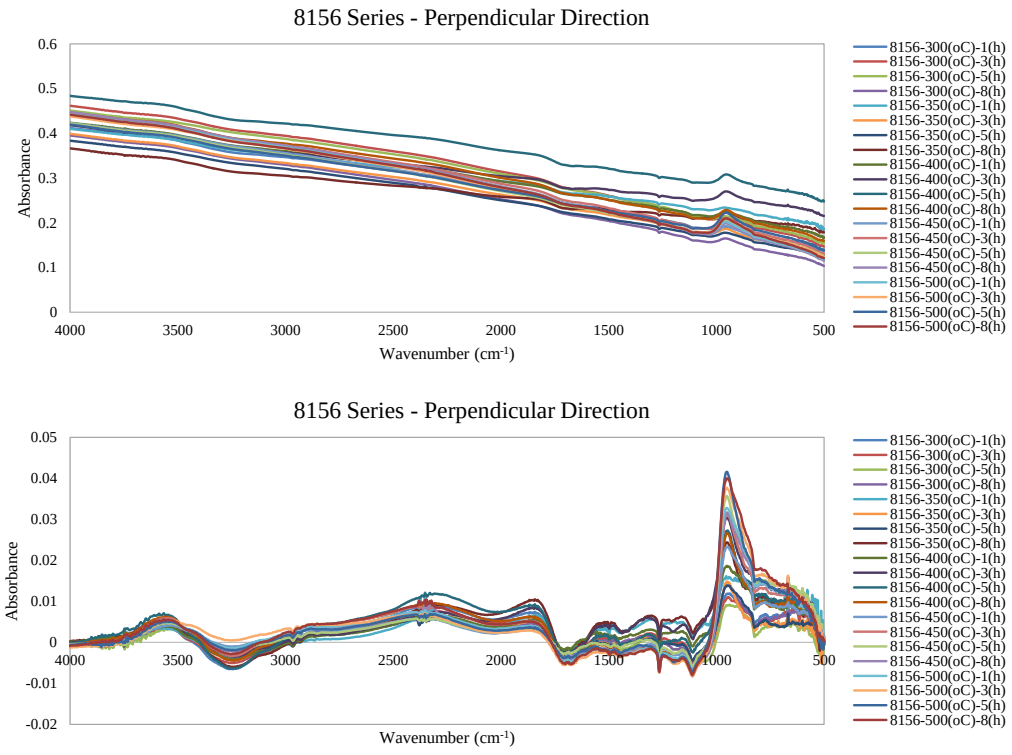

Figure 5.39. Raw and baseline corrected GATR-FTIR spectra of 8156 series alloys in perpendicular direction, respectively.

As it can be also seen from Figure 5.35-5.39 above, namely 8006, 1050, 3003 and 8156 series alloys have no externally added magnesium as in 3003BZ series alloys. Due to compositional similarity among these alloys, it is clear that there are also spectral similarity between them. Therefore, oxide thicknesses of these alloys were predicted by models generated with perpendicular measurements of 3003BZ series alloys.

After taking perpendicular direction measurements of two different series of aluminum alloys, parallel direction Grazing Angle ATR-FTIR measurements were performed for the same series.

5.3.3. Grazing Angle ATR-FTIR results of Parallel Direction

After obtaining Grazing Angle ATR-FTIR spectra of all the samples in perpendicular direction, aluminum samples were placed on Grazing Angle ATR accessory in parallel to the rolling direction, as shown in Figure 5.22. FTIR spectra of each series (3005 and 3003BZ), which have XPS reference analysis, were collected. Figure 5.40 shows the raw GATR-FTIR spectra of 3005 series of 21 samples whereas Figure 5.41 shows the raw GATR-FTIR spectra of 3003BZ series of 21 samples.

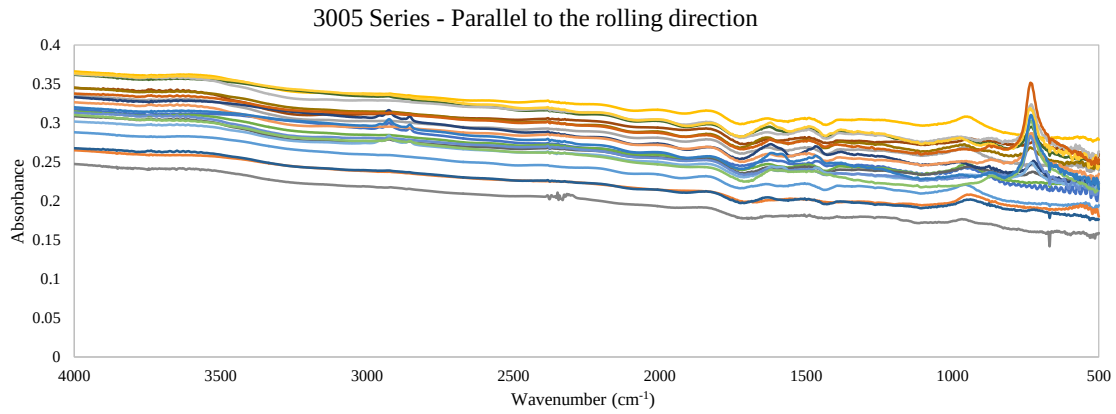

Figure 5.40. Raw FTIR spectra from Perkin Elmer FTIR Spectrometer coupled with Grazing Angle ATR of 21 samples of 3005 series alloys in parallel direction.

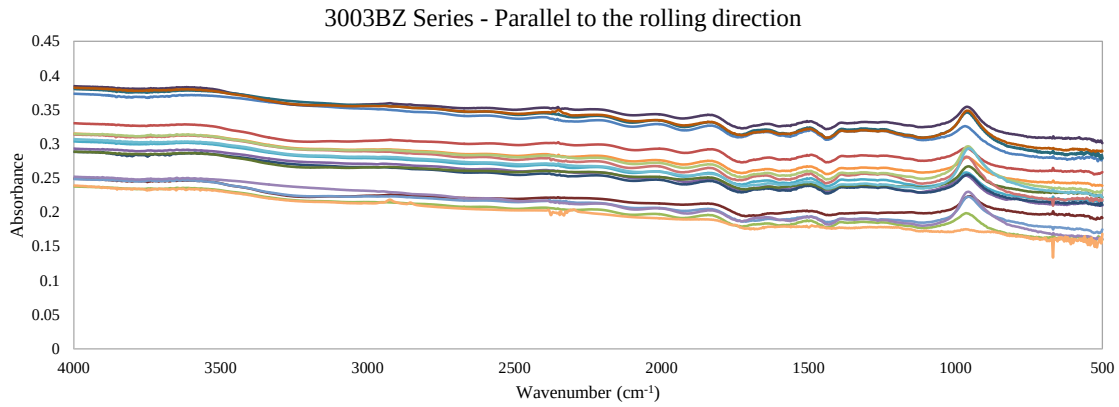

Figure 5.41. Raw FTIR spectra from Perkin Elmer FTIR Spectrometer coupled with Grazing Angle ATR of 21 samples of 3003BZ series alloys in parallel direction.

When the raw FTIR spectra of 3005 and 3003BZ series of aluminum given in Figure 5.40 and Figure 5.41 were examined closely, same baseline shift problem was observed similarly perpendicular direction measurements. Therefore, same baseline correction algorithm mentioned in section 5.3.2 was applied to FTIR spectra of both series obtained in parallel direction. Figure 5.42 shows baseline corrected FTIR spectra of 3005 series of aluminum alloys (in parallel direction) using baseline correction method. While Figure 5.42 shows the baseline corrected FTIR spectra of 3005 series, Figure 5.43 shows narrowed wavenumber range to focus oxide peaks.

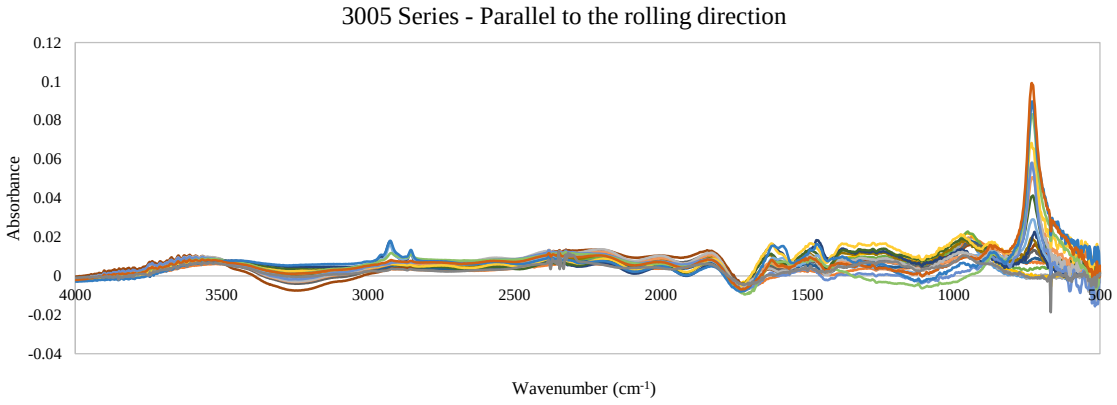

Figure 5.42. Baseline corrected FTIR spectra of 21 samples of 3005 series of aluminum in parallel direction using Perkin Elmer FTIR Spectrometer coupled with Grazing Angle ATR.

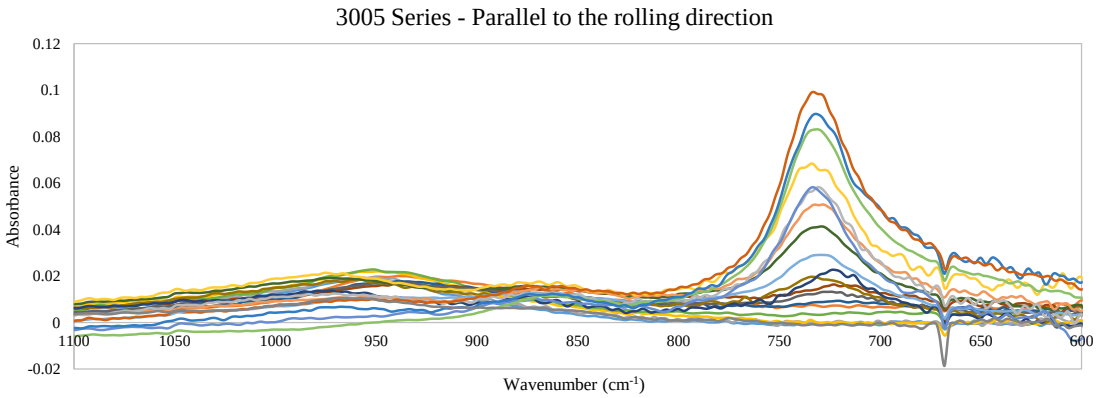

Figure 5.43. Narrowed range of wavenumber from 1100 to 600 cm^{-1} for the baseline corrected FTIR spectra of 21 samples of 3005 series of aluminum in parallel direction using Perkin Elmer FTIR Spectrometer coupled with Grazing Angle ATR.

When perpendicular and parallel measurements of GATR-FTIR spectra of 3005 series are compared, the intensity of magnesium oxide peaks in parallel direction measurements is higher than perpendicular direction measurements. As it can be seen clearly in Figure 5.43, the intensity of oxide peaks in parallel direction measurements is around 0.1, while the intensity of oxide peak in perpendicular direction measurements is around 0.08 as shown in Figure 5.28. In addition to this, compared to perpendicular direction measurement, a more dramatic shift in Al_2O_3 peak was observed in parallel direction measurements. Also, Figure 5.44 shows the baseline corrected FTIR spectra of 3003BZ series and Figure 5.45 shows the narrowed wavenumber range of 3003BZ series in order to focus oxide peaks.

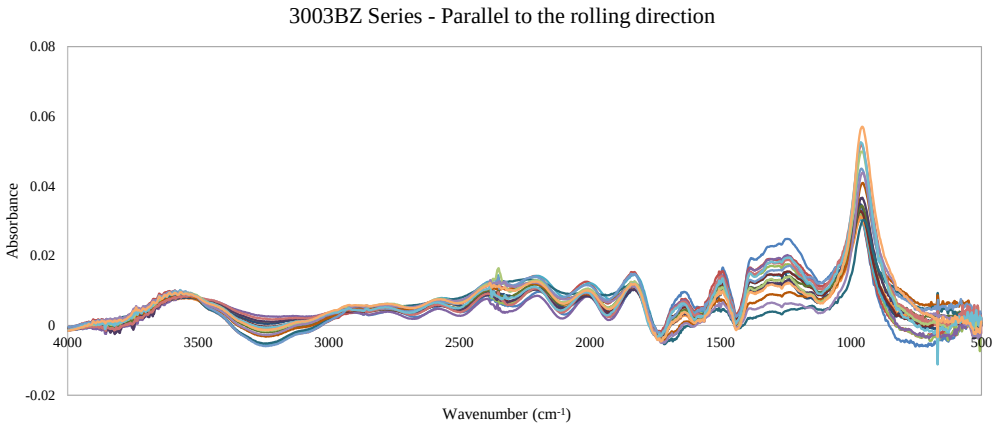

Figure 5.44. Baseline corrected FTIR spectra of 21 samples of 3003BZ series of aluminum in parallel direction using Perkin Elmer FTIR Spectrometer coupled with Grazing Angle ATR.

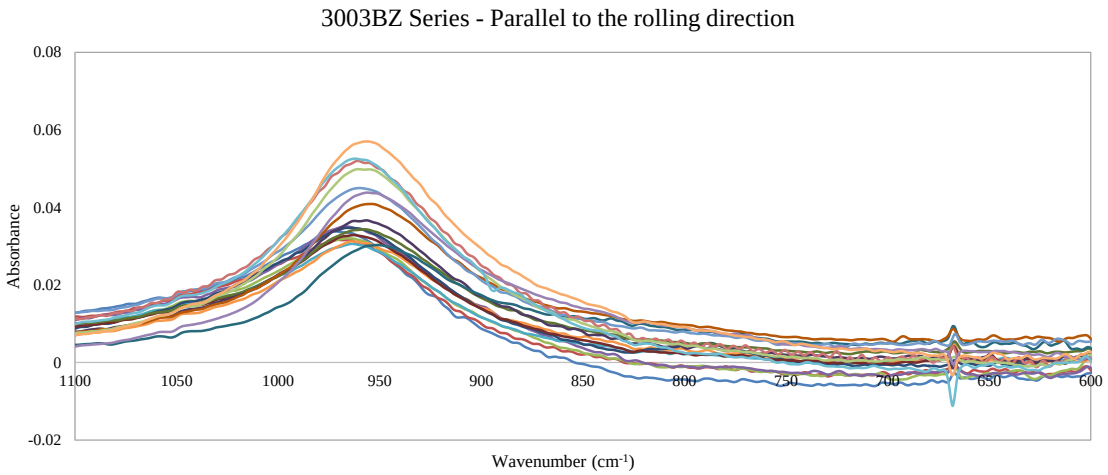

Figure 5.45. Narrowed range of wavenumber from 1100 to 600 cm^{-1} for the baseline corrected FTIR spectra of 21 samples of 3003BZ series of aluminum in parallel direction using Perkin Elmer FTIR Spectrometer coupled with Grazing Angle ATR.

Similar to perpendicular direction measurements, the wavenumber shift observed in Al_2O_3 peak in 3005 series was not observed in 3003BZ series in parallel direction measurements because of the absence of spinel formation.

As in perpendicular direction measurement, spectra of two set of aluminum alloys namely 3105, 5005, 5052, 5754 series and 1050, 3003, 8006 and 8156 series were obtained using GATR-FTIR in parallel direction. Figure 5.46, 5.47, 5.48 and 5.49 show the raw and baseline corrected spectra of 3105, 5005, 5052 and 5754 series aluminum alloys, respectively.

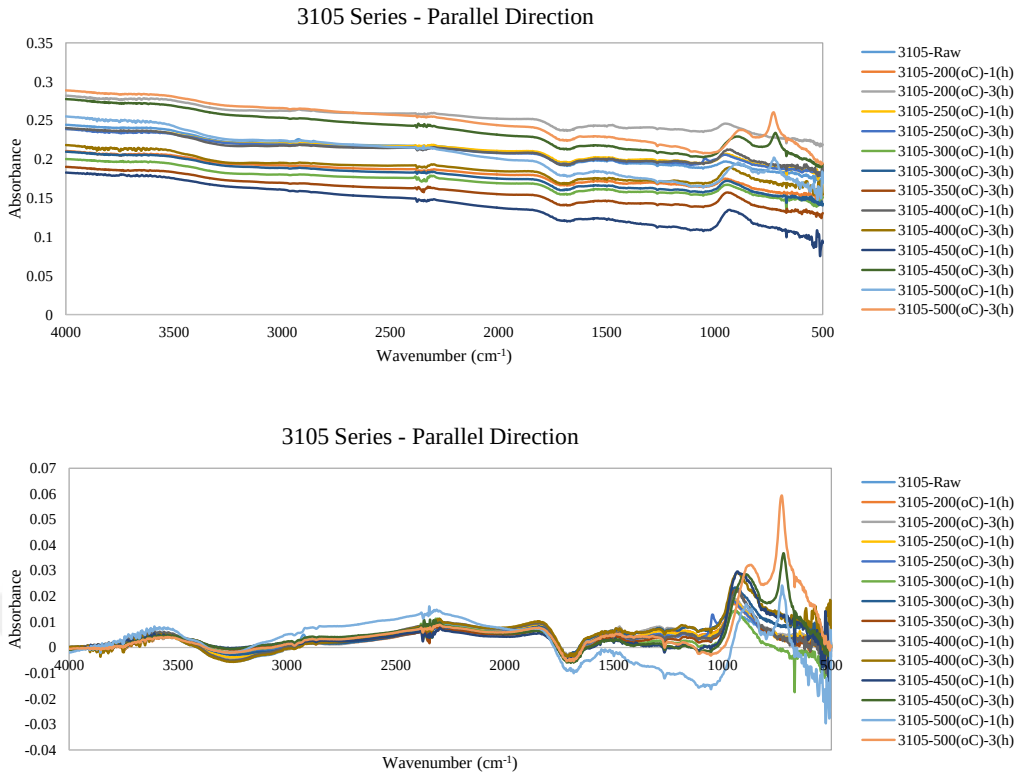

Figure 5.46. Raw and baseline corrected GATR-FTIR spectra of 3105 series alloys in parallel direction, respectively.

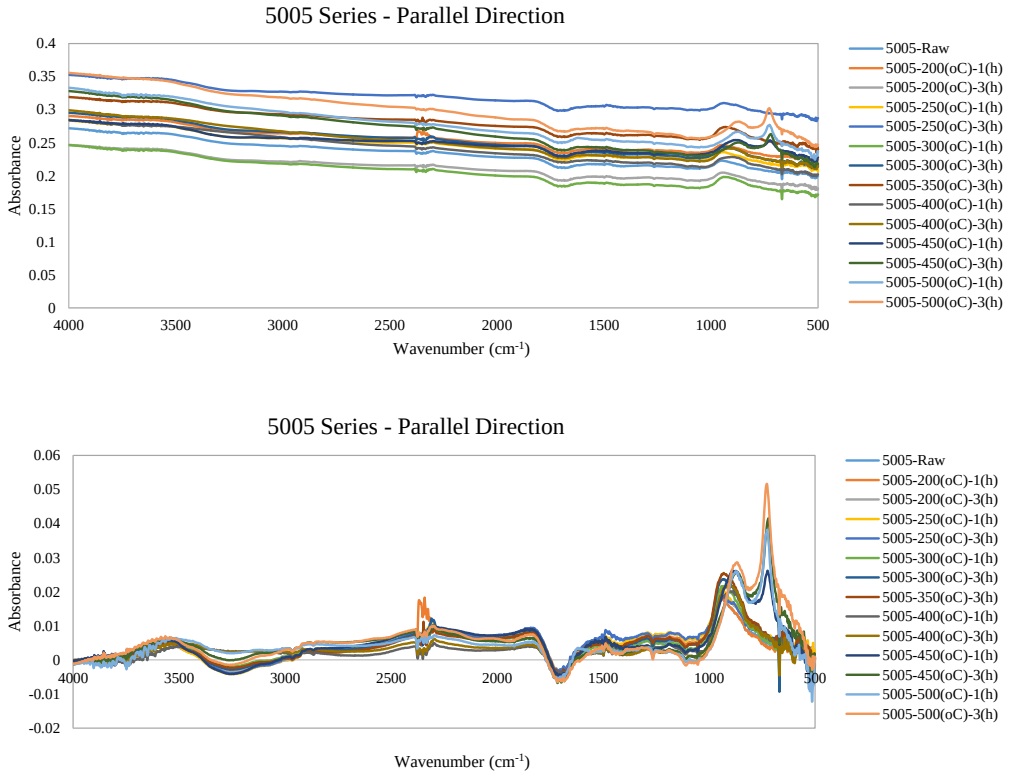

Figure 5.47. Raw and baseline corrected GATR-FTIR spectra of 5005 series alloys in parallel direction, respectively.

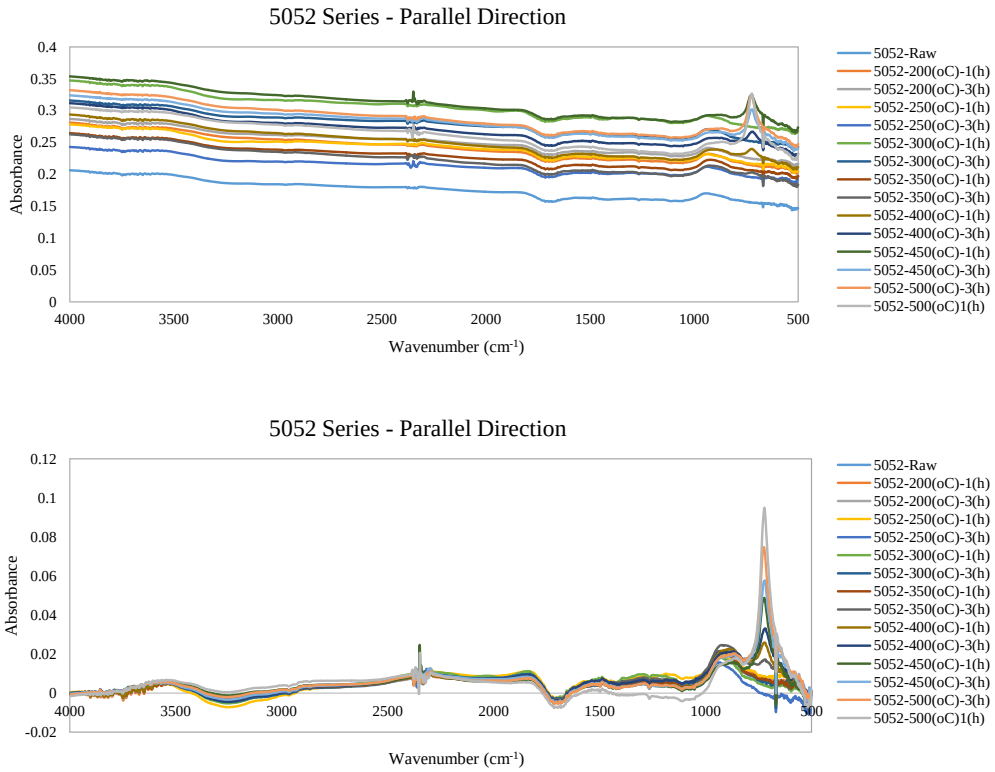

Figure 5.48. Raw and baseline corrected GATR-FTIR spectra of 5052 series alloys in parallel direction, respectively.

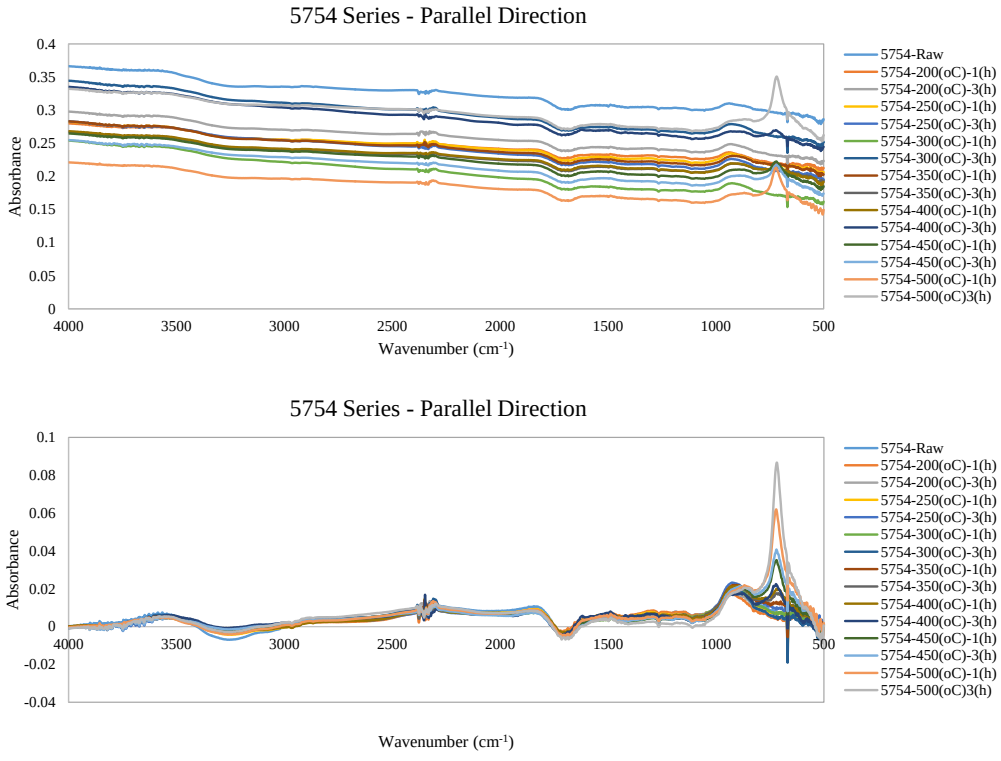

Figure 5.49. Raw and baseline corrected GATR-FTIR spectra of 5754 series alloys in parallel direction, respectively.

As shown in figures above, parallel measurements of namely 3105, 5005, 5052 and 5754 series alloys also have spectral similarity to parallel measurements of 3005 series alloys. Therefore, oxide thicknesses of those four series alloys were predicted by models generated with parallel measurements of 3005 series alloys. Similarly, Figure 5.50, 5.51, 5.52, 5.53 and 5.54 show the raw and baseline corrected spectra of 8006 - 1st Trial, 8006 - 2nd Trial, 1050, 3003 and 8156 series of aluminum alloys, respectively.

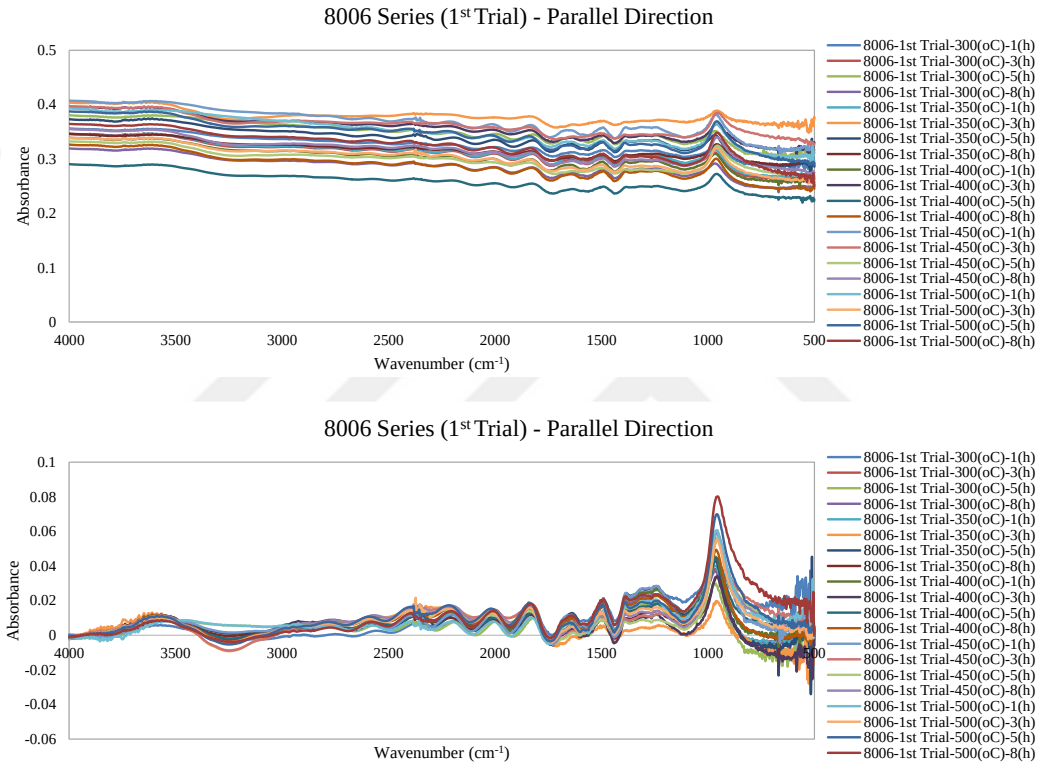

Figure 5.50. Raw and baseline corrected GATR-FTIR spectra of first trial of 8006 series alloys in parallel direction, respectively.

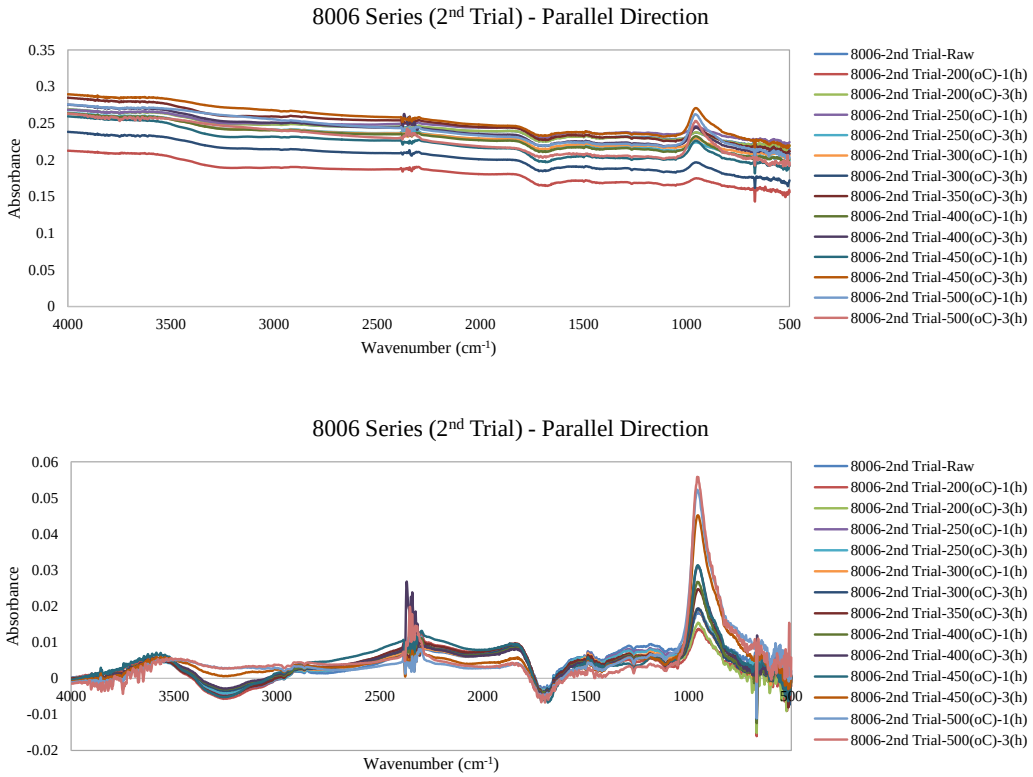

Figure 5.51. Raw and baseline corrected GATR-FTIR spectra of second trial of 8006 series alloys in parallel direction, respectively.

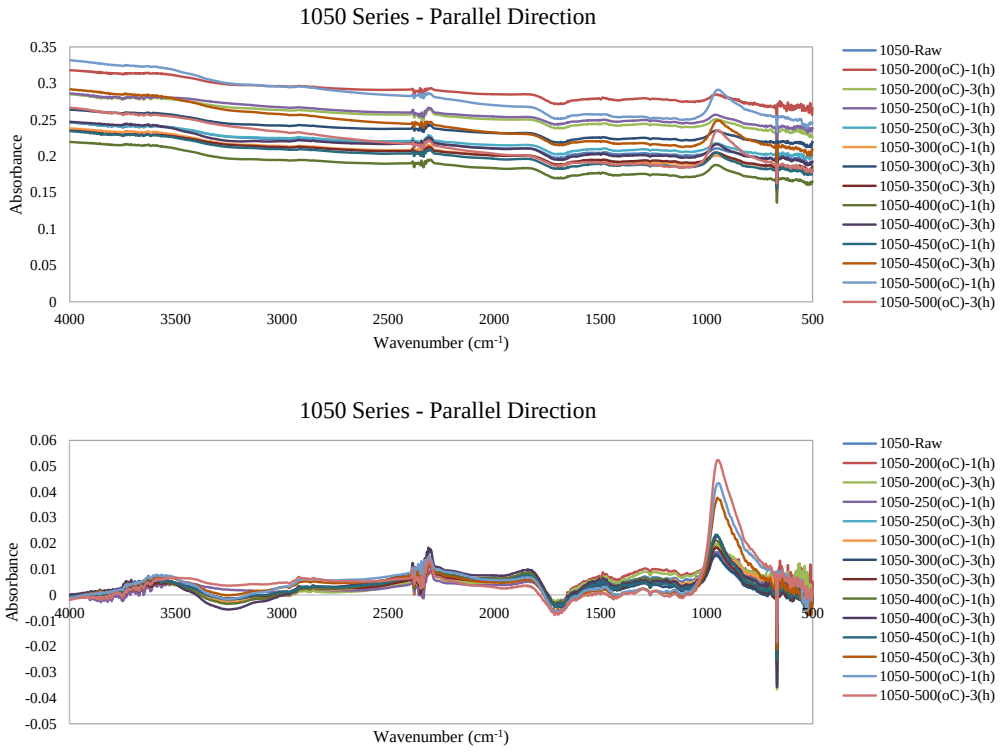

Figure 5.52. Raw and baseline corrected GATR-FTIR spectra of 1050 series alloys in parallel direction, respectively.

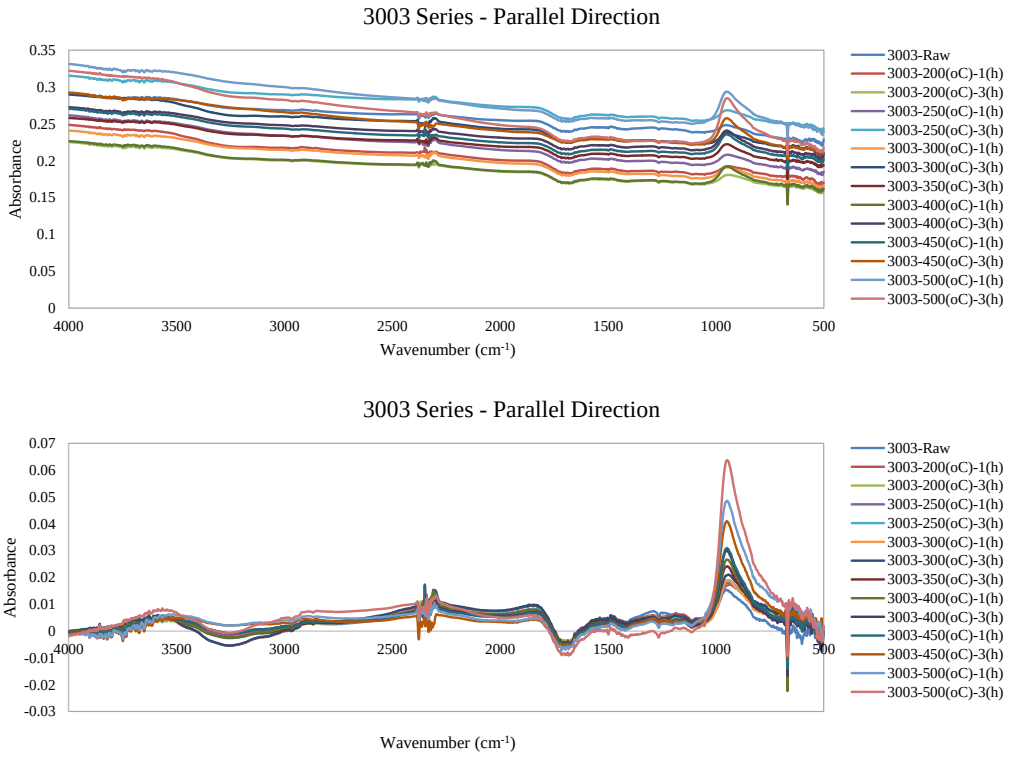

Figure 5.53. Raw and baseline corrected GATR-FTIR spectra of 3003 series alloys in parallel direction, respectively.

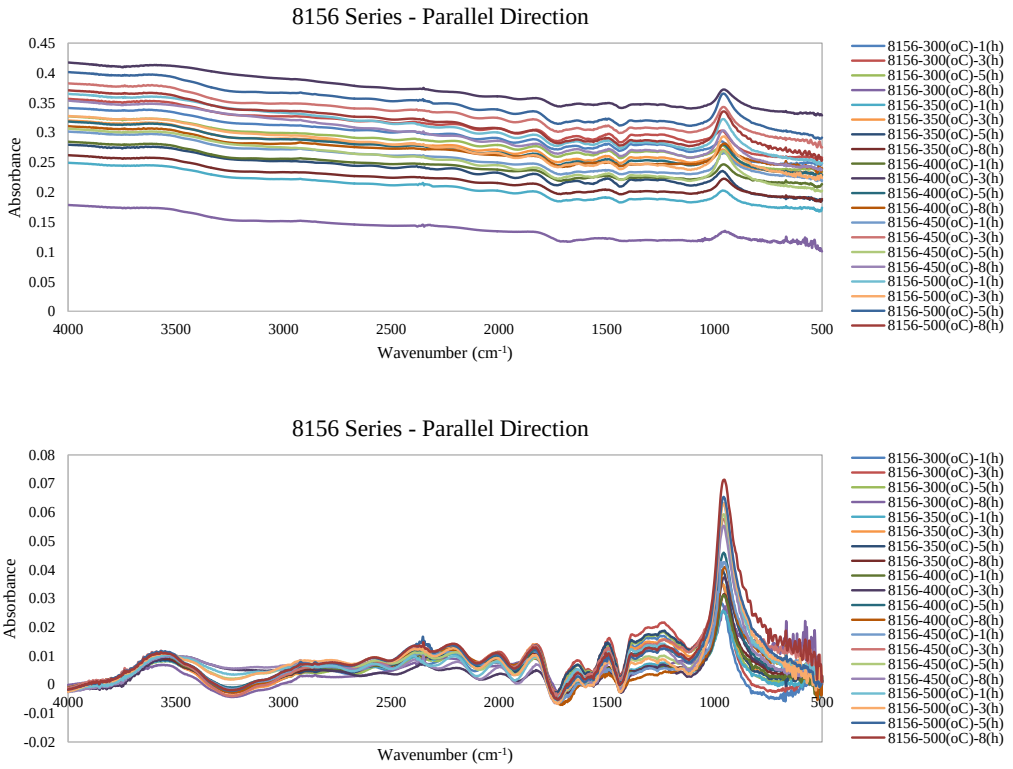

Figure 5.54. Raw and baseline corrected GATR-FTIR spectra of 8156 series alloys in parallel direction, respectively.

As it can be seen from figures above, parallel measurements of namely 8006, 1050, 3003 and 8156 series alloys have spectral and compositional similarity to parallel measurements of 3003BZ series alloys. Therefore, oxide thicknesses of those mentioned aluminum alloys were predicted by models generated with parallel measurements of 3003BZ series alloys.

Due to the serious shifts on peak maxima resulting from Al-Mg spinel formations explained in Figure 5.21, it is expected that the success of univariate calibration based on peak maxima would be insufficient. However, classical simple least squares regression was used to compare the results to multivariate calibration in order to assess predictive ability of multivariate models. Therefore, it is decided to apply simple least square procedure first for both aluminum oxide and magnesium oxide peaks in two different direction. The success of this models were reported in detail in the following section.

5.4. Univariate Calibration Results

5.4.1. Simple Least Squares Results of 3005 Series of Alloys in Perpendicular Direction

Simple least squares based on a single point calibration technique was applied to FTIR spectra shown in Figure 5.27 which belongs to 3005 series of aluminum alloys placed in perpendicular direction. As mentioned above, because of the wavelength shift occurred at high temperatures, it is hardly expected to obtain successful models with univariate calibration techniques. Nevertheless, in terms of creating integrity for this study, simple modelling technique was studied in the region of 900 cm^{-1} and 736 cm^{-1} corresponding to the maximum absorbance values. Figure 5.55 shows the univariate calibration graphs of 3005 series alloys where 736 cm^{-1} were chosen as the peak maxima of MgO. On the other hand, Figure 5.56 shows the univariate calibration graph using the maximum absorbance value at 900 cm^{-1} which is the peak maxima of Al_2O_3 peak.

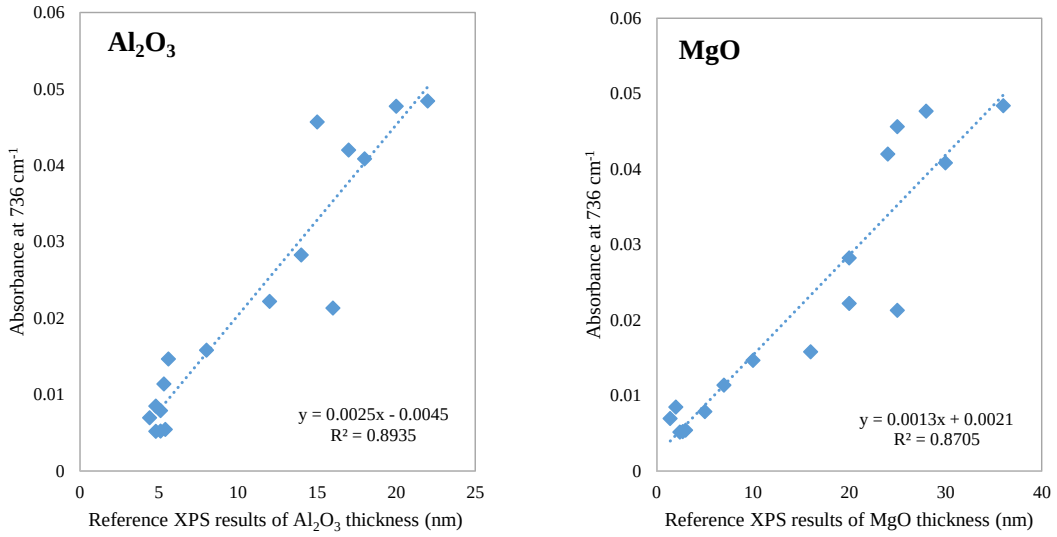

Figure 5.55. Simple calibration graphs of 3005 series alloys obtained by the simple least square method for Al_2O_3 and MgO at 736 cm^{-1} in perpendicular direction.

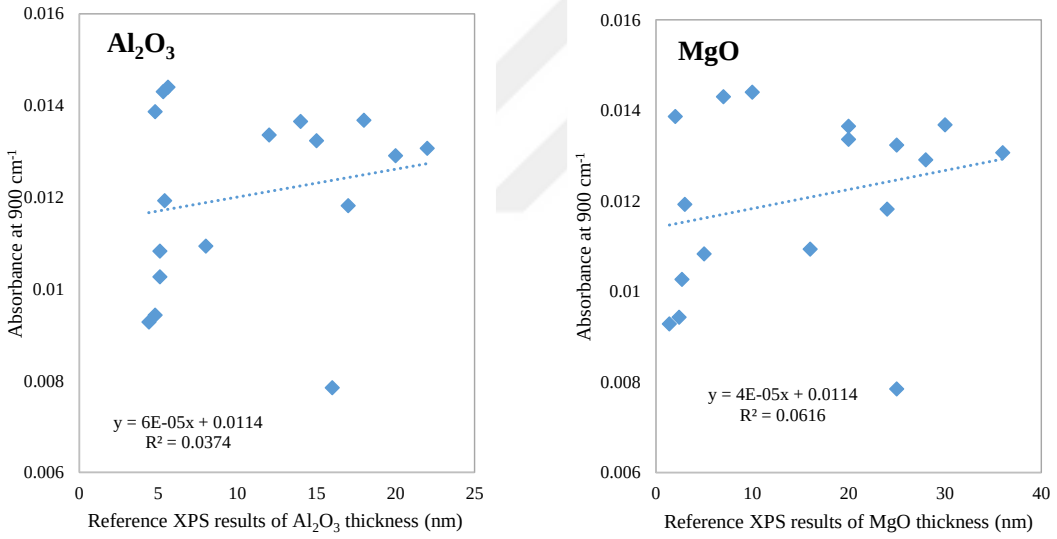

Figure 5.56. Simple calibration graphs of 3005 series alloys obtained by the simple least square method for Al_2O_3 and MgO at 900 cm^{-1} in perpendicular direction.

As given in the Table 5.1 and 5.2, calibration graphs for oxide thickness for 3005 series of aluminum alloys were plotted using 17 sample out of 21 samples because the thickness of three samples could not be determined by XPS due to the excessive time consumption. Although calibration graph between oxide thickness and the peak maximum of 736 cm^{-1} indicates a somewhat good correlation, in the other peak maxima (at 900 cm^{-1}) no correlations between oxide thickness and absorbance could be achieved.

At this point, it can be said that despite of having some correlations in the peak maximum of MgO, univariate calibration is not adequate to model oxide thickness.

In addition to calibration graphs above, FTIR spectra of 3005 series obtained in parallel direction was also used to check the correlation between aluminum and magnesium oxide thicknesses and their respective absorbance.

5.4.2. Simple Least Squares Results of 3005 Series of Alloys in Parallel Direction

After checking the correlation between aluminum and magnesium oxide thicknesses and their respective absorbance peaks in perpendicular direction measurements, simple least squares method was applied to FTIR spectra shown in Figure 5.42 which belongs to parallel measurement 3005 series alloys. Figure 5.57 shows the univariate calibration graph using the maximum absorbance value at 736 cm^{-1} which is the peak maxima of MgO peak whereas Figure 5.58 shows the univariate calibration graph using the maximum absorbance at 900 cm^{-1} which is the peak maxima of Al_2O_3 peak.

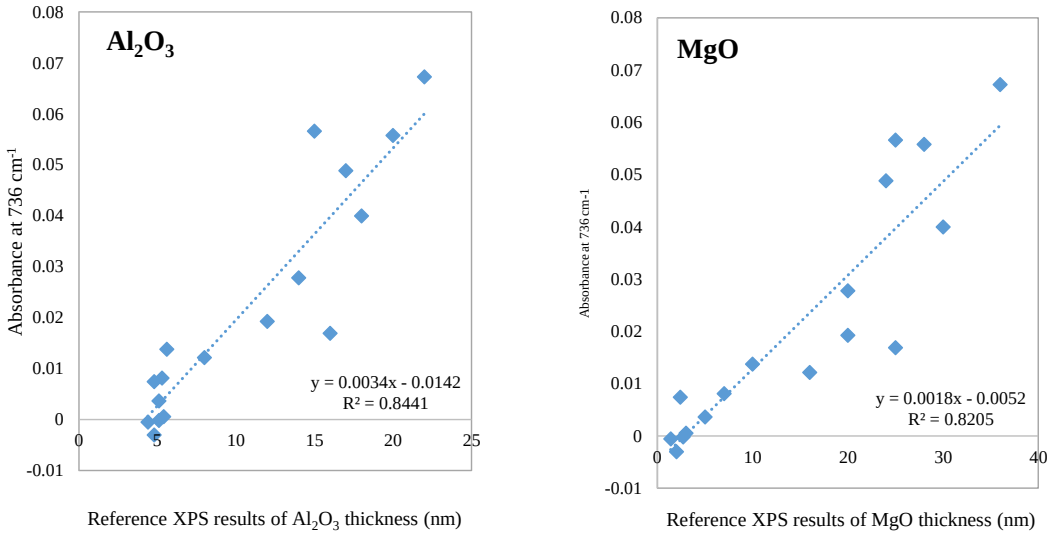

Figure 5.57. Simple calibration graphs of 3005 series alloys obtained by the simple least square method for Al_2O_3 and MgO at 736 cm^{-1} in parallel direction.

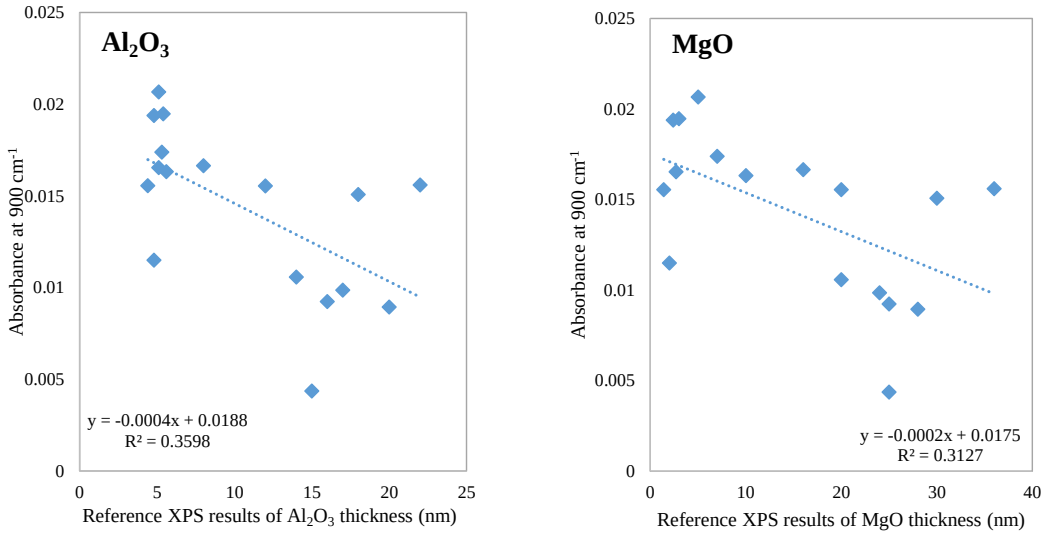

Figure 5.58. Simple calibration graphs of 3005 series alloys obtained by the simple least square method for Al_2O_3 and MgO at 900 cm^{-1} in parallel direction.

As can be seen from figures above, while there is a somewhat good correlation between oxide thicknesses and peak maxima at 736 cm^{-1} shown in Figure 5.57, Figure 5.58 shows poor correlation in the other peak maxima at 900 cm^{-1}. When compared to univariate calibration modelling with perpendicular measurement results, it can be said that perpendicular measurement results are in better correlation at peak maximum of 736 cm^{-1} than parallel one, when regression coefficients are compared. This might be the results of more significant baseline shifts observed in parallel measurement of FTIR spectra than perpendicular measurements. The other noticeable thing is that, negative correlation was observed when using absorbance value at 900 cm^{-1} in parallel measurements while there is a positive correlation in perpendicular one.

In addition to calibration graphs, oxide thicknesses of several aluminum alloys namely 3105, 5005, 5052 and 5754, which were mentioned in Experimental section and have no XPS reference data, were predicted by their respective univariate calibration models. Because correlation in absorbance maxima at 900 cm^{-1} did not provide successful models in both directions, these mentioned alloys were predicted by univariate models constructed with maximum absorbance at 736 cm^{-1}.

Predicted Al_2O_3 and MgO thicknesses of 3105, 5005, 5052 and 5754 series alloys by using univariate calibration models will be given in Multivariate Calibration Results section order to have a complete comparison with GILS and GPLS predicted oxide thicknesses.

5.4.3. Simple Least Squares Results of 3003BZ Series of Alloys in Perpendicular Direction

As can be seen in perpendicularly measured FTIR spectra which belongs to 3003BZ series of alloys in Figure 5.29, the peak at 960 cm^{-1} that represents Al_2O_3 is observed. However, the intensity of MgO peak at 736 cm^{-1} was observed to be very weak in comparison to 3005 series. The main reason is that 3003BZ series have no additional magnesium in its content. As shown in Table 5.4, although magnesium was not added, there was still a trace amount of magnesium in natural aluminum. Another important aspect is, unlike 3005 series, significant shifts were not observed in Al_2O_3 peak. As in 3005 series, simple least squares (SLS) models were also fit to 3003BZ series in both directions. Calibration graphs for Al_2O_3 peak maximum at 960 cm^{-1} which belongs to perpendicular measurement is given in Figure 5.59.

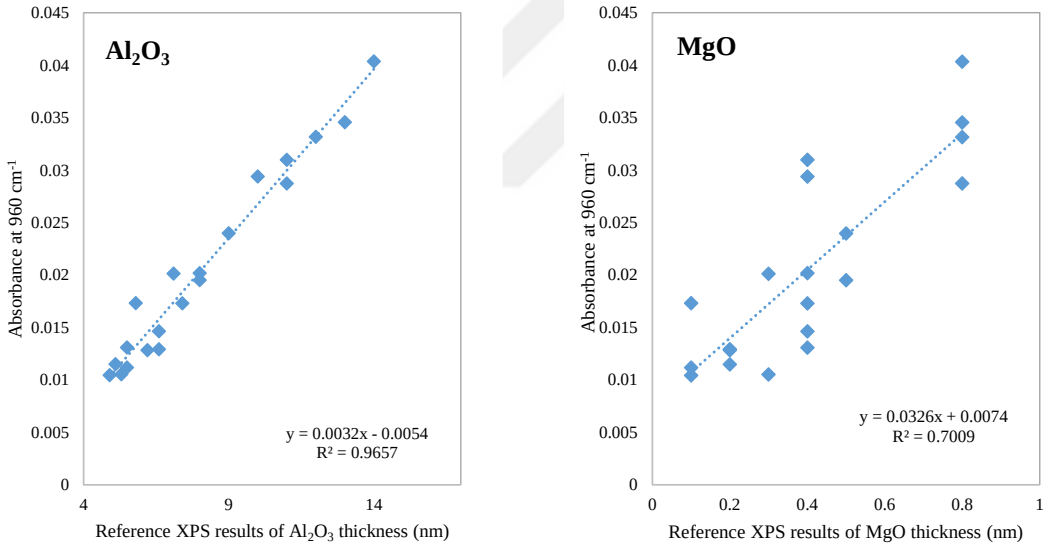

Figure 5.59. Simple calibration graphs of 3003BZ obtained by the simple least squares method for Al_2O_3 and MgO at 960 cm^{-1} in perpendicular direction.

From the calibration graphs shown in Figure 5.59, simple calibration modelling studies can be considered successful for Al_2O_3 but the same success could not be achieved for MgO. At this point it is worth mentioning that the dynamic range for the determination of MgO thickness is between 0.01 to 0.81 nm. Simple least squares modelling study was also performed with parallel measurement 3003BZ series alloys which is shown in following section.

5.4.4. Simple Least Squares Results of 3003BZ Series of Alloys in Parallel Direction

Simple calibration modelling studies for 3003BZ series of alloys were studied by using respective FTIR spectra of 3003BZ series alloys in parallel direction measurements shown in Figure 5.44. Therefore, Figure 5.60 shows the univariate calibration graphs of Al_2O_3 and MgO using the peak maxima of Al_2O_3 at 960 cm^{-1} in perpendicular direction.

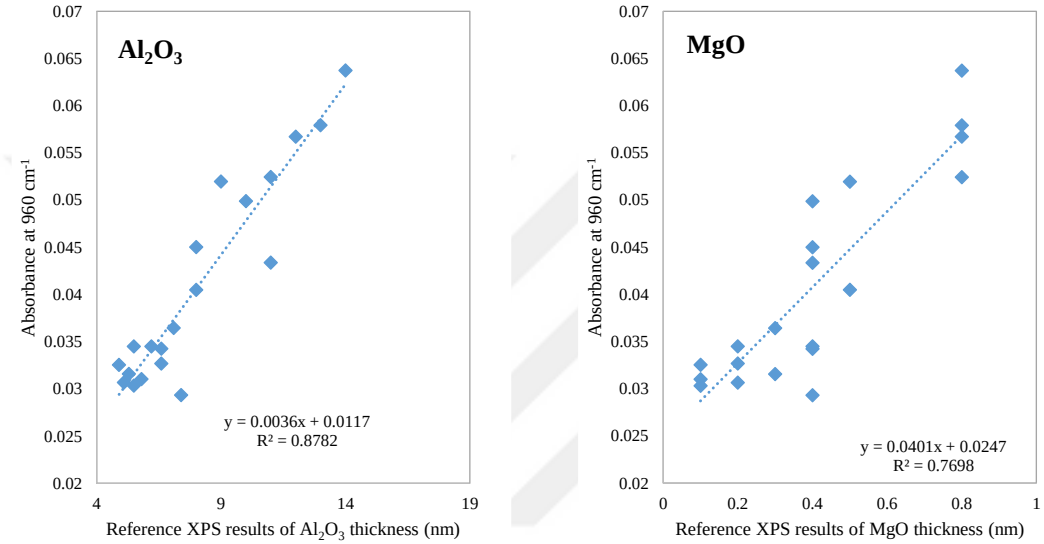

Figure 5.60. Simple calibration graphs of 3003BZ obtained by the simple least squares method for Al_2O_3 and MgO at 960 cm^{-1} in parallel direction.

As can be seen from calibration graphs in Figure 5.60, similar to perpendicular measurement results, there is a good correlation between oxide thicknesses and maximum absorbance value at 960 cm^{-1}.

Oxide thicknesses of several aluminum alloys namely, 8006, 1050, 3003 and 8156, which have no XPS oxide thickness reference data, were also predicted by constructed univariate calibration models using their respective 3003BZ series alloys. Results of predicted oxide thicknesses for both Al_2O_3 and MgO will be compared with respective GILS and GPLS results in Multivariate Calibration Results.

After all univariate calibration results were obtained, it was decided to generate multivariate calibration models. The next section describes a detail discussion of the modelling studies performed with GILS and GPLS multivariate calibration methods.

5.5. Multivariate Calibration Results

In this study, multivariate calibration methods, which are GILS and GPLS mentioned in Chapter 3, were used to develop models that can relate the XPS reference oxide thickness measurements with Grazing Angle ATR FTIR spectra. Since a genetic algorithm is used for variable selection and optimization in both GILS and GPLS, it is important to set these methods with a predefined gene number, iteration number and the number of repeated run. For this, both methods were set to run with 30 genes, 50 iterations and 100 runs. Therefore, the results that are given for all the scenarios in the following sections are generated from the averages of best runs coming from 100 repeated execution of the methods.

The fact that two different type of aluminum alloy (the one with the added magnesium and the one with only natural magnesium content) were selected to model oxide formation on aluminum surfaces, the results of the modelling studies were given under two sub-headings for each multivariate calibration methods. In addition, the results of each alloy were also discussed under each method separately. Since there were two different direction measurements, each multivariate calibration method were performed for perpendicular and parallel direction measurements. As it was shown in FTIR results section, there were also several other alloys which resembles to the alloys used to generate models were also studied in order to demonstrate the predicted ability of the multivariate calibration models. Those mentioned aluminum alloys were used to compare perpendicular and parallel measurement multivariate modelling studies and resulting graphs are shown after multivariate calibration results. Multivariate calibration studies were divided into two main groups which represents the orientation of the samples while collecting FTIR spectra of aluminum alloys and the results are given in the next section.

5.5.1. Perpendicular Direction Multivariate Calibration Results

First multivariate calibration modelling studies were performed with using perpendicular measurements of 3005 and 3003BZ series of alloys. Both GILS and GPLS modelling studies for 3005 and 3003BZ series alloys are given in following section.

5.5.1.1. GILS Results for 3005 Series of Aluminum Alloys

Using XPS results of 3005 series of aluminum alloys given in Table 5.1 and Table 5.2, 14 out of 17 samples and the un-annealed sample giving a total of 15 samples were used to construct the calibration models and the remaining 3 samples were used to build independent validation set in order to assess the success of the models. Multivariate calibration models were built with the baseline corrected GATR-FTIR spectra belongs to perpendicular measurement of 3005 series alloys given in Figure 5.27. Actual vs. predicted plots for the thicknesses of Al_2O_3 and MgO are given in Figure 5.61 where the actual values are obtained by XPS analyses. Standard error of cross validation (SECV) and standard error of prediction (SEP) of models along with maximum and minimum values of oxide thickness are given in Table 5.13.

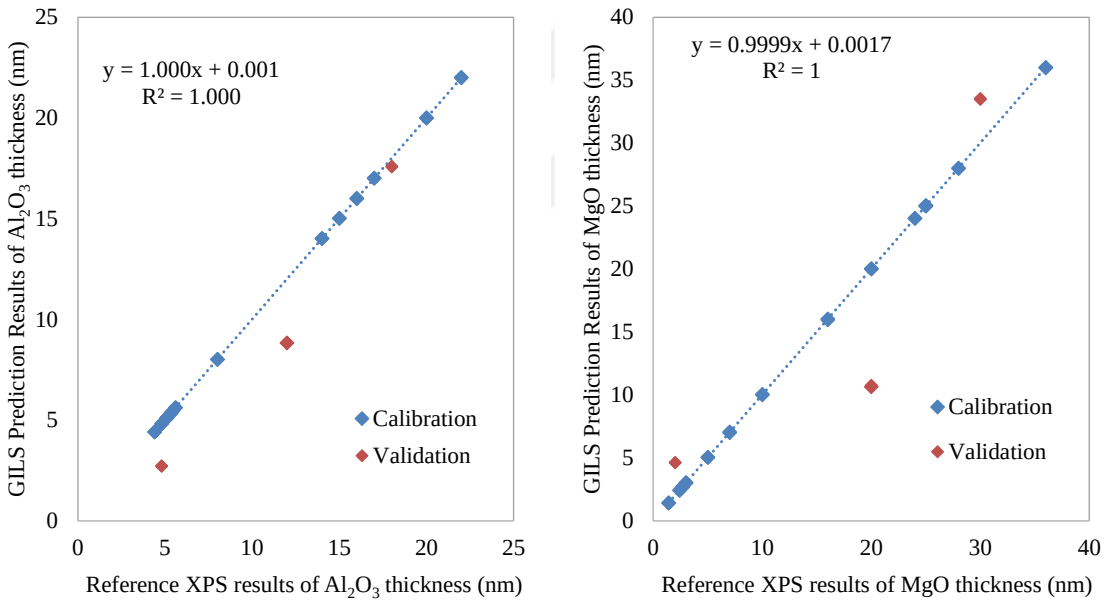

Figure 5.61. Reference XPS results of Al_2O_3 and MgO vs GILS predicted oxide thickness graphs of the 3005 series of aluminum alloys in perpendicular direction.

Table 5.13. Standard error of cross validation (SECV) and standard error of prediction (SEP) of GILS models along with the maximum and minimum oxide thicknesses of 3005 series in perpendicular direction.

	SECV (nm)	SEP (nm)	Max (nm)	Min (nm)
Al_2O_3	8.0×10^{-3}	2.2	22.0	4.4
MgO	2.2×10^{-2}	5.9	36.0	1.4

Although univariate calibration approach was unable to generate successful models, multivariate calibration approach using GILS method resulted in somewhat over fitted models for the calibration and independent validation sets in the determination of both Al_2O_3 and MgO as shown in Figure 5.61. Despite of having only three samples for independent validation sets, these predictions seems to be successful. When standard error of prediction values (SEP) were analyzed, however, for both oxide thickness analysis SEP value was higher than SECV value. The main reason of these high errors were the samples size of calibration sets which was only 15 and this causes an overfitting on the models. Another point to be addressed is that when evaluating SECV and SEP values, it is important to consider the dynamic range (maximum and minimum) of oxide thicknesses, given in Table 5.13.

5.5.1.2. GILS Results for 3003BZ Series of Aluminum Alloys

After relatively successful modelling studies using GILS method and FTIR spectra of perpendicular measurement of 3005 series of aluminum, another GILS modelling study was performed using the other aluminum alloy series called as 3003BZ which also has reference XPS measurements. Using the oxide thicknesses in Table 5.3 and Table 5.4 that are obtained by XPS as a reference thicknesses and their FTIR spectra shown in Figure 5.29, GILS modelling studies were performed. A total of 16 out of 20 samples were used to construct calibration sets and the remaining 4 samples were used as an independent validation set. The results of GILS predictions of Al_2O_3 thicknesses and MgO thicknesses with their corresponding XPS reference oxide thicknesses are given in the Figure 5.62. Standard error of cross-validation (SECV) and standard error of prediction (SEP) along with maximum and minimum values of oxide thicknesses are also given in Table 5.14.

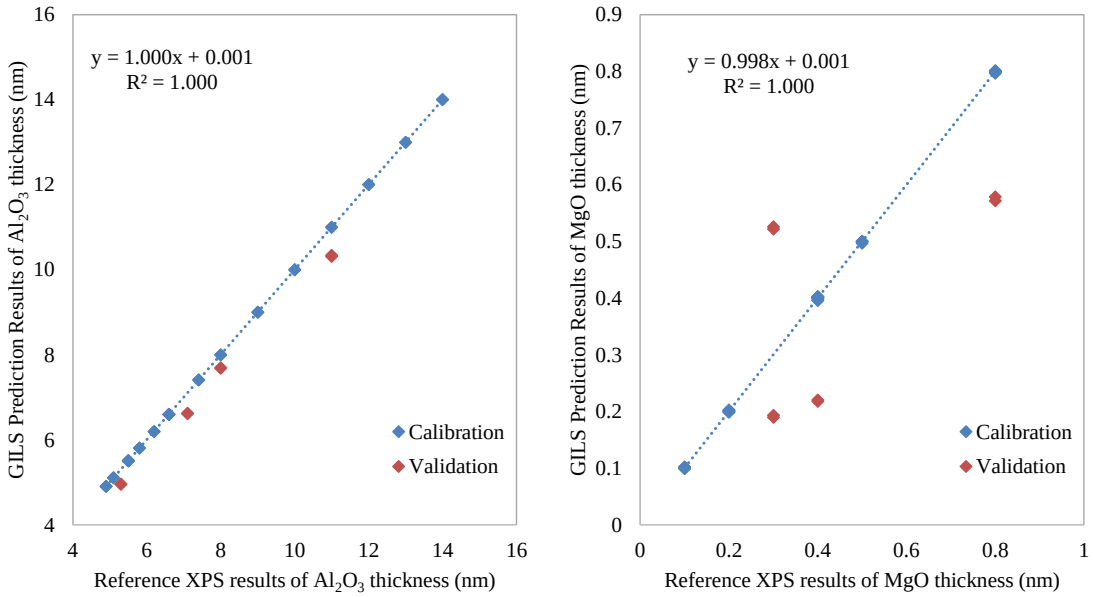

Figure 5.62. Reference XPS results of Al_2O_3 and MgO vs GILS predicted oxide thickness graphs of the 3003BZ series of aluminum alloys in perpendicular direction.

Table 5.14. Standard error of cross validation (SECV) and standard error of prediction (SEP) of GILS models along with maximum and minimum oxide thicknesses of 3003BZ series in perpendicular direction.

	SECV (nm)	SEP (nm)	Max (nm)	Min (nm)
Al_2O_3	0.005	0.48	14.0	4.9
MgO	0.002	0.19	0.8	0.1

When the success of simple least square and GILS methods are compared, GILS provided strongly over fitted models for 3003BZ series having both Al_2O_3 and MgO as the source of oxide thicknesses. On the other hand, the success of GILS calibration models for the prediction of independent validation set for MgO is much lower than Al_2O_3 model. This result is reflected in the standard error of cross validation and prediction values where MgO shows higher prediction error but in this point the dynamic range of the MgO model should be considered which is varies only in between 0.1 nm and 0.8 nm.

5.5.1.3. GPLS Results for 3005 Series of Aluminum Alloys

Same 3005 series of aluminum alloys used to construct GILS models were also used to construct GPLS models. From 17 samples, 14 of them are chosen to be calibration set in addition to the un-annealed sample resulting in a 15 sample for the calibration set

and the rest of them (3 of them) were used to build independent validation set as indicated in GILS modelling part. Reference XPS results vs GPLS predicted results for both Al_2O_3 and MgO are shown in Figure 5.63. SECV and SEP along with the range of oxide thicknesses that were studied are given in Table 5.15.

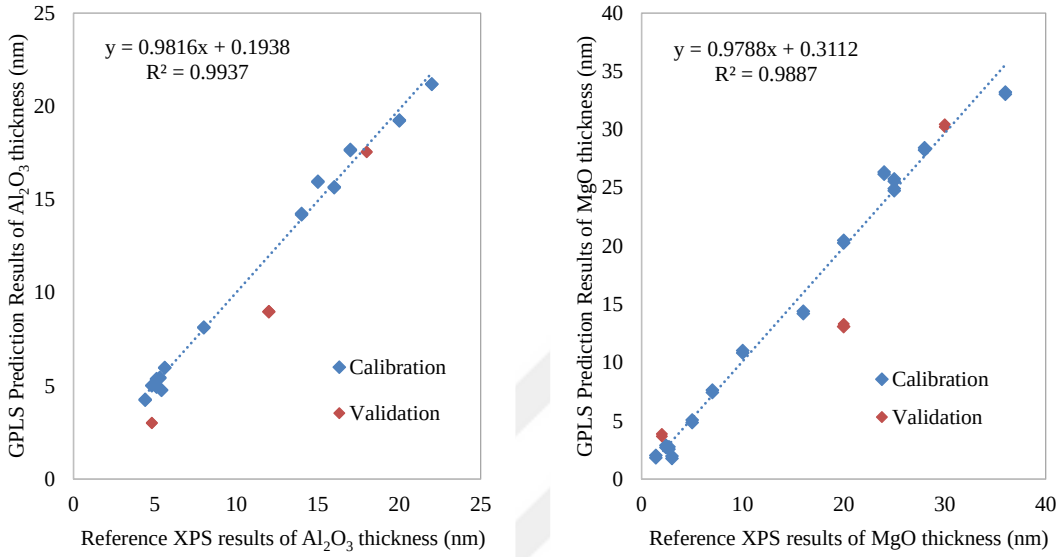

Figure 5.63. Reference XPS results of Al_2O_3 and MgO vs GPLS predicted oxide thickness graphs of the 3005 series of aluminum alloys in perpendicular direction.

Table 5.15. Standard error of cross validation (SECV) and standard error of prediction (SEP) of GPLS model along with maximum and minimum oxide thicknesses of 3005 series in perpendicular direction.

	SECV (nm)	SEP (nm)	Max (nm)	Min (nm)
Al_2O_3	0.5	2.1	22.0	4.4
MgO	1.2	4.1	36.0	1.4

While the SECV values of GILS models are lower, somewhat higher SEP values indicate a possible over fit problem as seen in Table 5.13. This results, however, had been improved by using PLS modelling that takes advantages of principal component analysis (PCA) which reduces the dimensionally of the raw spectral data by taking the linear combinations of the original variables in the process of generating PCA score vectors which now has the size of the number of calibration sample.

5.5.1.4. GPLS Results for 3003BZ Series of Aluminum Alloys

The 3003BZ series which had been previously modelled by using SLS and GILS were also modelled using GPLS. Plots of reference oxide thicknesses versus the predictions with GPLS are given in Figure 5.64. Also, standard error of cross-validation and standard error of prediction along with maximum and minimum values of oxide thickness range are given in Table 5.16.

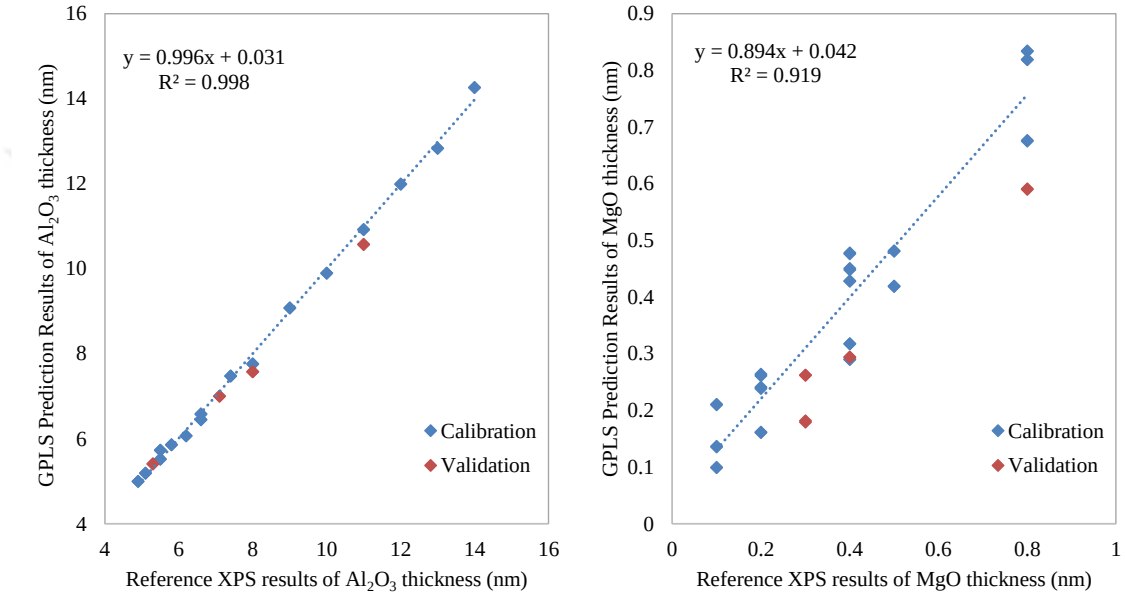

Figure 5.64. Reference XPS results of Al_2O_3 and MgO vs GPLS predicted oxide thickness graphs of the 3003BZ series of aluminum alloys in perpendicular direction.

Table 5.16. Standard error of cross validation (SECV) and standard error of prediction (SEP) of GPLS model along with maximum and minimum oxide thicknesses of 3003BZ series in perpendicular direction.

	SECV (nm)	SEP (nm)	Max (nm)	Min (nm)
Al_2O_3	0.2	0.3	14.0	4.9
MgO	$6.9x10^{-2}$	0.1	0.8	0.1

The constructed GILS and GPLS models for Al_2O_3 thickness of 3003BZ series in perpendicular direction can both be considered successful when the SEP values are taken into account which are 0.5 and 0.3 for GILS and GPLS respectively. On the other hand,

the predicted MgO thickness were not that good, and the low SECV value with a higher SEP values points to an over fitting problem due to the MgO layer being extremely thin.

5.5.2. Parallel Direction Multivariate Calibration Results

After multivariate calibration studies using perpendicular direction measurements of 3005 and 3003BZ series alloys, parallel direction measurements of same aluminum series were used and resulting multivariate calibration modelling studies are shown in following sections.

5.5.2.1. GILS Results for 3005 Series of Aluminum Alloys

Similar to perpendicular direction measurements, XPS results of aluminum and magnesium oxide thicknesses of 3005 series alloys given in Table 5.1 and 5.2 were used and 14 out of 17 samples and un-annealed sample were used to construct calibration model while the remaining 3 samples were used to construct independent validation set. GILS modelling studies were built with baseline corrected GATR-FTIR spectra belongs to 3005 series of aluminum alloys in parallel direction given in Figure 5.42. XPS reference aluminum and magnesium oxide thicknesses and their corresponding GILS oxide predictions are given in Figure 5.65. Standard error of cross-validation (SECV) and standard error of prediction (SEP) along with maximum and minimum values of oxide thicknesses are also given in Table 5.17.

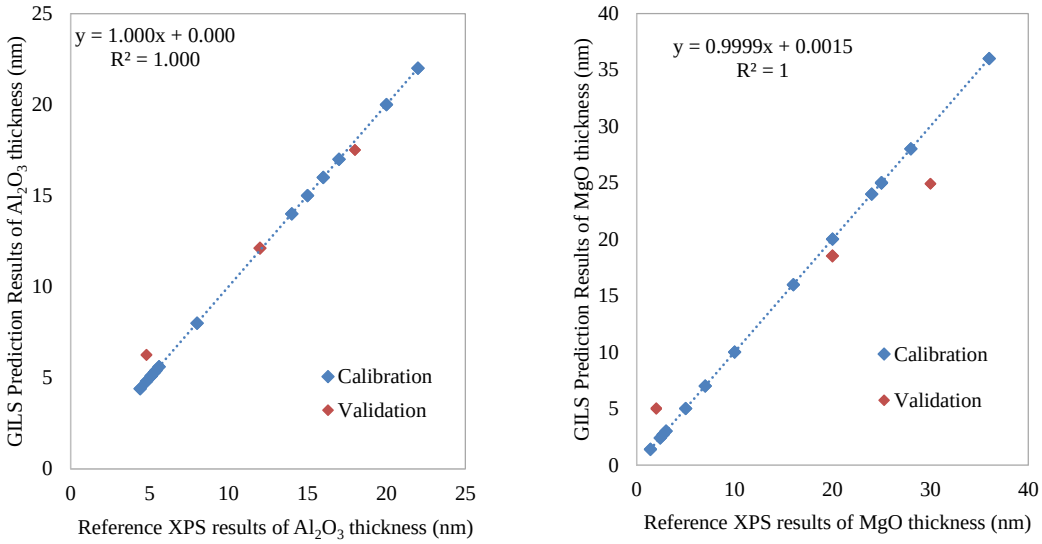

Figure 5.65. Reference XPS results of Al_2O_3 and MgO vs GILS predicted oxide thickness graphs of the 3005 series of aluminum alloys in parallel direction.

Table 5.17. Standard error of cross validation (SECV) and standard error of prediction (SEP) of GILS model along with maximum and minimum oxide thicknesses of 3005 series in parallel direction.

	SECV (nm)	SEP (nm)	Max (nm)	Min (nm)
Al_2O_3	$3.0x10^{-4}$	0.9	22.0	4.4
MgO	$2.0x10^{-2}$	3.5	36.0	1.4

When the success of GILS models for perpendicular and parallel directions are compared, as shown in Figure 5.65, similar over fitting problem is also observed in parallel direction GILS model study for both Al_2O_3 and MgO. However, in terms of standard error of cross validation and prediction values, GILS models in parallel direction assumed to have better results. Standard error of cross validation value is found as 0.0003 and standard error of prediction value is found as 0.9 for Al_2O_3 in parallel direction as shown in Table 5.17, while SECV and SEP values are found as 0.0008 and 2.2, respectively for perpendicular direction. Similarly, SECV and SEP values for MgO GILS model in parallel direction were also found lower than perpendicular direction.

5.5.2.2. GILS Results for 3003BZ Series of Aluminum Alloy

GILS modelling studies were also performed with 3003BZ series alloys in parallel direction. Same XPS reference oxide thicknesses for 3003BZ series which were used in perpendicular direction are used which are shown in Table 5.3 and 5.4. Respective GATR-FTIR spectra belongs to baseline corrected 3003BZ series alloys in parallel direction shown in Figure 5.44 are also used to build GILS models for Al_2O_3 and MgO. Similar to perpendicular direction, 16 out of 20 samples were used to construct calibration sets and the remaining 4 samples were used as an independent validation set in parallel direction studies. Figure 5.66 shows the XPS reference oxide thicknesses of Al_2O_3 and MgO and their corresponding GILS predicted oxide thicknesses. SECV, SEP, maximum and minimum value of working range for both oxides were also given in Table 5.18.

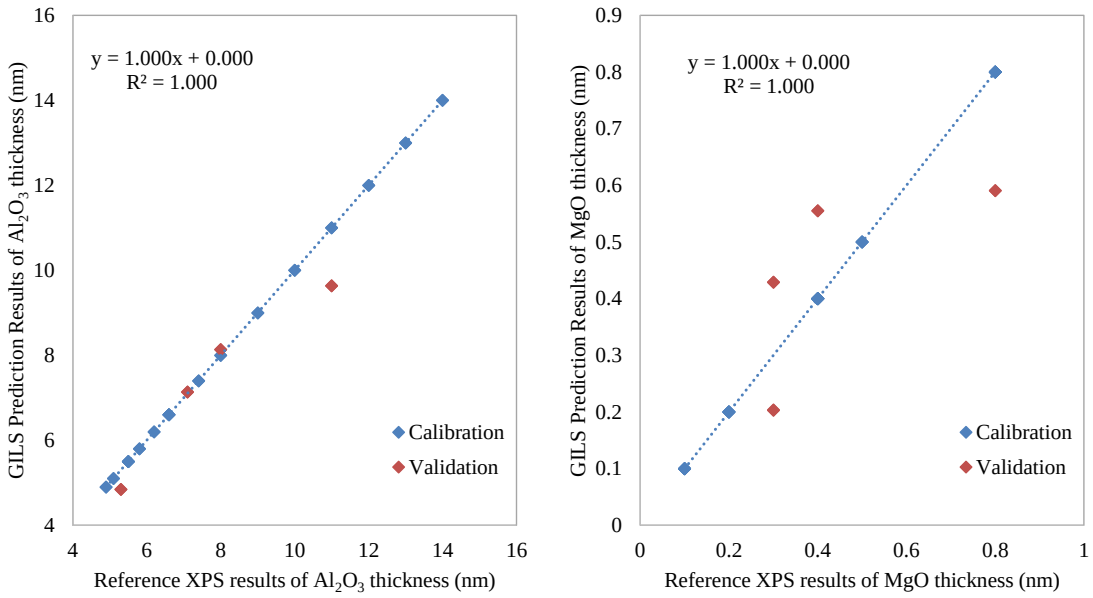

Figure 5.66. Reference XPS results of Al_2O_3 and MgO vs GILS predicted oxide thickness graphs of the 3003BZ series of aluminum alloys in parallel direction.

Table 5.18. Standard error of cross validation (SECV) and standard error of prediction (SEP) of GILS model along with maximum and minimum oxide thicknesses of 3003BZ series in parallel direction.

	SECV (nm)	SEP (nm)	Max (nm)	Min (nm)
Al_2O_3	$1x10^{-3}$	0.7	14.0	4.9
MgO	$1x10^{-3}$	0.2	0.8	0.1

As shown in Figure 5.66, similar to perpendicular direction, although GILS models for both Al_2O_3 and MgO are able to build a successful model, they are not sufficient enough to predict independent validation set which results in over fitting problem. However, when SECV and SEP values for both Al_2O_3 and MgO shown in Table 5.18 are compared with perpendicular direction results, parallel direction GILS modelling studies have lower calibration errors while prediction errors are higher than perpendicular direction.

5.5.2.3. GPLS Results for 3005 Series of Aluminum Alloys

3005 series of aluminum alloys which have already used to construct GILS model also used to construct GPLS model in parallel direction. Similar to all of the 3005 series modelling studies, same number of aluminum alloys were used to construct calibration and independent validation set. Resulting XPS reference Al_2O_3 and MgO thicknesses vs GPLS prediction results are shown in Figure 5.67. Standard error of cross validation, standard error of prediction, maximum and minimum of working range are given in Table 5.19.

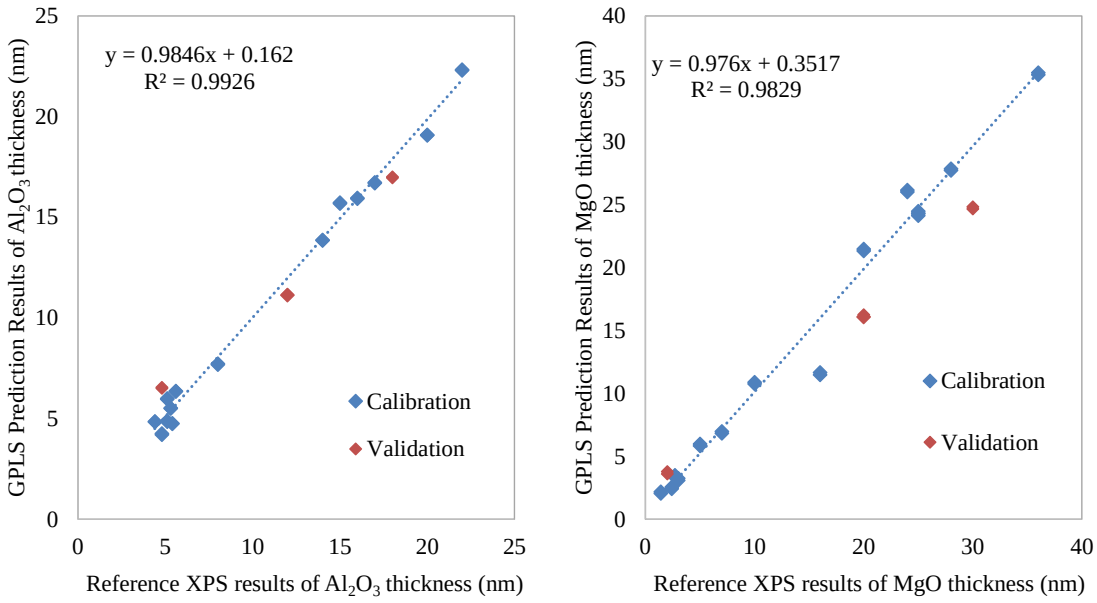

Figure 5.67. Reference XPS results of Al_2O_3 and MgO vs GPLS predicted oxide thickness graphs of the 3005 series of aluminum alloys in parallel direction.

Table 5.19. Standard error of cross validation (SECV) and standard error of prediction (SEP) of GPLS model along with maximum and minimum oxide thicknesses of 3005 series in parallel direction.

	SECV (nm)	SEP (nm)	Max (nm)	Min (nm)
Al_2O_3	0.6	1.3	22.0	4.4
MgO	1.5	3.9	36.0	1.4

As shown in Figure 5.67, similar to perpendicular direction, GPLS models for Al_2O_3 and MgO in parallel direction overcome the overfitting problem which had been observed in GILS models. However, SEP values are still observed to be higher than the SECV values which could be the result of low number of samples used to build models shown in Table 5.19.

5.5.2.4. GPLS Results for 3003BZ Series of Aluminum Alloys

The last GPLS modelling study was performed with 3003BZ series of aluminum alloys in parallel direction. Same number of aluminum alloys which have been already used to construct calibration and independent validation set were used and resulting XPS reference oxide thicknesses and GPLS prediction results of both Al_2O_3 and MgO are given in Figure 5.68. SECV and SEP values along with maximum and minimum values of working range are also given in Table 5.20.

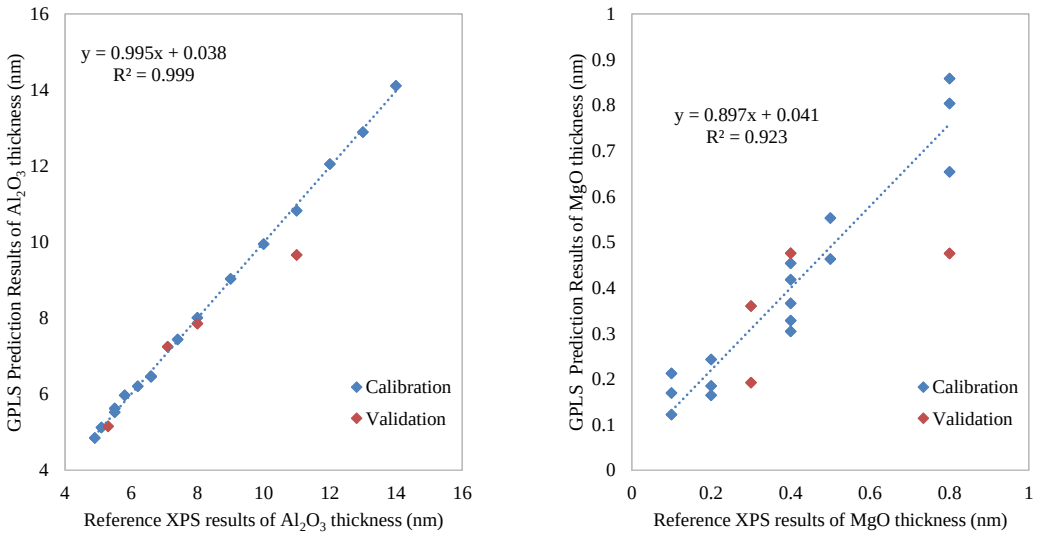

Figure 5.68. Reference XPS results of Al_2O_3 and MgO vs GPLS predicted oxide thickness graphs of the 3003BZ series of aluminum alloys in parallel direction.

Table 5.20. Standard error of cross validation (SECV) and standard error of prediction (SEP) of GPLS model along with maximum and minimum oxide thicknesses of 3003BZ series in parallel direction.

	SECV (nm)	SEP (nm)	Max (nm)	Min (nm)
Al_2O_3	0.1	0.7	14.0	4.9
MgO	0.1	0.2	0.8	0.1

Comparison of GILS and GPLS models obtained from parallel direction measurements for 3003BZ series indicated that SEP values are observed to be higher than SECV values in both cases. In addition to these, as shown in Figure 5.68, over fitting problem was eliminated in GPLS models. As it is mentioned, the 3003BZ series do not have additional magnesium content, the predictive power of all the MgO models were not as good as Al_2O_3 models. However, resulting modelling studies can still assumed to be successful when the working range of MgO thickness considered.

After all modelling studies were obtained, as it was mentioned before, several aluminum alloys which resembles to 3005 and 3003BZ series and have no XPS reference data were studied. As shown in FTIR result section, by using the respective FTIR spectra, oxide thicknesses of these mentioned aluminum alloys were predicted and perpendicular and parallel direction model studies were compared in following section.

5.5.3. Comparison of Perpendicular and Parallel Direction Measurements

To be able to determine to most successful models, perpendicular and parallel models were used to predict the oxide thicknesses of 3105, 5005, 5052 and 5754 series alloys by using corresponding 3005 series models. Similarly, oxide thicknesses of 1050, 3003, 8006 and 8156 series alloys were predicted with corresponding 3003BZ series models. In following section, perpendicular and parallel measurements were compared with their respective multivariate calibration models.

5.5.3.1. Comparison of GILS predicted Al_2O_3 thickness of 3005 like alloys Perpendicular and Parallel Measurements

First comparison of perpendicular and parallel direction measurement were studied with 3005 GILS model. The predicted Al_2O_3 thicknesses of namely 3105, 5005, 5052 and 5754 series alloys were used to compare perpendicular and parallel direction models. Figure 5.69 shows the comparison of predicted Al_2O_3 thicknesses belongs to these mentioned series. The x-axis figure labels indicate the alloy series name, annealing temperature and annealing time with spaces between each term (e.g. '3105'-'200 ^{o}C'-'1h' corresponds to the samples which is from 3105 series of aluminum alloy annealed at 200 ^{o}C for 1 hour).

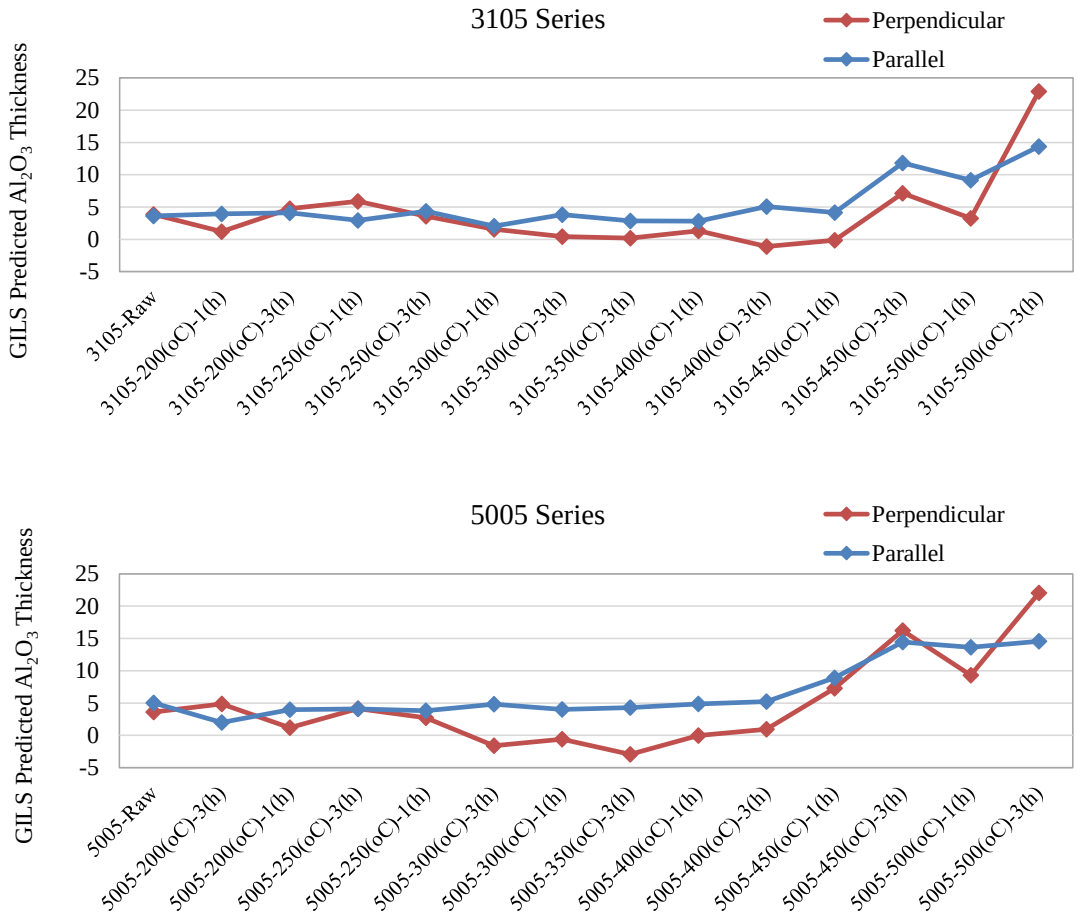

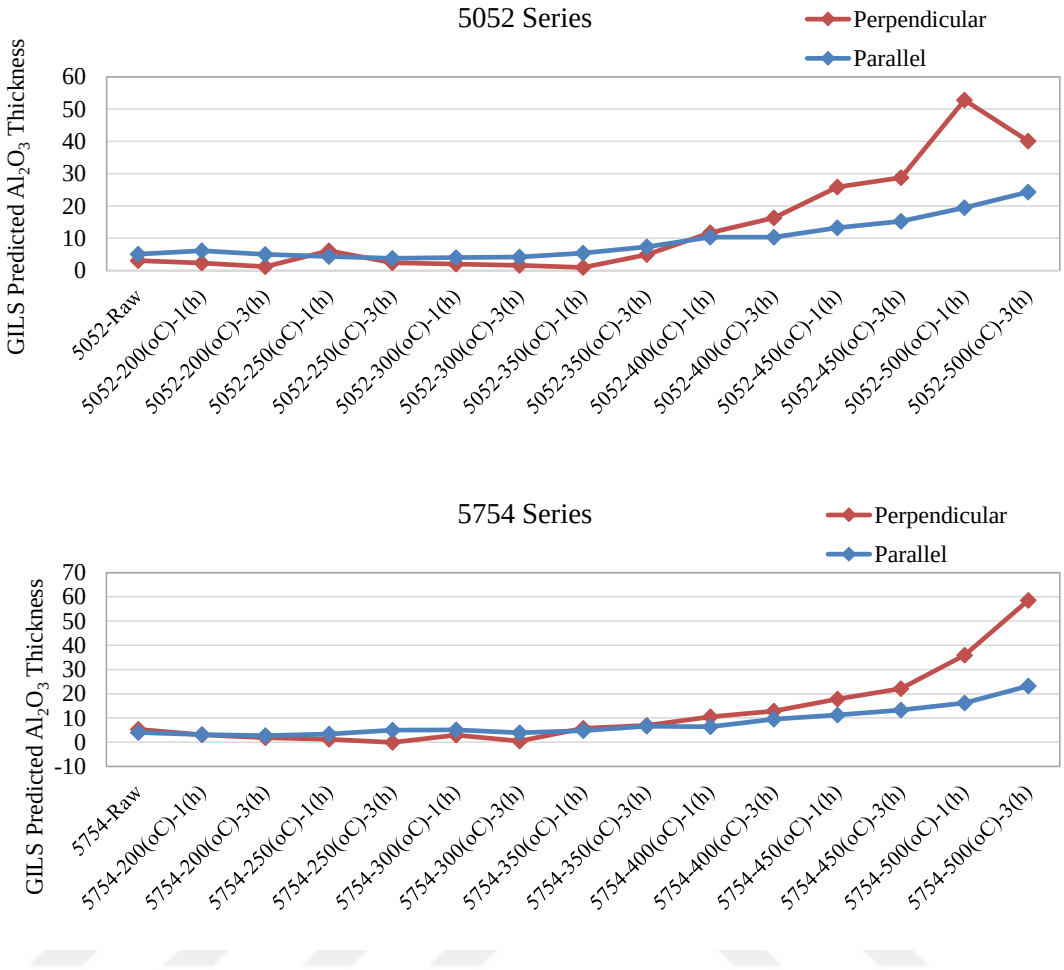

Figure 5.69. Comparison of predicted Al_2O_3 thickness of five different series of alloys (3105, 5005, 5052 and 5754) using perpendicular and parallel 3005 GILS models.

In the predicted aluminum oxide graphs in Figure 5.69, x-axis represents the increasing annealing temperature and annealing time. Therefore, predicted oxide thicknesses are expected to increase when going to the right in the x axis. However, when the predicted oxide thicknesses in perpendicular direction of 3105 and 5005 series of aluminum are examined, negative values are observed and these predictions have higher fluctuations than parallel direction predictions. Also, in the case of 5052 and 5754 series of alloy predictions, parallel and perpendicular direction models are observed to follow the same trend up to 400°C. However, the Al_2O_3 thickness in perpendicular direction predictions are observed up to 60 nm in the highest annealing temperature and time, which is not reasonable. The other point is, the composition of 5052 and 5754 series alloys are known to be much similar to 3005 series which was modelled. Since the predictions of Al_2O_3 thicknesses are expected to show an oxide thickness trend that is similar with 3005

series, GILS models for 3005 series in parallel direction can be assumed to have better models for Al_2O_3 thickness predictions of unknown samples.

5.5.3.2. Comparison of GILS predicted MgO thickness of 3005 like alloys Perpendicular and Parallel Measurements

GILS models constructed with 3005 series alloys were also used to predict MgO thicknesses of 3105, 5005, 5052 and 5754 series alloys. To be able to compare perpendicular and parallel direction GILS modelling studies, predicted MgO thicknesses belongs to those mentioned four series alloys are given in the Figure 5.70.

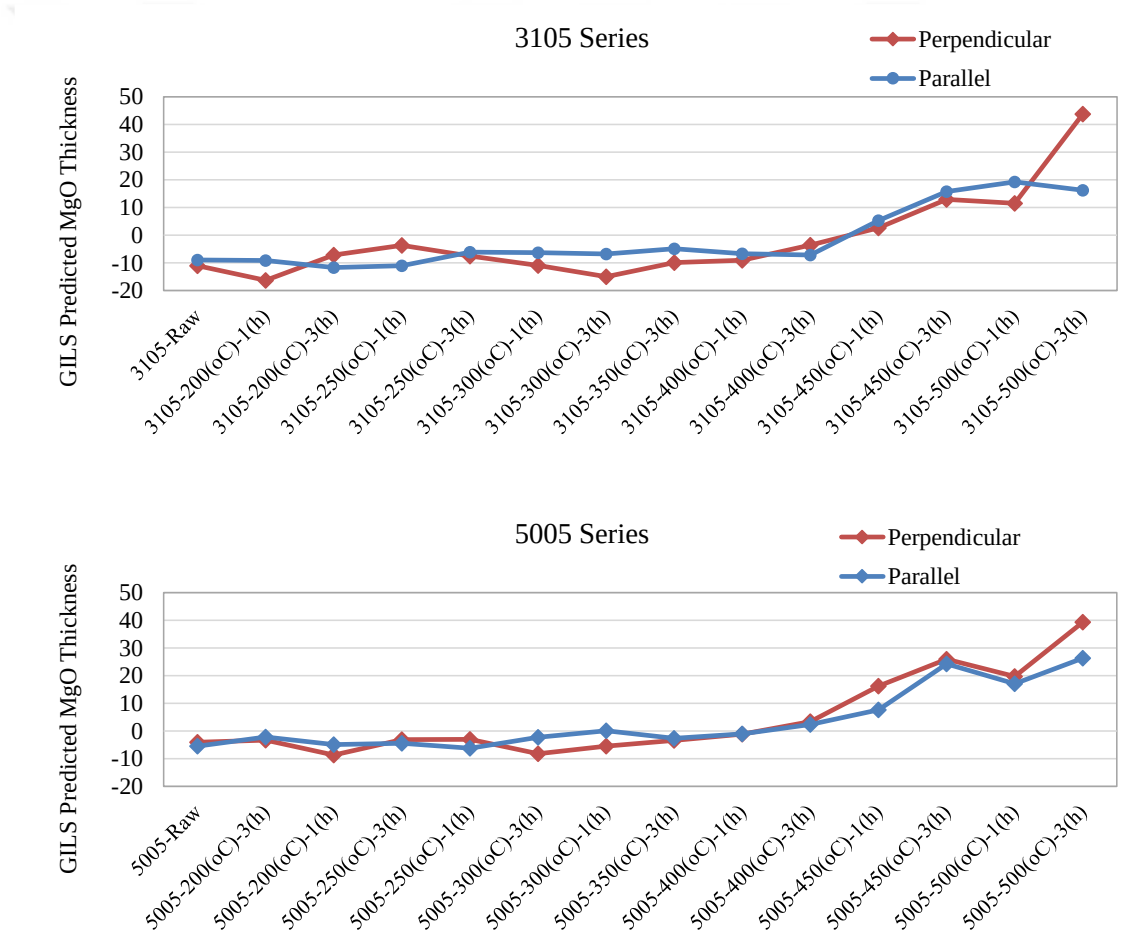

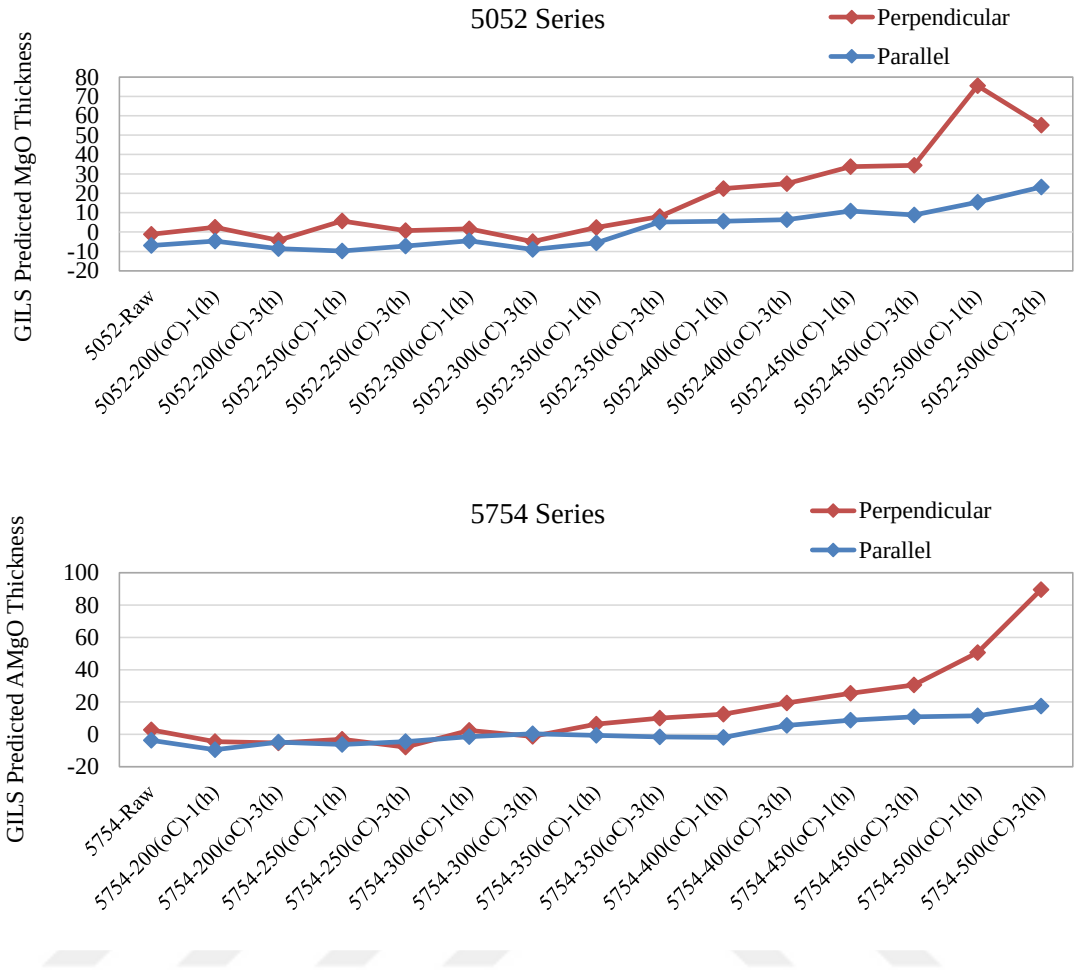

Figure 5.70. Comparison of predicted MgO thickness of five different series of alloys (3105, 5005, 5052 and 5754) using perpendicular and parallel 3005 GILS models.

Comparison of GILS predicted MgO thicknesses of 3105, 5005, 5052 and 5754 series alloys shown in Figure 5.70 indicated that even though predicted MgO thicknesses are observed in negative values in perpendicular and parallel measurement models, parallel direction measurements resulted in somewhat better predictions especially in 5052 and 5754 series alloys.

5.5.3.3. Comparison of GPLS predicted Al_2O_3 thickness of 3005 like alloys Perpendicular and Parallel Measurements

Aluminum oxide thicknesses of same aluminum alloys predicted by using 3005 GILS models were also predicted by using 3005 GPLS models. Predicted aluminum oxide thicknesses of 3105, 5005, 5052 and 5754 series alloy are given in Figure 5.71.

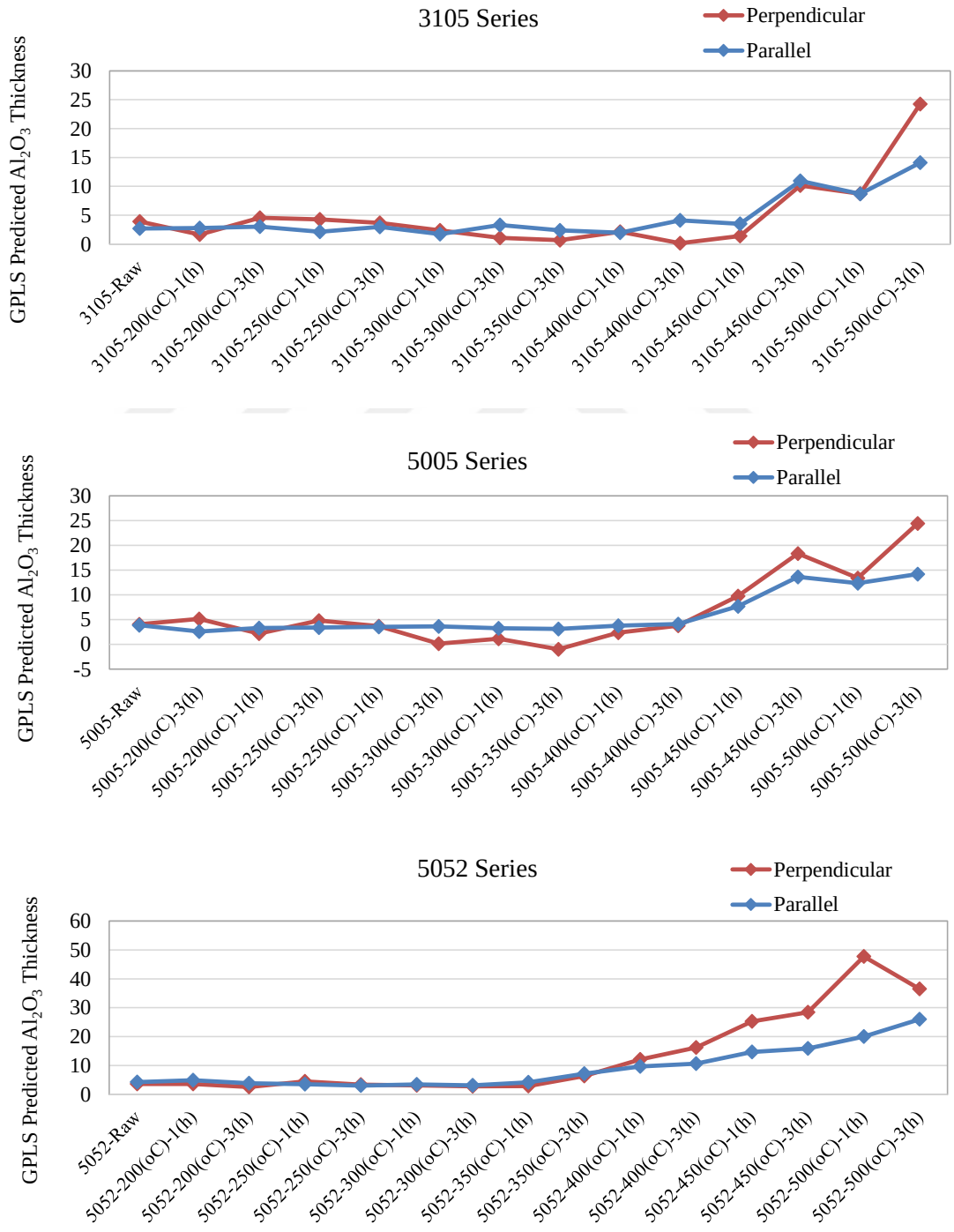

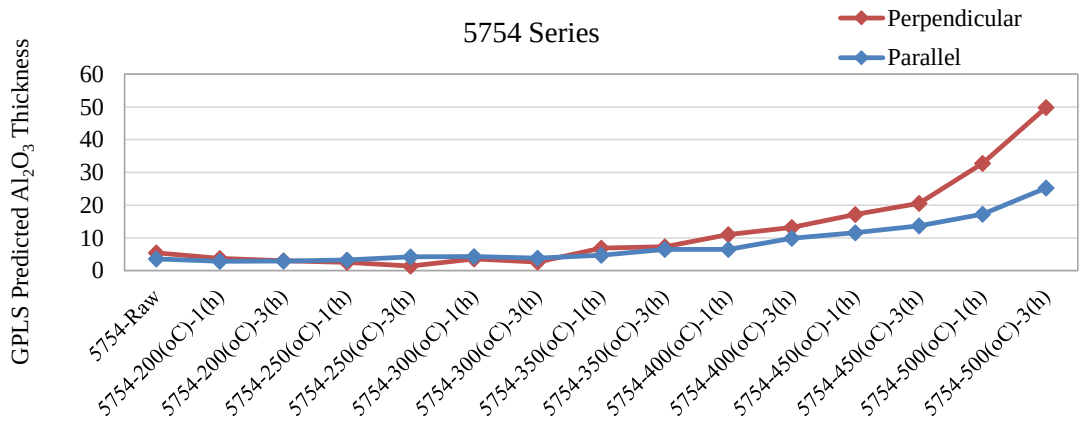

Figure 5.71. Comparison of predicted Al_2O_3 thickness of five different series of alloys (3105, 5005, 5052 and 5754) using perpendicular and parallel 3005 GPLS models.

As seen in predictions of 3105 and 5005 series, while the oxide thicknesses follows a consistent trend in parallel measurements, the perpendicular measurements resulted in somewhat fluctuated predictions. Also, in 5052 and 5754 series, predicted oxide thicknesses reaches to an unexpected value for perpendicular measurements whereas the predictions of parallel measurements remained reasonable.

5.5.3.4. Comparison of GPLS predicted MgO thickness of 3005 like alloys Perpendicular and Parallel Measurements

For 3005 series, the last comparison of perpendicular and parallel measurements were carried out for predictions of MgO thicknesses. The magnesium oxide thicknesses of same four series of aluminum alloys were predicted by 3005 GPLS models and resulting graphs are given in Figure 5.72.

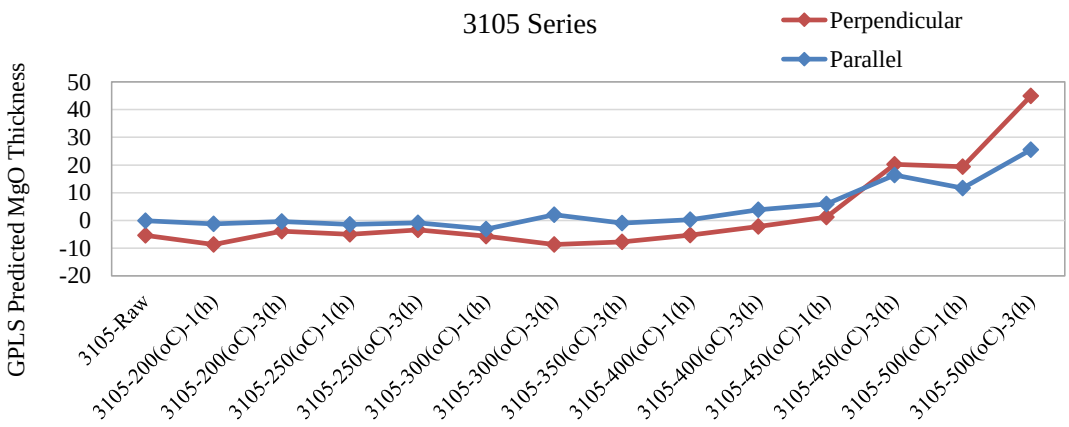
3105 Series
Perpendicular
Parallel
GPLS Predicted MgO Thickness
50
40
30
20
10
0
-10
-20
3105-Raw
3105-200(oC)-1(h)
3105-200(oC)-3(h)
3105-250(oC)-1(h)
3105-250(oC)-3(h)
3105-300(oC)-1(h)
3105-300(oC)-3(h)
3105-350(oC)-3(h)
3105-400(oC)-1(h)
3105-400(oC)-3(h)
3105-450(oC)-1(h)
3105-450(oC)-3(h)
3105-500(oC)-1(h)
3105-500(oC)-3(h)

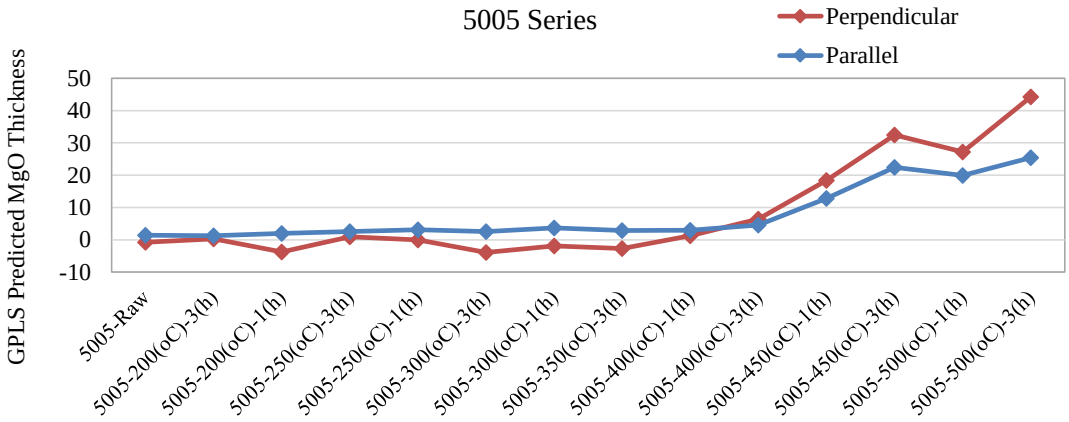
5005 Series
Perpendicular
Parallel
GPLS Predicted MgO Thickness
50
40
30
20
10
0
-10
5005-Raw
5005-200(oC)-3(h)
5005-200(oC)-1(h)
5005-250(oC)-3(h)
5005-250(oC)-1(h)
5005-300(oC)-3(h)
5005-300(oC)-1(h)
5005-350(oC)-3(h)
5005-400(oC)-1(h)
5005-400(oC)-3(h)
5005-450(oC)-1(h)
5005-450(oC)-3(h)
5005-500(oC)-1(h)
5005-500(oC)-3(h)

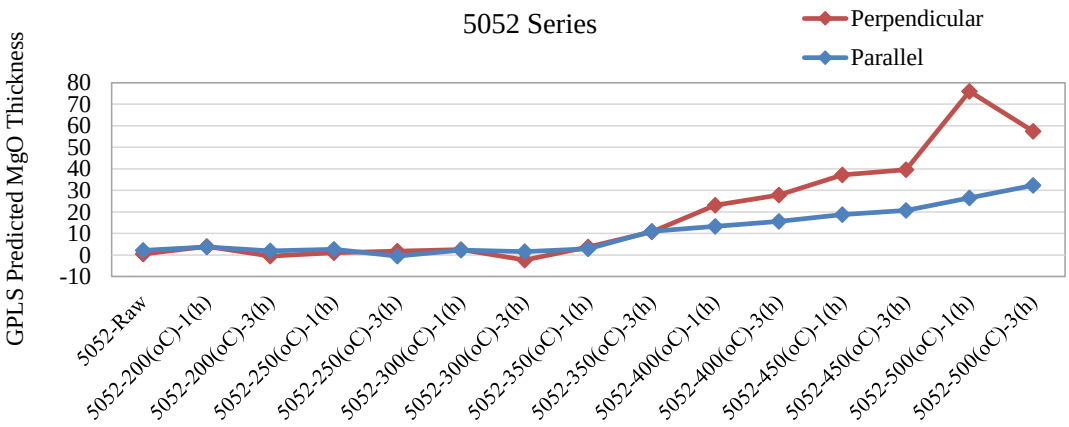
5052 Series
Perpendicular
Parallel
GPLS Predicted MgO Thickness
80
70
60
50
40
30
20
10
0
-10
5052-Raw
5052-200(oC)-1(h)
5052-200(oC)-3(h)
5052-250(oC)-1(h)
5052-250(oC)-3(h)
5052-300(oC)-1(h)
5052-300(oC)-3(h)
5052-350(oC)-1(h)
5052-350(oC)-3(h)
5052-400(oC)-1(h)
5052-400(oC)-3(h)
5052-450(oC)-1(h)
5052-450(oC)-3(h)
5052-500(oC)-1(h)
5052-500(oC)-3(h)

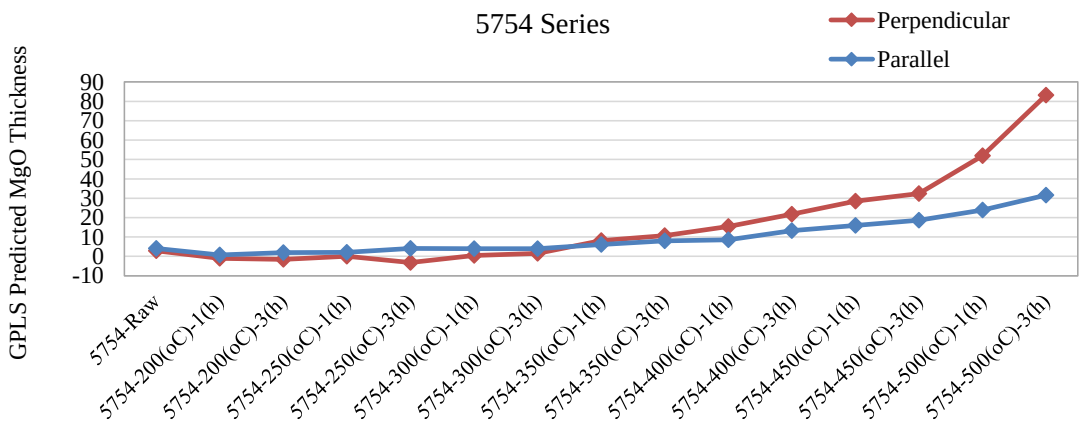

Figure 5.72. Comparison of predicted MgO thickness of five different series of alloys (3105, 5005, 5052 and 5754) using perpendicular and parallel 3005 GPLS models.

While the predictions for both parallel and perpendicular measurements follows the same trend until 350^{o}C, the perpendicular measurements often goes below zero which indicates weakness in the reliability of these models whereas in the parallel measurements this problem does not exist for 3105 and 5005 series alloys. Another problem is the unexpectedly high oxide thickness predictions after 350^{o}C for perpendicular measurements especially in 5052 and 5754 series alloys. Finally, the fluctuations are more dramatic in 5005 and 5052 series alloys in perpendicular measurements.

After all comparisons carried out with 3005 GILS and GPLS models, for the determination of aluminum oxide and magnesium oxide thicknesses multivariate calibration models constructed with parallel measurement were chosen since it is more reliable in most cases. To be able to determine the best calibration method, comparison of predictions from both univariate and multivariate models are reported after the comparison of perpendicular and parallel measurements for 3003BZ series which are given in following section.

5.5.3.5. Comparison of GILS predicted Al_2O_3 thickness of 3003BZ like alloys Perpendicular and Parallel Measurements

As it was mentioned in experimental section, four different series of alloys namely 1050, 3003, 8006 and 8156 aluminum alloys having FTIR spectral resemblance because of the composition similarity were chosen to compare perpendicular and parallel measurement of 3003BZ GILS models. Figure 5.73 shows the GILS predicted Al_2O_3 thicknesses belongs to those mentioned series of alloys.

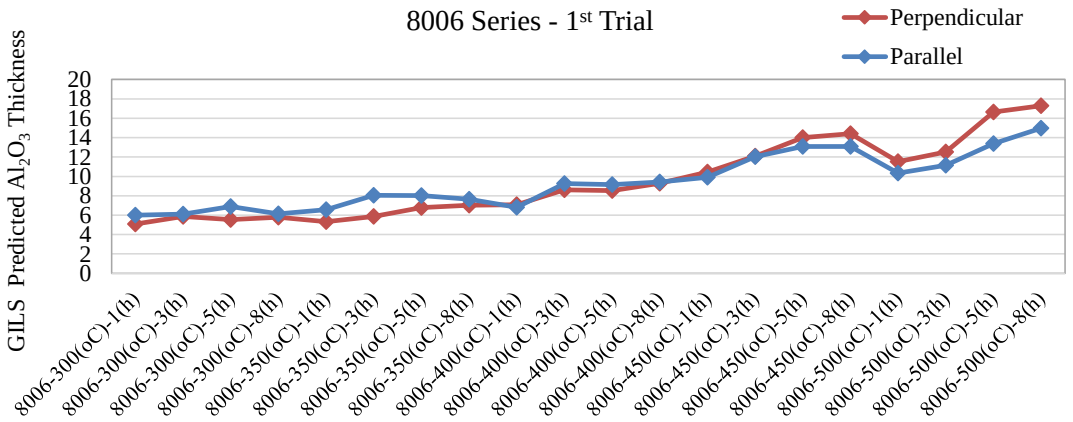

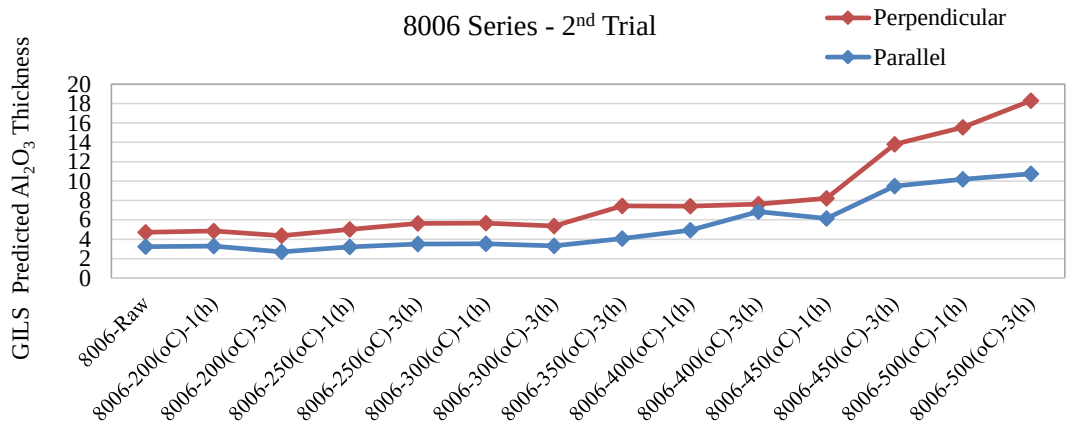

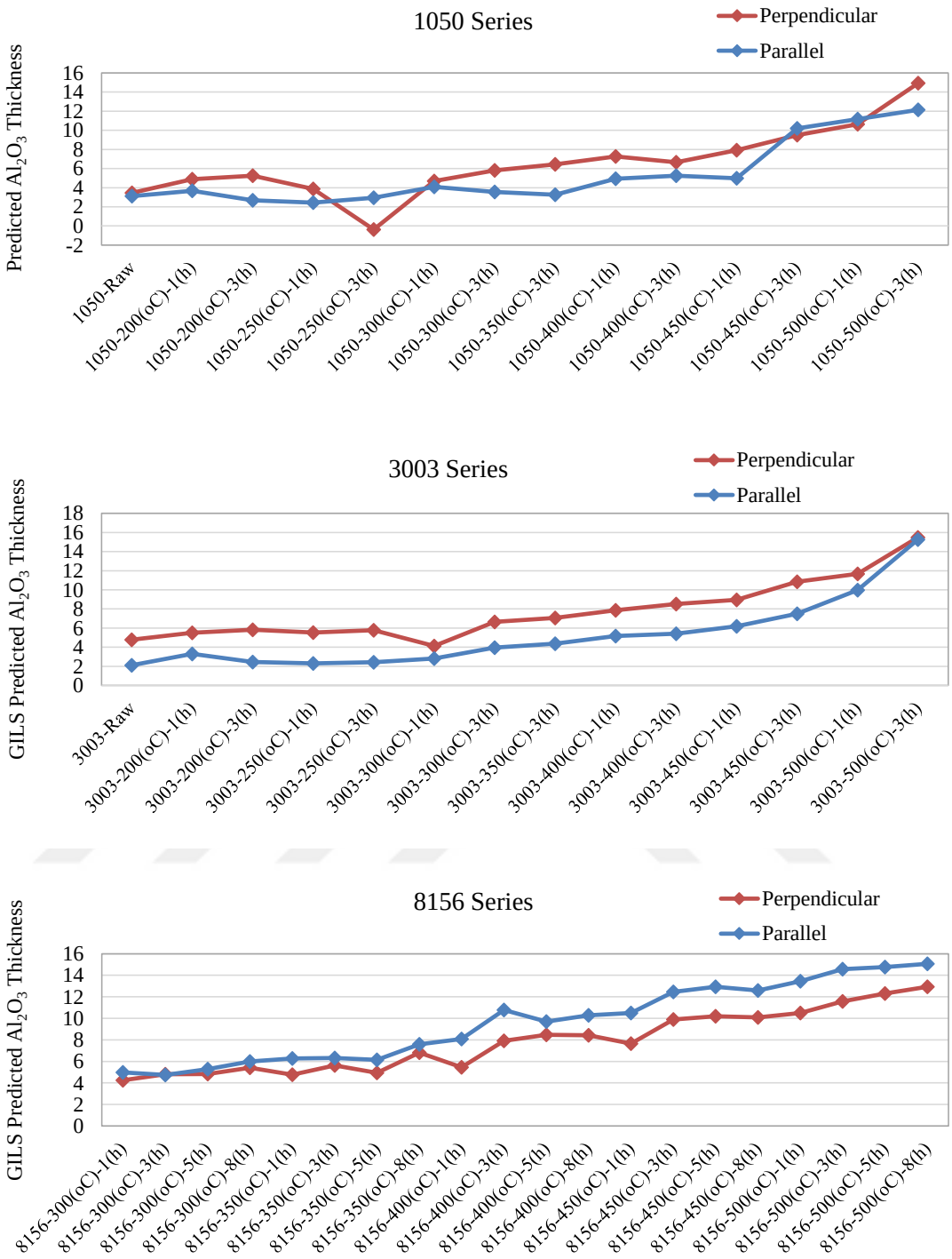

Figure 5.73. Comparison of predicted Al_2O_3 thickness of four different series of alloys (8006-1st Trial, 8006-2nd Trial, 1050, 3003 and 8156) using perpendicular and parallel 3003BZ GILS models.

As shown in Figure 5.73, there are two 8006 series. FTIR spectra of one of them measured as a first trial set and the other measurement were carried out as a second trial. While the predictions of first trial of 8006 series shows a very similar trend for parallel and perpendicular measurements, in the predictions of second trial of 8006 series as well as 1050 and 3003 series alloys positive bias is observed for perpendicular measurements. Also, there is a significant fluctuation in the prediction of perpendicular measurements in 1050 series, and a slight fluctuation in 3003 series. In the prediction of 8156 series alloys, however, even though the parallel measurements appear to cause positive biased predictions, the results of parallel measurements appears to be better in agreement with the XPS reference Al_2O_3 thicknesses of 3003BZ series shown in Table 5.3.

5.5.3.6. Comparison of GILS predicted MgO thickness of 3003BZ like alloys Perpendicular and Parallel Measurements

The MgO thicknesses of same four different series aluminum alloys were also predicted by using respective 3003BZ GILS models. Figure 5.74 shows the predicted MgO thicknesses of 8006-1st Trial, 8006-2nd Trial, 1050, 3003 and 8156 series alloys in perpendicular and parallel measurements.

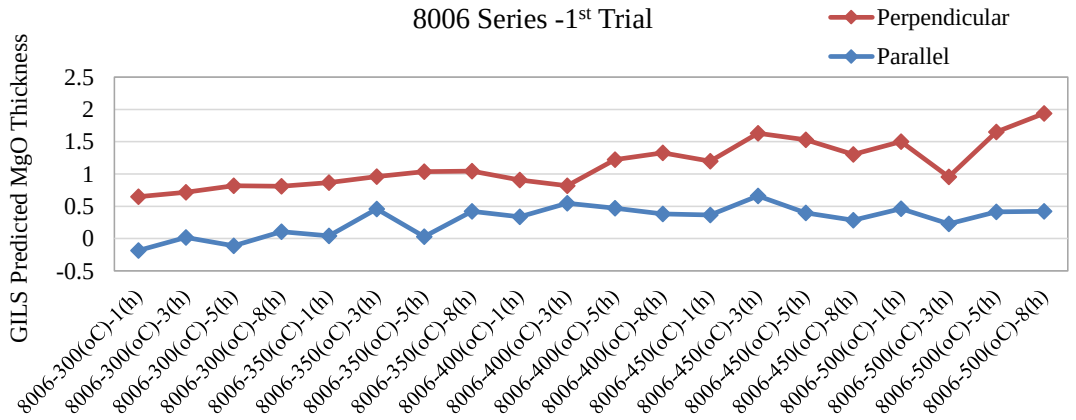

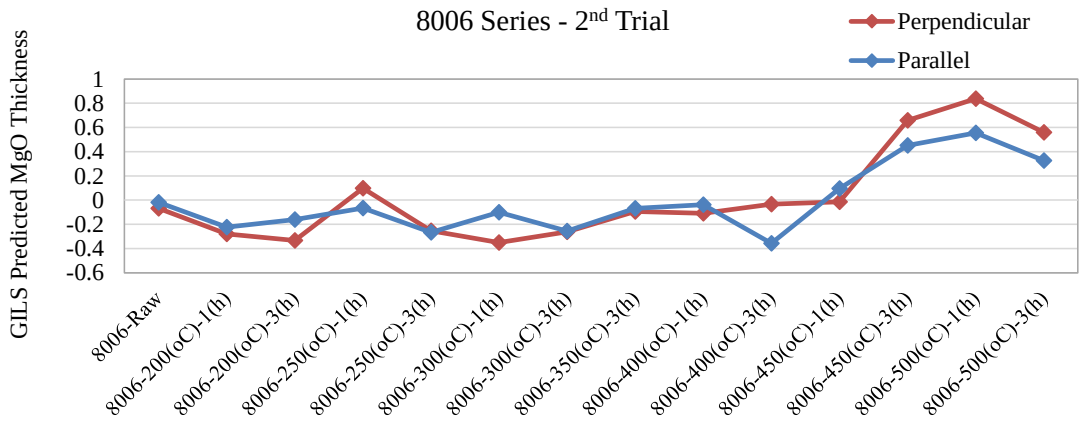
8006 Series - 2nd Trial
Perpendicular
Parallel
GILS Predicted MgO Thickness
1
0.8
0.6
0.4
0.2
0
-0.2
-0.4
-0.6
8006-Raw
8006-200(oC)-1(h)
8006-200(oC)-3(h)
8006-250(oC)-1(h)
8006-250(oC)-3(h)
8006-300(oC)-1(h)
8006-300(oC)-3(h)
8006-350(oC)-3(h)
8006-400(oC)-1(h)
8006-400(oC)-3(h)
8006-450(oC)-1(h)
8006-450(oC)-3(h)
8006-500(oC)-1(h)
8006-500(oC)-3(h)

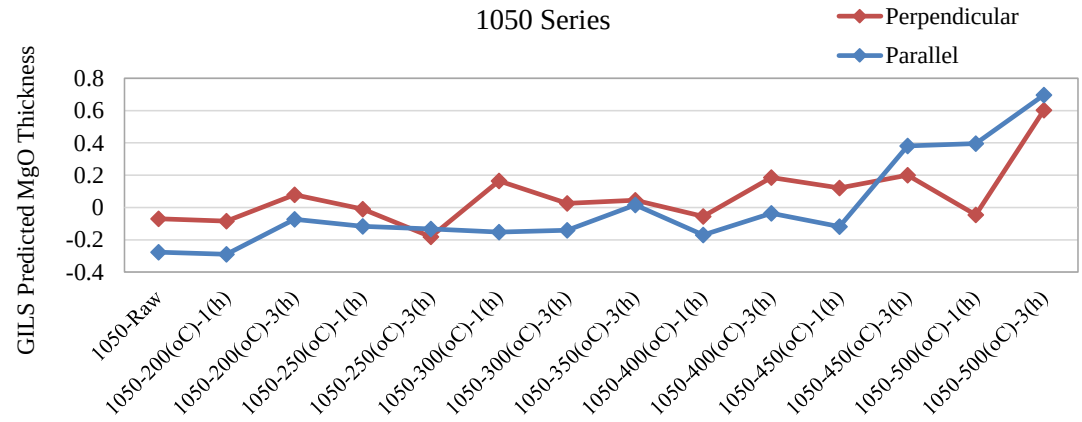
1050 Series
Perpendicular
Parallel
GILS Predicted MgO Thickness
0.8
0.6
0.4
0.2
0
-0.2
-0.4
1050-Raw
1050-200(oC)-1(h)
1050-200(oC)-3(h)
1050-250(oC)-1(h)
1050-250(oC)-3(h)
1050-300(oC)-1(h)
1050-300(oC)-3(h)
1050-350(oC)-3(h)
1050-400(oC)-1(h)
1050-400(oC)-3(h)
1050-450(oC)-1(h)
1050-450(oC)-3(h)
1050-500(oC)-1(h)
1050-500(oC)-3(h)

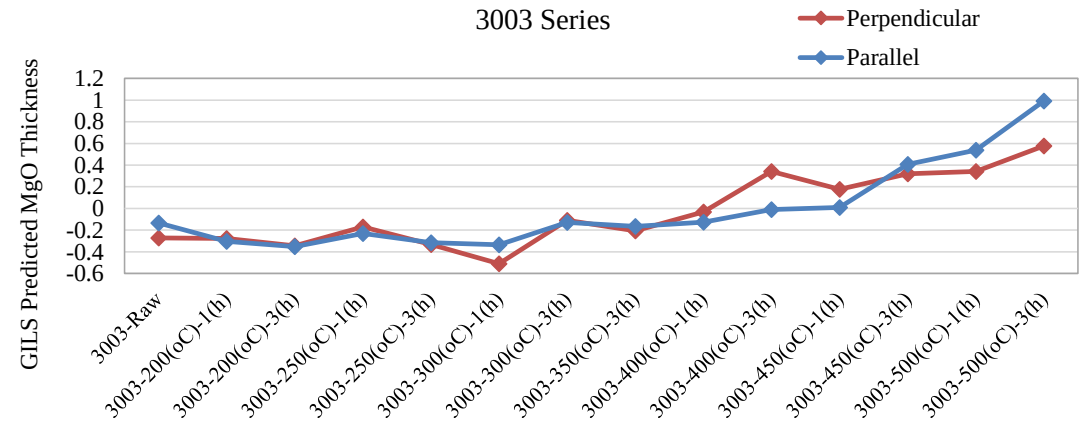
3003 Series
Perpendicular
Parallel
GILS Predicted MgO Thickness
1.2
1
0.8
0.6
0.4
0.2
0
-0.2
-0.4
-0.6
3003-Raw
3003-200(oC)-1(h)
3003-200(oC)-3(h)
3003-250(oC)-1(h)
3003-250(oC)-3(h)
3003-300(oC)-1(h)
3003-300(oC)-3(h)
3003-350(oC)-3(h)
3003-400(oC)-1(h)
3003-400(oC)-3(h)
3003-450(oC)-1(h)
3003-450(oC)-3(h)
3003-500(oC)-1(h)
3003-500(oC)-3(h)

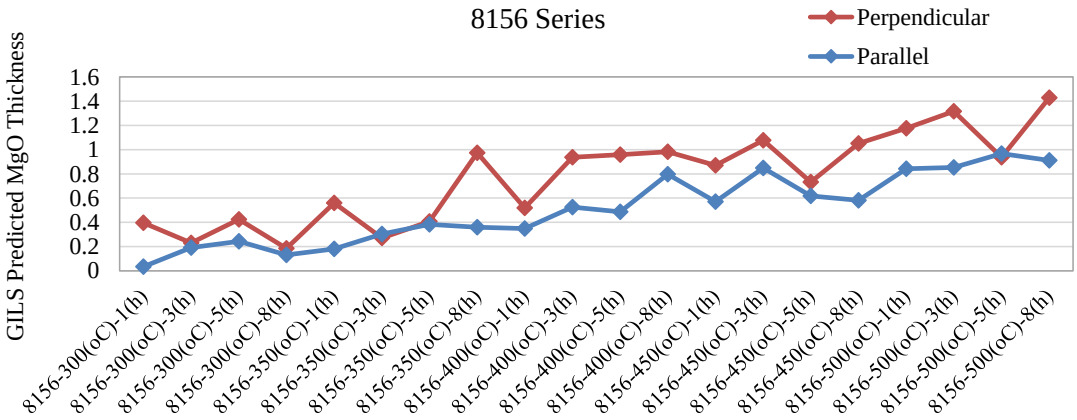

Figure 5.74. Comparison of predicted MgO thickness of five different series of alloys (8006-1st Trial, 8006-2nd Trial, 1050, 3003 and 8156) using perpendicular and parallel 3003BZ GILS models.

Even though the constructed models are already not reliable due to the very small magnesium oxide thicknesses as mentioned in previous sections for the independent validation sets, in the figure showing the predicted MgO thicknesses of the first trial of 8006 and 8156 series alloys, the perpendicular measurements led to the values exceeding 1.0 nm which seems somewhat unlikely as the reference XPS results of 3003BZ series alloy never goes above this value. As a result, the results of parallel measurements appears to be more consistent. In 1050 series alloys, the fluctuations are more evident for perpendicular measurements while the parallel measurements led to more stable predictions. In addition, the predictions of second trial of 8006 series and 3003 series show similar and reasonable trends for both parallel and perpendicular measurements.

5.5.3.7. Comparison of GPLS predicted Al_2O_3 thickness of 3003BZ like alloys Perpendicular and Parallel Measurements

After 3003BZ GILS models, 3003BZ GPLS models were used in order to determine whether perpendicular or parallel measurement oxide predictions are better. For this purpose, same four series of aluminum alloys, which had been already studied with models generated by using 3003BZ data, were used. Figure 5.75 shows the predicted Al_2O_3 thicknesses of 8006-1st Trial, 8006-2nd Trial, 1050, 3003 and 8156 series alloys in both directions.

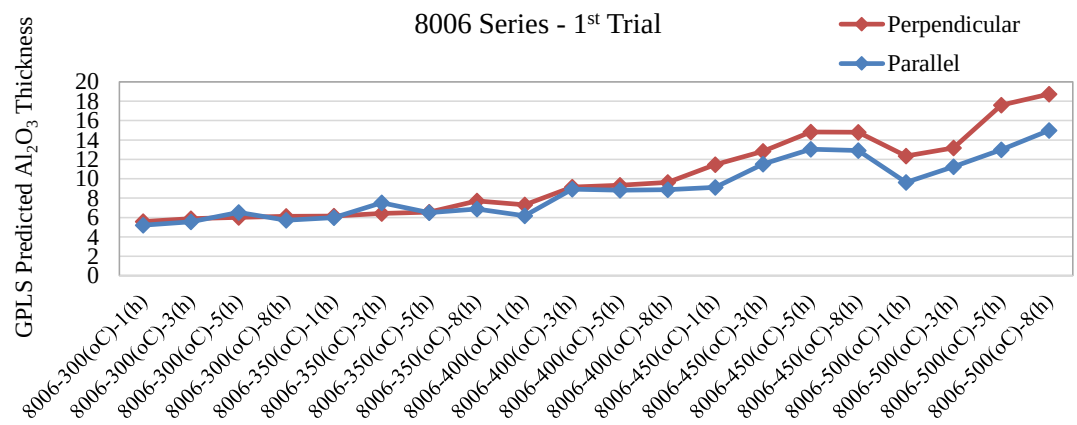
8006 Series - 1st Trial
Perpendicular
Parallel
GPLS Predicted Al2O3 Thickness
0
2
4
6
8
10
12
14
16
18
20
8006-300(oC)-1(h)
8006-300(oC)-3(h)
8006-300(oC)-5(h)
8006-300(oC)-8(h)
8006-350(oC)-1(h)
8006-350(oC)-3(h)
8006-350(oC)-5(h)
8006-350(oC)-8(h)
8006-400(oC)-1(h)
8006-400(oC)-3(h)
8006-400(oC)-5(h)
8006-400(oC)-8(h)
8006-450(oC)-1(h)
8006-450(oC)-3(h)
8006-450(oC)-5(h)
8006-450(oC)-8(h)
8006-500(oC)-1(h)
8006-500(oC)-3(h)
8006-500(oC)-5(h)
8006-500(oC)-8(h)

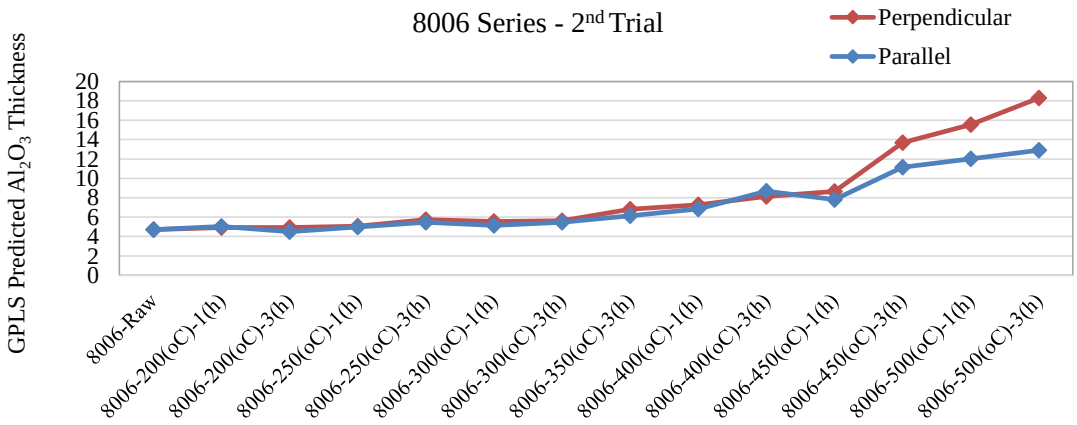
8006 Series - 2nd Trial
Perpendicular
Parallel
GPLS Predicted Al2O3 Thickness
0
2
4
6
8
10
12
14
16
18
20
8006-Raw
8006-200(oC)-1(h)
8006-200(oC)-3(h)
8006-250(oC)-1(h)
8006-250(oC)-3(h)
8006-300(oC)-1(h)
8006-300(oC)-3(h)
8006-350(oC)-3(h)
8006-400(oC)-1(h)
8006-400(oC)-3(h)
8006-450(oC)-1(h)
8006-450(oC)-3(h)
8006-500(oC)-1(h)
8006-500(oC)-3(h)

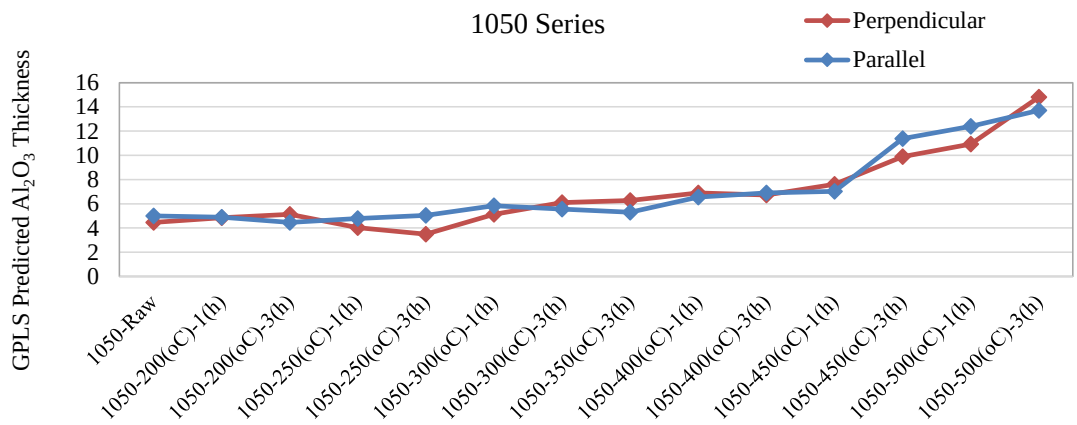
1050 Series
Perpendicular
Parallel
GPLS Predicted Al2O3 Thickness
0
2
4
6
8
10
12
14
16
1050-Raw
1050-200(oC)-1(h)
1050-200(oC)-3(h)
1050-250(oC)-1(h)
1050-250(oC)-3(h)
1050-300(oC)-1(h)
1050-300(oC)-3(h)
1050-350(oC)-3(h)
1050-400(oC)-1(h)
1050-400(oC)-3(h)
1050-450(oC)-1(h)
1050-450(oC)-3(h)
1050-500(oC)-1(h)
1050-500(oC)-3(h)

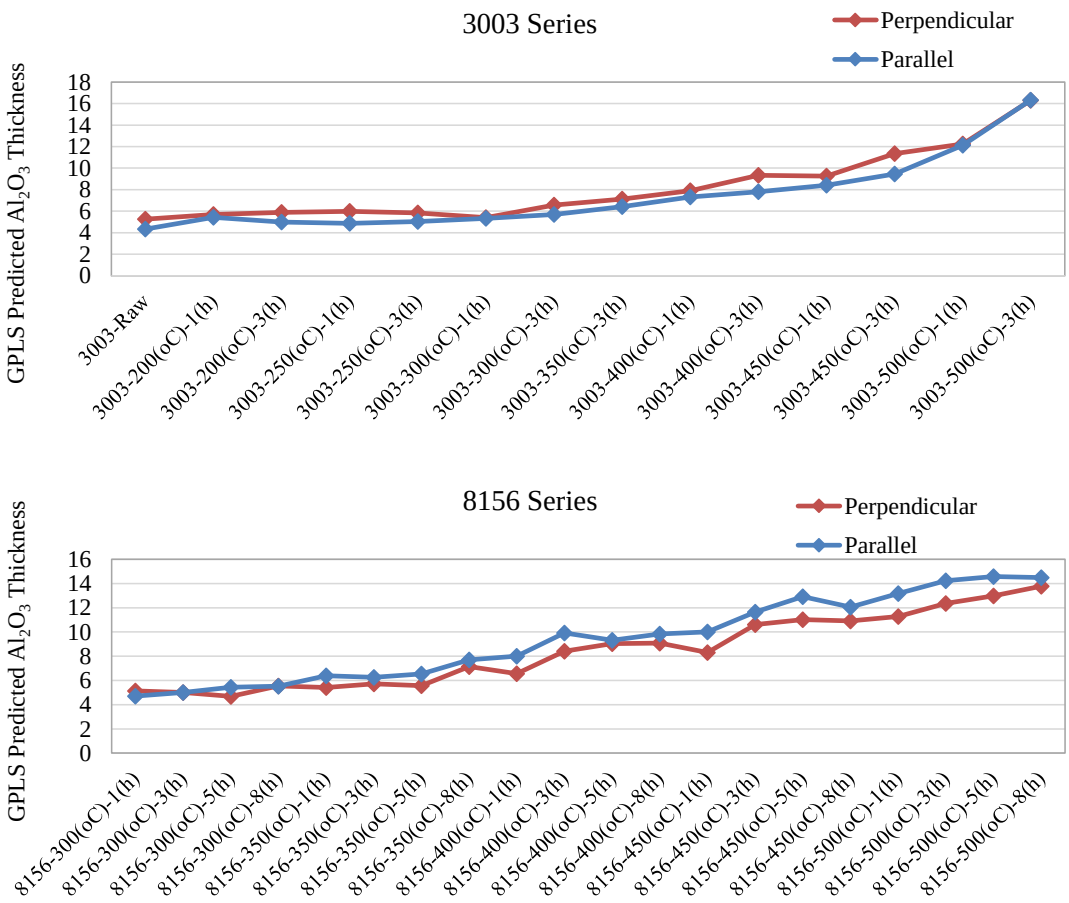

Figure 5.75. Comparison of predicted Al_2O_3 thickness of five different series of alloys (8006-1st Trial, 8006-2nd Trial, 1050, 3003 and 8156) using perpendicular and parallel 3003BZ GPLS models.

As shown in Figure 5.75, although the predictions of 1050, 3003 and 8156 series alloys show very similar trends for both parallel and perpendicular placements, in the predictions of first and second trial of 8006 series a positive deviation after 400ºC and 450ºC was observed for perpendicular measurements respectively.

5.5.3.8. Comparison of GPLS predicted MgO thickness of 3003BZ like alloys Perpendicular and Parallel Measurements

The last comparison of perpendicular and parallel measurement study were carried out with predictions of MgO thicknesses by using 3003BZ series with four different series of 3003BZ series alike aluminum alloys. Figure 5.76 shows the predicted magnesium oxide thicknesses of those mentioned aluminum alloys in both directions.

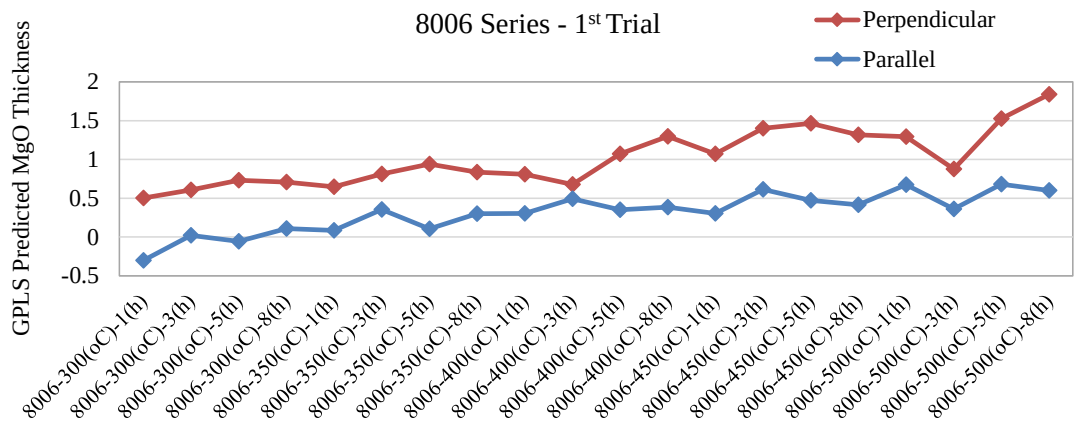
8006 Series - 1st Trial
Perpendicular
Parallel
GPLS Predicted MgO Thickness
2
1.5
1
0.5
0
-0.5
8006-300(oC)-1(h)
8006-300(oC)-3(h)
8006-300(oC)-5(h)
8006-300(oC)-8(h)
8006-350(oC)-1(h)
8006-350(oC)-3(h)
8006-350(oC)-5(h)
8006-350(oC)-8(h)
8006-400(oC)-1(h)
8006-400(oC)-3(h)
8006-400(oC)-5(h)
8006-400(oC)-8(h)
8006-450(oC)-1(h)
8006-450(oC)-3(h)
8006-450(oC)-5(h)
8006-450(oC)-8(h)
8006-500(oC)-1(h)
8006-500(oC)-3(h)
8006-500(oC)-5(h)
8006-500(oC)-8(h)

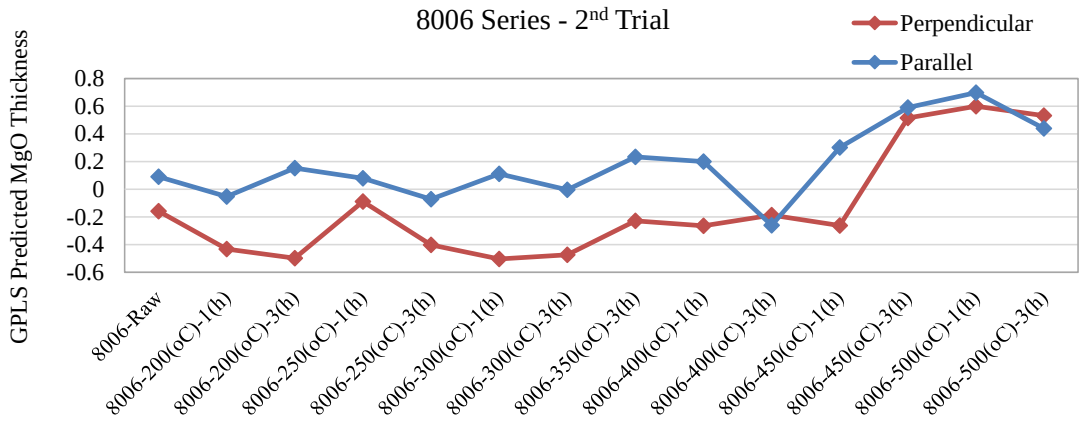
8006 Series - 2nd Trial
Perpendicular
Parallel
GPLS Predicted MgO Thickness
0.8
0.6
0.4
0.2
0
-0.2
-0.4
-0.6
8006-Raw
8006-200(oC)-1(h)
8006-200(oC)-3(h)
8006-250(oC)-1(h)
8006-250(oC)-3(h)
8006-300(oC)-1(h)
8006-300(oC)-3(h)
8006-350(oC)-3(h)
8006-400(oC)-1(h)
8006-400(oC)-3(h)
8006-450(oC)-1(h)
8006-450(oC)-3(h)
8006-500(oC)-1(h)
8006-500(oC)-3(h)

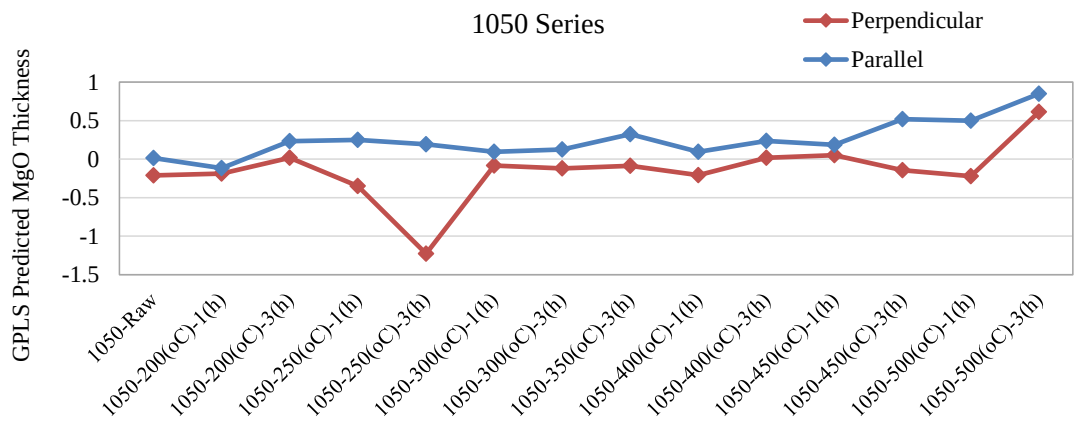
1050 Series
Perpendicular
Parallel
GPLS Predicted MgO Thickness
1
0.5
0
-0.5
-1
-1.5
1050-Raw
1050-200(oC)-1(h)
1050-200(oC)-3(h)
1050-250(oC)-1(h)
1050-250(oC)-3(h)
1050-300(oC)-1(h)
1050-300(oC)-3(h)
1050-350(oC)-3(h)
1050-400(oC)-1(h)
1050-400(oC)-3(h)
1050-450(oC)-1(h)
1050-450(oC)-3(h)
1050-500(oC)-1(h)
1050-500(oC)-3(h)

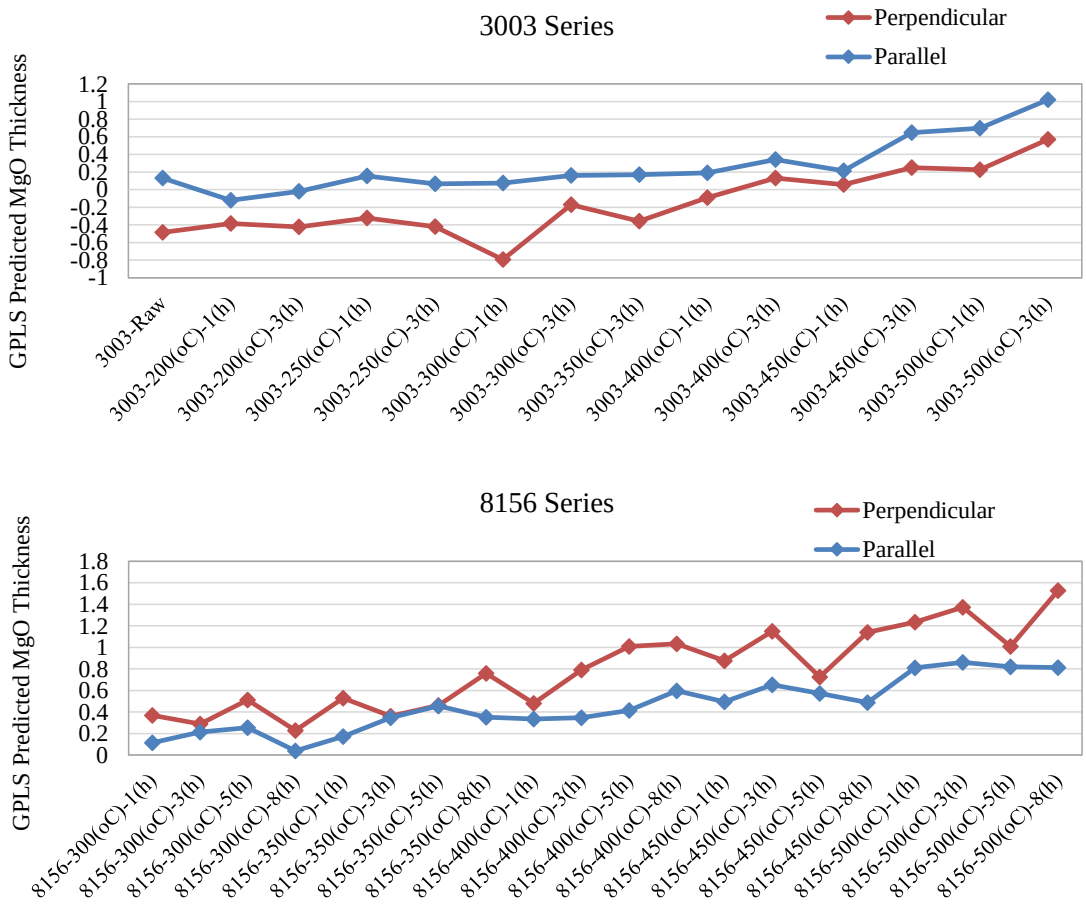

Figure 5.76. Comparison of predicted MgO thickness of five different series of alloys (8006-1st Trial, 8006-2nd Trial, 1050, 3003 and 8156) using perpendicular and parallel 3003BZ GPLS models.

When the predictions of the second trial of 8006, 1050 and 3003 series alloys are investigated, the negative values predicted from perpendicular measurements were observed which brings a strong suspicion for the reliability of these models. Also, for the first trial of 8006 and 8156 series alloys, the predictions obtained from perpendicular measurements resulted in values exceeding 1.0 nm which exceed the maximum magnesium oxide thicknesses observed in XPS reference study.

After the comparison of the predictions of all the compositionally similar alloy series carried out with the model obtained by 3003BZ series alloys, the parallel measurements are chosen to be a better measurement method since it provided more consistent, reliable and expected results in overall. Comparison of univariate and multivariate calibration methods constructed with parallel measurements are reported in the next section.

5.5.4. Comparison of Multivariate Calibration Models

After determining parallel measurements having more reliable predictions than perpendicular ones, all of the calibration models which are generated with SLS, GILS and GPLS were compared in order to choose the best calibration method. For both aluminum oxide and magnesium oxide thickness of 3105, 5005, 5052 and 5754 series alloys were compared with their corresponding 3005 series models while oxide thicknesses of 8006, 1050, 3003 and 8156 series alloys were compared with their corresponding 3003BZ series models.

5.5.4.1. Comparison of predicted Al_2O_3 thickness of 3005 like alloys SLS, GILS and GPLS models

First calibration method comparison was carried out with Al_2O_3 thickness predictions of 3105, 5005, 5052 and 5754 series alloys. Figure 5.77 shows the predicted Al_2O_3 thicknesses of those mentioned series by their corresponding 3005 series calibration models.

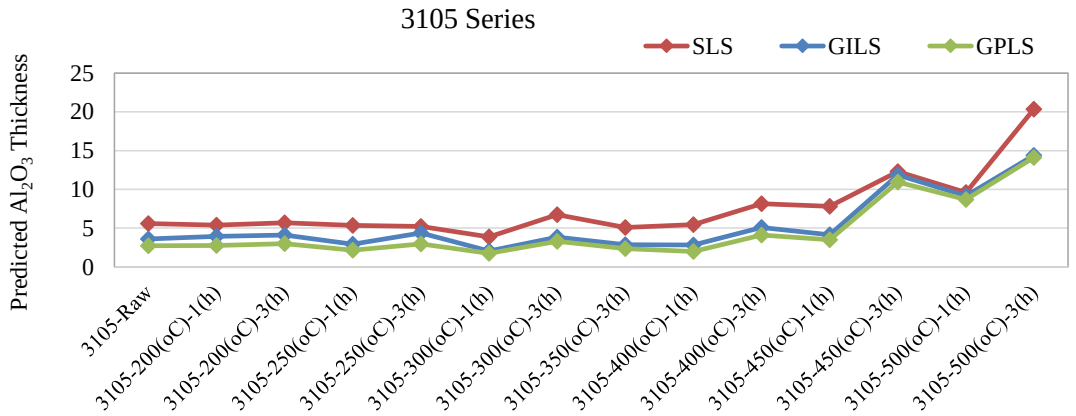

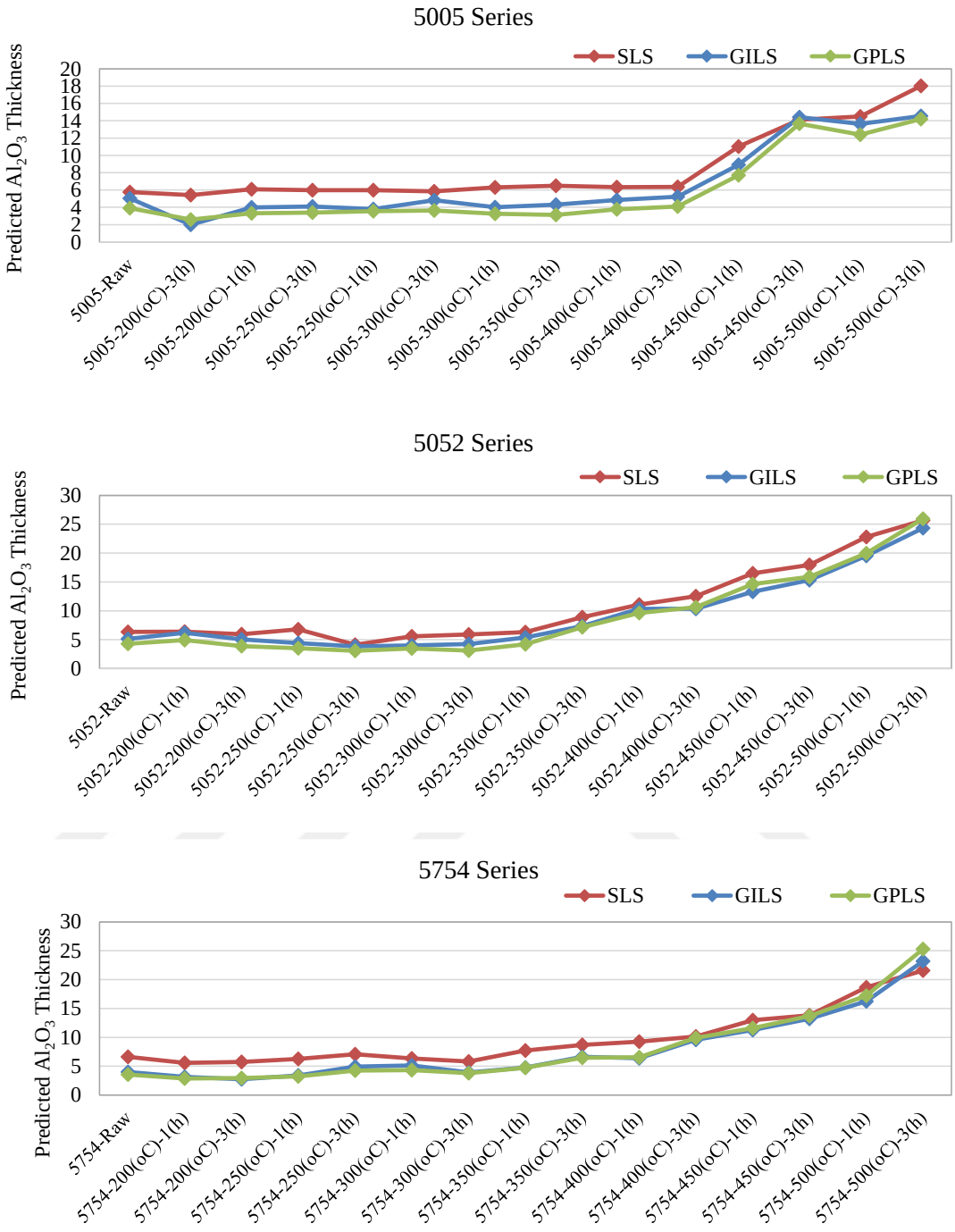

Figure 5.77. Comparison of predicted Al_2O_3 thickness of five different series of alloys (3105, 5005, 5052 and 5754) using 3005 series of GPLS, GILS and SLS models.

In Figure 5.77, for all the series of aluminum alloys, while the multivariate calibration methods which are GILS and GPLS models provide very consistent predictions with each other, SLS appears to have a positive bias when predicting

aluminum oxide thicknesses. However, the predictions of three methods for the 5052 series alloy appears to be quite similar.

5.5.4.2. Comparison of predicted MgO thickness of 3005 like alloys SLS, GILS and GPLS models

Comparison of four different aluminum alloys, which have already studied above, was also carried out with predictions of MgO thickness. Similarly, the predicted MgO thicknesses of 3105, 5005, 5052 and 5754 series alloys are shown in Figure 5.78 using SLS, GILS and GPLS.

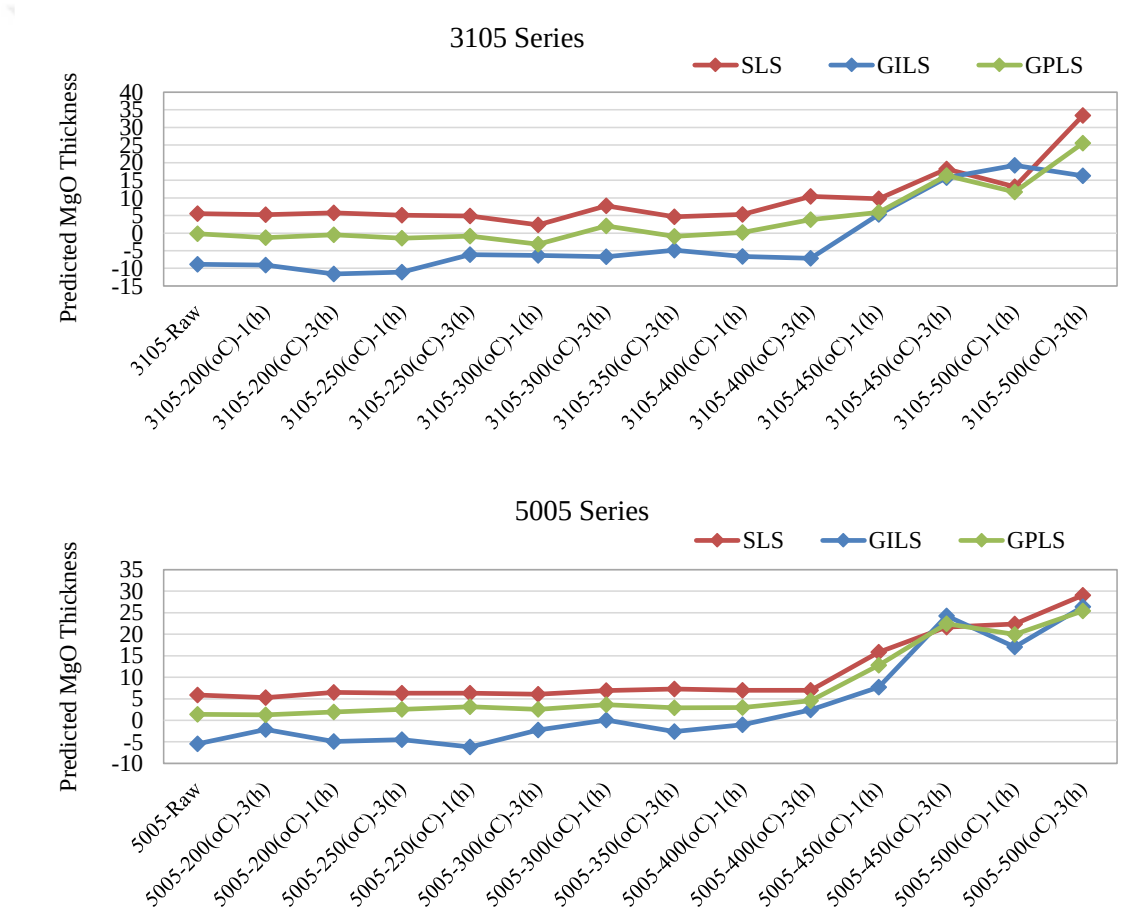

Figure 5.78. Comparison of predicted MgO thickness of five different series of alloys (3105, 5005, 5052 and 5754) using 3005 series of GPLS, GILS and SLS models.

Looking at the graphs shown in Figure 5.78, it is possible to say that the GPLS models provided the most reasonable MgO predictions whereas GILS often predicted negative thickness values and SLS led to the positive biased predictions. Another point is fluctuations are more evident in the predictions with GILS in overall.

From the both Al_2O_3 and MgO prediction graphs, it can be concluded that, GPLS models for 3005 series alloys have more successful predictions for aluminums which have additional magnesium content in them.

5.6.4.3. Comparison of predicted Al_2O_3 thickness of 3003BZlike alloys SLS, GILS and GPLS models

Same calibration method comparison was also performed with 3003BZ like alloys and the oxide thicknesses of 8006, 1050, 3003 and 8156 series alloys were predicted in order to compare which calibration method is the best. Figure 5.79 shows the predicted Al_2O_3 thicknesses of those mentioned aluminum alloys using 3003BZ series models in parallel direction.

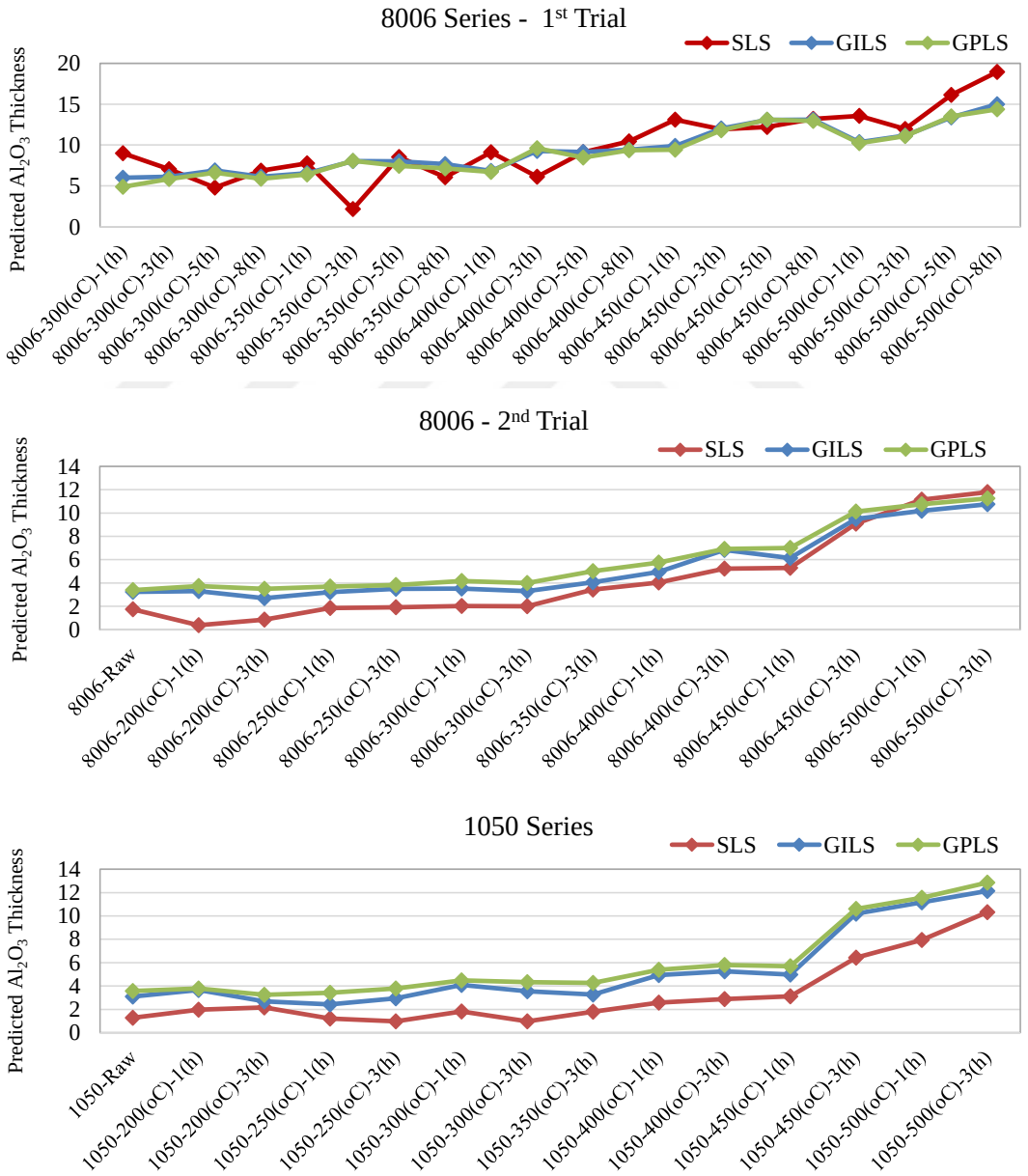

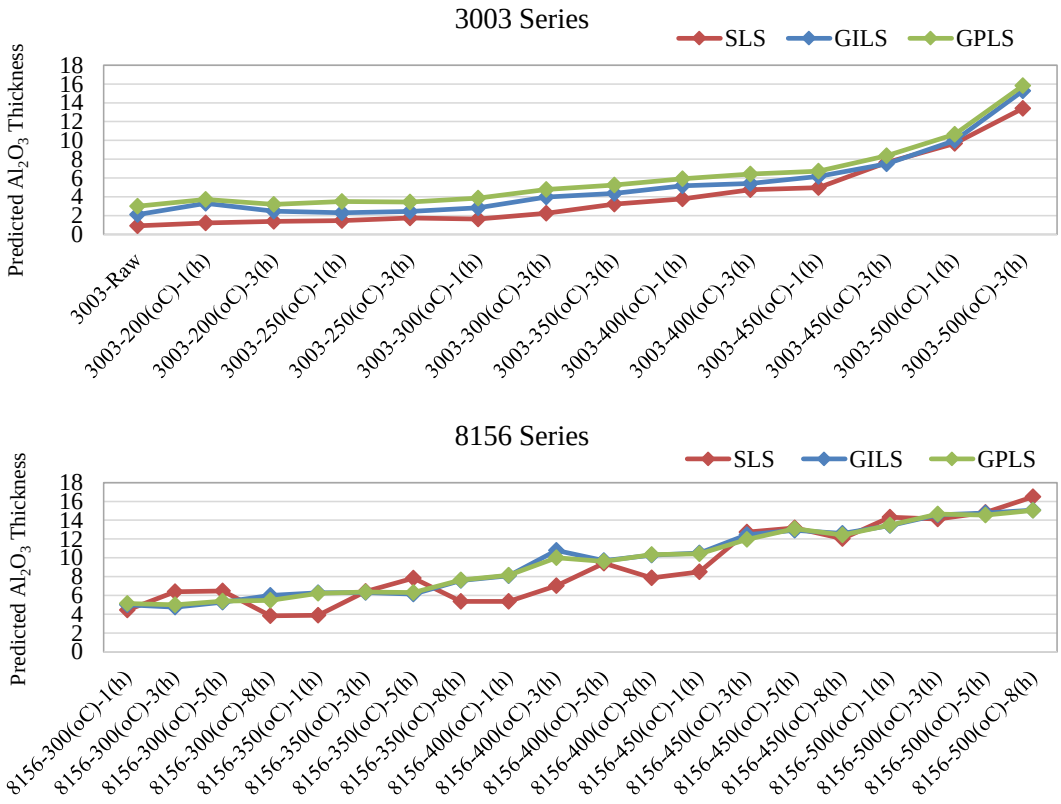

Figure 5.79. Comparison of predicted Al_2O_3 thickness of five different series of alloys (8006-1st Trial, 8006-2nd Trial, 3003, 1050 and 8156 series) using 3003BZ series of GPLS, GILS and SLS models.

By looking at the predictions of first trial of 8006 series alloys and 8156 series alloys shown in Figure 5.79, multivariate methods provided results which are strongly consistent especially as the annealing time and annealing temperature increases. However, the predictions of SLS method seems to be fluctuating resulting in an unreliable thickness values. Also, the second trial of 8006 series, 1050 series and 3003 series alloys, while the multivariate calibration methods provided similar results the predictions obtained by SLS models appears to be negatively biased.

5.5.4.4. Comparison of predicted MgO thickness of 3003BZ like alloys SLS, GILS and GPLS models

The last calibration method comparison was carried out with predicted MgO thicknesses of four different aluminum alloys which are namely 8006, 1050, 3003 and 8156 series alloys. Figure 5.80 shows the predicted MgO thickness of those mentioned aluminum alloys with their respective 3003BZ series models.

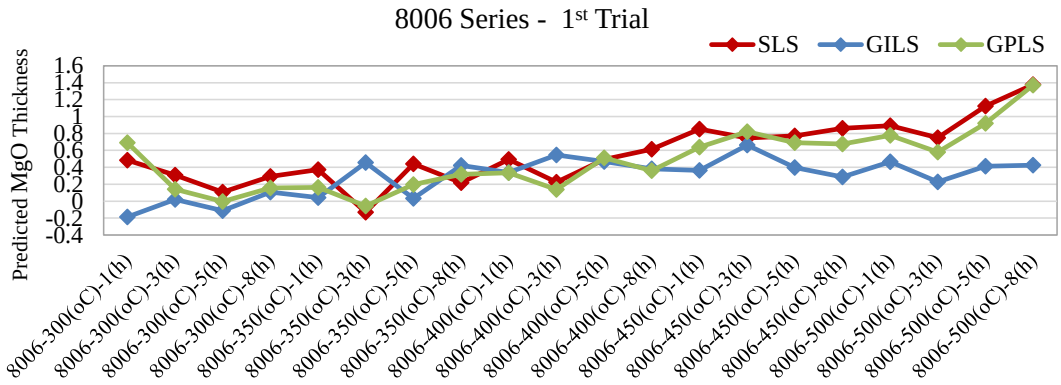
8006 Series - 1st Trial
SLS
GILS
GPLS
Predicted MgO Thickness
1.6
1.4
1.2
1
0.8
0.6
0.4
0.2
0
-0.2
-0.4
8006-300(oC)-1(h)
8006-300(oC)-3(h)
8006-300(oC)-5(h)
8006-300(oC)-8(h)
8006-350(oC)-1(h)
8006-350(oC)-3(h)
8006-350(oC)-5(h)
8006-350(oC)-8(h)
8006-400(oC)-1(h)
8006-400(oC)-3(h)
8006-400(oC)-5(h)
8006-400(oC)-8(h)
8006-450(oC)-1(h)
8006-450(oC)-3(h)
8006-450(oC)-5(h)
8006-450(oC)-8(h)
8006-500(oC)-1(h)
8006-500(oC)-3(h)
8006-500(oC)-5(h)
8006-500(oC)-8(h)

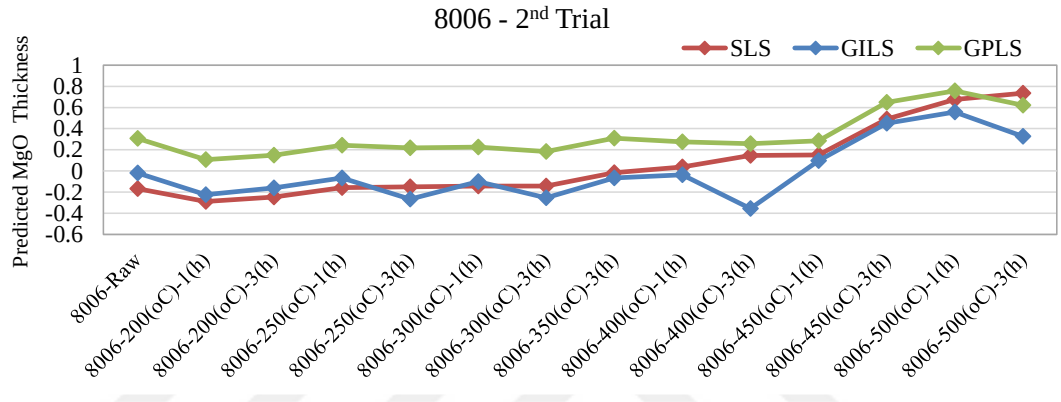
8006 - 2nd Trial
SLS
GILS
GPLS
Predicted MgO Thickness
1
0.8
0.6
0.4
0.2
0
-0.2
-0.4
-0.6
8006-Raw
8006-200(oC)-1(h)
8006-200(oC)-3(h)
8006-250(oC)-1(h)
8006-250(oC)-3(h)
8006-300(oC)-1(h)
8006-300(oC)-3(h)
8006-350(oC)-3(h)
8006-400(oC)-1(h)
8006-400(oC)-3(h)
8006-450(oC)-1(h)
8006-450(oC)-3(h)
8006-500(oC)-1(h)
8006-500(oC)-3(h)

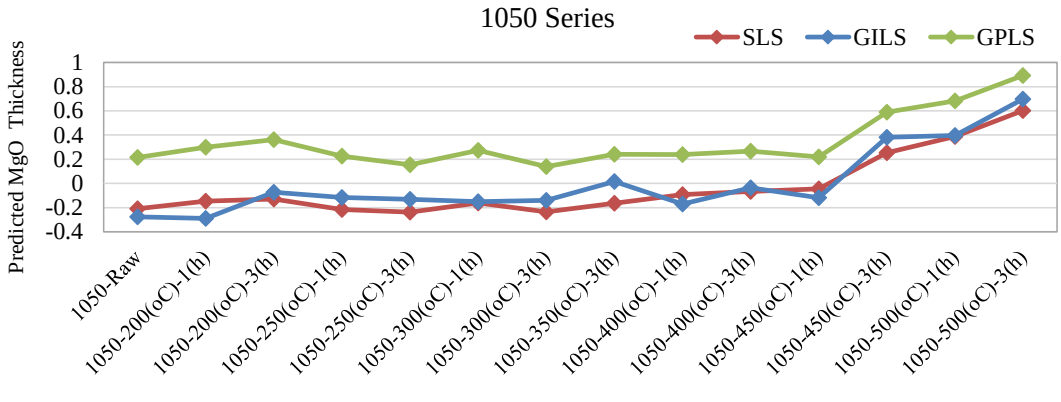
1050 Series
SLS
GILS
GPLS
Predicted MgO Thickness
1
0.8
0.6
0.4
0.2
0
-0.2
-0.4
1050-Raw
1050-200(oC)-1(h)
1050-200(oC)-3(h)
1050-250(oC)-1(h)
1050-250(oC)-3(h)
1050-300(oC)-1(h)
1050-300(oC)-3(h)
1050-350(oC)-3(h)
1050-400(oC)-1(h)
1050-400(oC)-3(h)
1050-450(oC)-1(h)
1050-450(oC)-3(h)
1050-500(oC)-1(h)
1050-500(oC)-3(h)

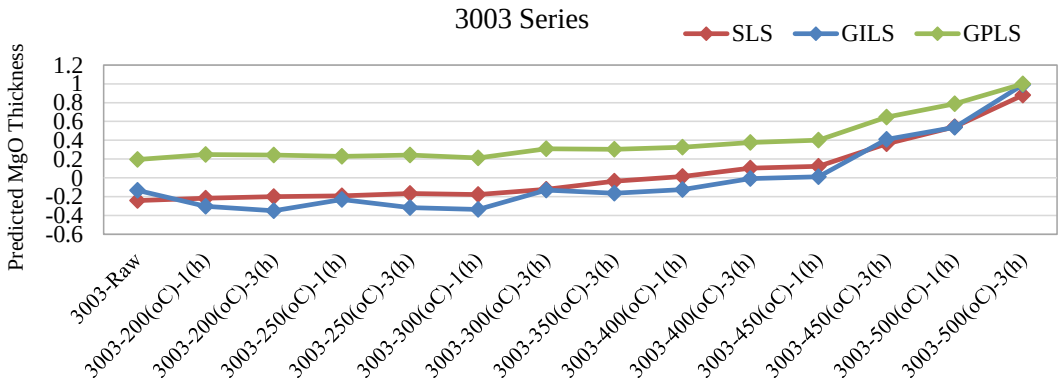
3003 Series
SLS
GILS
GPLS
Predicted MgO Thickness
1.2
1
0.8
0.6
0.4
0.2
0
-0.2
-0.4
-0.6
3003-Raw
3003-200(oC)-1(h)
3003-200(oC)-3(h)
3003-250(oC)-1(h)
3003-250(oC)-3(h)
3003-300(oC)-1(h)
3003-300(oC)-3(h)
3003-350(oC)-3(h)
3003-400(oC)-1(h)
3003-400(oC)-3(h)
3003-450(oC)-1(h)
3003-450(oC)-3(h)
3003-500(oC)-1(h)
3003-500(oC)-3(h)

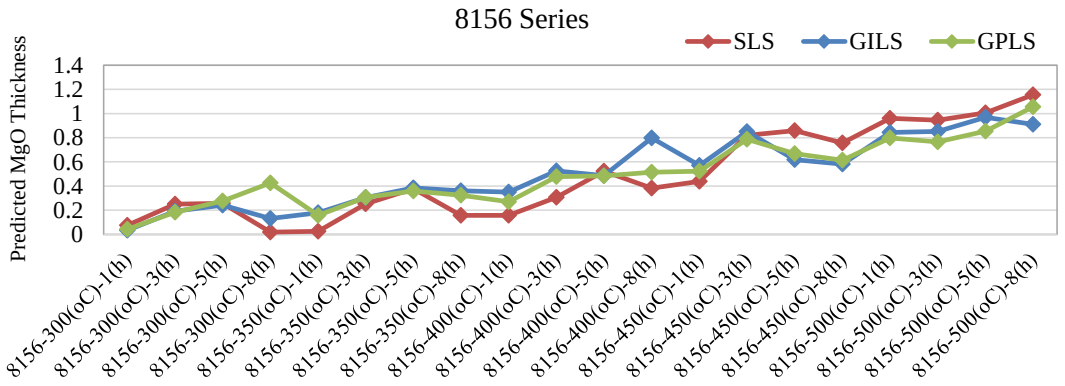

Figure 5.80. Comparison of predicted MgO thickness of five different series of alloys (8006-1st Trial, 8006-2nd Trial, 3003, 1050 and 8156 series) using 3003BZ series of GPLS, GILS and SLS models.

In the Figure 5.80, all of the calibration methods provides inconsistent predictions among each other for first trial of 8006 series and 8156 series. However, in the second trial 8006 series, 1050 series and 3003 series alloys, only GPLS predicted positive magnesium oxide thicknesses while SLS and GILS model predictions goes under zero.

Finally, similar to 3005 series modelling studies, GPLS method was chosen as the best calibration method for 3003BZ series to predict Al_2O_3 and MgO thicknesses on 3003BZ like aluminum alloys.

CHAPTER 6

CONCLUSION

In this study, a new method was developed for the measurement of nano-scale oxide thicknesses on aluminum foil and sheets surfaces using GATR-FTIR along with chemometric calibration techniques. Although univariate calibration techniques were also studied, because of the baseline shift due to formation of spinels, chemometrics multivariate calibration techniques, namely Genetic Inverse Least Square (GILS) and Genetic Partial Least Squares (GPLS), were applied to develop robust models.

From two different direction measurements which are perpendicular to the aluminum alloy rolling direction and parallel to the rolling direction, parallel direction measurements were chosen because their models demonstrated more predictive power. Even though both SLS, GILS and GPLS models provided adequate results on most of the alloys, GPLS performed better in all cases and had less over-fitting issues. Besides independent validation samples that were used, different alloy compositions in both cases proved the success of models. On the other hand, because of the additional magnesium in 3005 series which is resulted in the peak maxima shifts on the wavenumber scale formation of Al_2MgO_4 spinels was also another serious problem. In addition baseline shifts on the FTIR spectra due to surface morphology of the samples caused lack of success in prediction of Al_2O_3 thickness compared to 3003BZ models. It was also observed that the effect of annealing temperature is much greater when compared to the annealing time on the oxide formation.

Finally, a new method based on Grazing Angle ATR-FTIR combined with the chemometric multivariate calibration (GILS and GPLS) methods was developed and it provides a quantitative determination of oxide thickness resulting from annealing processes on the surfaces of aluminum sheets and foils. Unlike the XPS that is used for reference analyses, GATR-FTIR spectroscopy provides non-destructive, low-cost, simple and fast analysis. In addition, the application of this method carries the potential in the areas not only in aluminum industries but also in many other fields that deals with the surface related issues such as coating and painting.

REFERENCES

Brereton, Richard G. 2003. *Chemometrics: data analysis for the laboratory and chemical plant*: John Wiley & Sons.

Dunlop, HM, and M Benmalek. 1997. "Role and characterization of surfaces in the aluminium industry." *Le Journal de Physique IV* 7 (C6):C6-163-C6-174.

Franchy, René. 2000. "Growth of thin, crystalline oxide, nitride and oxynitride films on metal and metal alloy surfaces." *Surface Science Reports* 38 (6):195-294.

French, Roger H, Harald Müllejans, and David J Jones. 1998. "Optical Properties of Aluminum Oxide: Determined from Vacuum Ultraviolet and Electron Energy-Loss Spectroscopies." *Journal of the American Ceramic Society* 81 (10):2549-2557.

Garabagiu, Sorina, and Gheorghe Mihailescu. 2011. "Thinning anodic aluminum oxide films and investigating their optical properties." *Materials Letters* 65 (11):1648-1650. doi: 10.1016/j.matlet.2011.02.068.

Geladi, Paul, and Bruce R Kowalski. 1986. "Partial least-squares regression: a tutorial." *Analytica chimica acta* 185:1-17.

Habib, K. 2010. "Determination of oxide barrier-film thickness of anodized aluminum by electrochemical impedance spectroscopy at the nanometer scale." Southeast Asian International Advances in Micro/Nano-technology.

Hardy, An, C Adelmann, S Van Elshocht, Heidi Van den Rul, MK Van Bael, Stefan De Gendt, Marc D'Olieslaeger, Marc Heyns, JA Kittl, and Jules Mullens. 2009. "Study of interfacial reactions and phase stabilization of mixed Sc, Dy, Hf high-k oxides by attenuated total reflectance infrared spectroscopy." *Applied surface science* 255 (17):7812-7817.

Heilmann, A, F Altmann, D Katzer, F Müller, Th Sawitowski, and G Schmid. 1999. "Determination of the pore size and the vertical structure of nanoporous aluminum oxide membranes." *Applied surface science* 144:682-685.

Holler, F James, Douglas A Skoog, and Stanley R Crouch. 2007. "Principles of instrumental analysis." *Belmont: Thomson*.

Jeurgens, L. P. H., M. S. Vinodh, and E. J. Mittemeijer. 2006a. "Quantitative analysis of multi-element oxide thin films by angle-resolved XPS: Application to ultra-thin oxide films on MgAl substrates." *Applied Surface Science* 253 (2):627-638. doi: 10.1016/j.apsusc.2005.12.147.

Jeurgens, LPH, WG Sloof, FD Tichelaar, CG Borsboom, and EJ Mittemeijer. 1999. "Determination of thickness and composition of aluminium-oxide overlayers on aluminium substrates." *Applied surface science* 144:11-15.

Jeurgens, LPH, MS Vinodh, and EJ Mittemeijer. 2006b. "Quantitative analysis of multi-element oxide thin films by angle-resolved XPS: Application to ultra-thin oxide films on MgAl substrates." *Applied Surface Science* 253 (2):627-638.

Kempfert, KD, GJ Kemeny, SH Vogel, and M Modreanu. "Optimization of Grazing Angle Attenuated Total Reflection for the Analysis of Monomolecular Layers on Silicon."

Kim, Hui Sun, Jeffrey D Hartgerink, and M Reza Ghadiri. 1998. "Oriented self-assembly of cyclic peptide nanotubes in lipid membranes." *Journal of the American Chemical Society* 120 (18):4417-4424.

King, David E, and WE Swartz. 1987. "Variable-angle X-ray photoelectron spectroscopic determination of the thickness of the oxide layer on aluminum metal: An advanced undergraduate laboratory experiment." *Journal of Chemical Education* 64 (11):981.

Le Pévédic, Séverine, Didier Schmaus, and Camille Cohen. 2008. "Formation of a well-ordered ultrathin aluminum oxide film on Ni (111): Determination of its thickness, composition and structure." *Surface Science* 602 (1):67-76.

Lefez, B., J. Lopitaux, B. Hannoyer, M. P. Bacos, and E. Beucher. 2007. "Fourier transform infrared reflection absorption spectroscopy and microspectroscopy, a tool to investigate thermally grown oxide scales." *Thin Solid Films* 516 (2-4):349-354. doi: 10.1016/j.tsf.2007.06.126.

Mirabella, Francis M. 1998. *Modern techniques in applied molecular spectroscopy*. Vol. 14: John Wiley & Sons.

Movla, Hossein, and Mohammad Babazadeh. 2014. "Simulation analysis of the aluminum thin film thickness measurement by using low energy electron beam." *Optik - International Journal for Light and Electron Optics* 125 (1):71-74. doi: 10.1016/j.ijleo.2013.06.033.

ÖZDEMİR, DURMUŞ, and Betül Öztürk. 2004. "Genetic multivariate calibration methods for near infrared (NIR) spectroscopic determination of complex mixtures." *Turkish Journal of Chemistry* 28 (4):497-514.

Prescott, R, and MJ Graham. 1992. "The formation of aluminum oxide scales on high-temperature alloys." *Oxidation of metals* 38 (3-4):233-254.

Primera-Pedrozo, Oliva M, Yadira M Soto-Feliciano, Leonardo C Pacheco-Londoño, and Samuel P Hernández-Rivera. 2009. "Detection of high explosives using reflection absorption infrared spectroscopy with fiber coupled grazing angle probe/FTIR." *Sensing and Imaging: An International Journal* 10 (1-2):1-13.

Raacke, J, M Giza, and G Grundmeier. 2005. "Combination of FTIR reflection absorption spectroscopy and work function measurement for in-situ studies of plasma modification of polymer and metal surfaces." *Surface and Coatings Technology* 200 (1):280-283.

Roach, Paul, David Farrar, and Carole C Perry. 2005. "Interpretation of protein adsorption: surface-induced conformational changes." *Journal of the American Chemical Society* 127 (22):8168-8173.

Sezen, Hikmet, and Sefik Suzer. 2013. "XPS for chemical-and charge-sensitive analyses." *Thin Solid Films* 534:1-11.

Snijders, PC, LPH Jeurgens, and WG Sloof. 2002. "Structure of thin aluminium-oxide films determined from valence band spectra measured using XPS." *Surface science* 496 (1):97-109.

Ulman, Abraham. 2013. *An Introduction to Ultrathin Organic Films: From Langmuir--Blodgett to Self--Assembly*: Academic press.

Van Den Brand, J, WG Sloof, H Terryn, and JHW De Wit. 2004. "Correlation between hydroxyl fraction and O/Al atomic ratio as determined from XPS spectra of aluminium oxide layers." *Surface and interface analysis* 36 (1):81-88.

Xiang, Yuren, Chunlan Zhou, Endong Jia, and Wenjing Wang. 2015. "Oxidation precursor dependence of atomic layer deposited Al2O3 films in a-Si: H (i)/Al2O3 surface passivation stacks." *Nanoscale research letters* 10 (1):1-8.